NOTE TO USERS

This reproduction is the best copy available.

UMI®

Self Tuned NFC and Adaptive Hysteresis Based DTC Scheme for IM Drive

By

Lakehead University, Thunder Bay, Ontario

A thesis submitted in partial fulfilment of the requirement for the of Masters of Science

At

Lakehead University, Thunder Bay, Ontario

December, 2010

Canada

Abstract

The concept of field oriented control scheme brought the revolutionary change in industrial drives. Due to the high initial and running costs of the DC machines, the trend shifted from DC to AC motor drives to obtain high performance variable speed drives. The major achievement with field oriented control was the decoupled and independent control of stator and rotor quantities like DC machines. It is agreed that the control scheme for ac machines is complicated as compared to DC machines. The inherited problem with the ac machine control is the nonlinear relation between process variables e.g. speed and manipulated variables e.g. current, torque etc. Moreover, magnetic saturation of its rotor core causes developed torque relation of nonlinear nature.

Direct torque control (DTC) scheme is a vector control technique like field oriented control (FOC) scheme but it is faster and simpler. The DTC does not need any coordinate transformation like FOC. The DTC controls motor torque directly, so it is faster. The DTC scheme is used to obtain the high dynamic performance for control of AC machines like FOC. Conventional DTC scheme consists of two hysteresis comparators, a flux and torque estimator and a table used to select optimal inverter voltage vector. Both torque and flux are controlled simultaneously by the selection of appropriate voltage form the inverter. Due to the discrete nature of the control system and limited number of possible voltage vectors from the three phase inverter, this scheme suffers from high torque ripples. The bandwidth of hysteresis and variable slope of the torque make the switching frequency of inverter variable.

This thesis presents a critical analysis of the working components of DTC scheme. The torque production in induction motor (IM) and the factors which influence the ripple level in the developed torque are also analysed. On the basis of this analysis, it presents a new algorithm for the three level torque and two level flux hysteresis controllers. Then another algorithm is designed to vary the bandwidth of the torque hysteresis controllers online to keep the torque ripples within specified limits. This thesis further presents a simpler algorithm to determine the sector number of the stator flux linkage vector. Finally, a Neuro-Fuzzy Logic Controller (NFC) is proposed to improve the dynamic behaviour of the IM drive. The use of intelligent controller is very limited in the drive industry due to the relevant computational burden of the micro processor. Therefore, in order to reduce the computational burden, linear linguistic variables with lesser number of membership functions have been selected in this thesis. The effectiveness of the proposed NFC and adaptive hysteresis based DTC scheme of the IM drive is consolidated through the development of a simulation model using Matlab/Simulink. Then the complete IM drive, incorporating the proposed NFC based DTC scheme, is successfully implemented in real-time using digital signal processor (DSP) board-DS1104 for a laboratory 1/3 hp motor. The effectiveness of the proposed IM drive is verified both in simulation and experiment at different dynamic operating conditions. The results show the robustness of the drive and its potentiality to apply for real-time industrial drive applications.

Acknowledgements

Contents

1. Introduction

2. Modeling of Induction Motor for DTC

3. Fundamentals of Hysteresis Band Adapted DTC Scheme

4. Development of Neuro-Fuzzy Controller for DTC based IM Drive

5. Real-time Implementation

6. Conclusion and Future Scope

List of Symbols

a	120^0 phase shift operator
Kp	Proportional gain
Ki	Integral gain
e_T	Torque error
$\vec{i_r}$	rotor current phasor in the rotor frame
$\vec{i'_r}$	rotor current phasor in the stator frame
$\vec{v_r}$	rotor voltage phasor in the rotor frame
$\vec{v'_r}$	rotor voltage phasor in the stator frame
$\vec{i_s}$	stator current phasor in the stator frame
Ψ	magnetic flux linkage
$\psi_{s\alpha}, \psi_{s\beta}$	real and imaginary component of stator flux linkage
ψ_{sd}, ψ_{sq}	Real and imaginary component of rotor flux linkage
ψ_{sr}	Radial component of stator flux linkage
ψ_{st}	Tangential component of stator flux linkage
ψ_{so}	Residual flux linkage
$\psi_{sa}, \psi_{sb}, \psi_{sc}$	Flux linkage of phase a,b & c
ψ_s, ψ_r	Net stator and rotor flux linkage
v_a, v_b, v_c	a, b and c phase voltages
i_a, i_b, i_c	a, b and c phase currents

$v_{s\alpha}$, $v_{s\beta}$	Real and imaginary components of stator voltage
$i_{s\alpha}$	Real component of stator current
$i_{s\beta}$	Imaginary component of stator current
R_s	stator resistance per phase
R_r	Rotor resistance per phase
L_d	d-axis inductance
L_q	q-axis inductance
L_{sl}	Stator leakage inductance
L_{sm}	Stator magnetizing inductance
L_s	Stator self inductance
ω_s	Stator angular frequency or synchronous speed
ω_m	Mechanical speed of motor
$\omega_m{}^*$	motor command speed
$\Delta\omega$	Error between actual and command speed
e	Per unit speed error
Θ_m	mechanical rotor position w.r.t. stationary stator frame of reference
Θ	Position of stator flux vector w.r.t. stationary stator frame of reference
Θ_{sr}	Angle between stator and rotor flux linkages
p	differential operator d/dt
P	number of pole pairs
T_e, T_c	Estimated and command torques
T_L	load torque

J	rotor inertia constant
B_m	friction damping coefficient
V_{dc}	DC bus voltage for the inverter
$HB_{\psi U}$	Flux linkage hysteresis band upper limit
$HB_{\psi L}$	Flux linkage hysteresis band lower limit
HB_{TU}, HB_{TL}	Torque hysteresis upper and lower limits
HT_e	Output of torque hysteresis comparator
$H\Psi_s$	Output of flux linkage hysteresis comparator

List of Acronyms

AB	Adaptive Backstepping
AC	Alternating current
A/D	Analog to digital
AI	Artificial Intelligence
AIC	Artificial intelligent controller
ANFIS	Adaptive-network-based fuzzy inference system
BJT	Bipolar junction transistor
COA	Centre of Area
COG	Centre of Gravity
D/A	Digital to analog
DC	Direct Current
DSP	Digital signal processing
DTC	Direct torque control
ANN	Artificial neural network
FB	Feed backward
FOC	Field Oriented Control
FF	Feed forward
FLC	Fuzzy logic controller

GA	Genetic Algorihtm
GFLC	Genetic based fuzzy logic controller
HPD	High Performance Drive
HPVSD	High performance variable speed drive
IGBT	Inverted gate bipolar transistor
IM	Induction Motor
IPMSM	Interior Permanent Magnet Synchronous Motor
KCL	Kirchoff's Current Law
LCR	Linguistic control rule
LPF	Low pass filter
MIMO	Multi-input-multi-output
MRAC	Model Reference Adaptive Controller
MV	Manipulated Variable
NFC	Neuro-fuzzy controller
NNC	Neural network controller
PI	Proportional Integral
PID	Proportional Integral Derivative
PM	Permanent Magnet
PMSM	Permanent Magnet Synchronous Motor
PWM	Pulse Width Modulation
RFI	Radio frequency interference
RTI	Real-time Interface

SISO	Single-input-single-output
SMC	Sliding Mode Control
SP	Set Point
TI	Texas Instruments
TSK	Takagi-Sugeno-Kang
v/f	Voltage/frequency
VSD	Variable Speed Drive
VSI	Voltage Source Inverter

CHAPTER 1

Introduction

This chapter concisely introduces major types of electrical motors. It details the unique and special properties of squirrel cage induction motor (IM) which makes it so attractive for industrial use. Later, it discusses different control techniques and controllers for variable speed drives (VSD). Finally, it briefly elaborates the motivation behind this thesis work.

1.1 Electric Motors and Controls

Electrical motors are the major source of electromechanical energy conversion. The first electrical motor was invented by Michael Faraday in 1821. Then it followed by Tesla who developed the first AC synchronous motor in 1883. The most important fact about the motors is that they are consuming almost 50% of the generated electrical energy [1]. Especially, the major industrial horse, the Induction Motor, which is almost 70% of the total motors load. This reality draws researcher's attention to improve IM performance.

Over the global environment concern, the 15th conference of the *United Nations Framework Convention on Climate Change* was held in Copenhagen from Dec, 7-17, 2009. According to *Copenhagen Accord*, Canada should cut down carbon emission by 20% below 2006 level by 2020 [2]. Since one of the major electrical energy consumers is an IM so improvement in its efficiency will bring a significant reduction in pollution level. Keeping in

view this important factor a consortium, *Motor Challenge Program*, was organized in Europe in 2003 which aids the industrial companies working for the improvement of efficiency of their motor driven systems.

Before the revolution of Power Electronics, the major source of speed control was the motor winding connections [3]. This method provides a very specific numbers of speed values based on the number of poles of the motor. The use of power electronics made it possible to control the speed more precisely from very low to over the rated speed of the motor. Principally, the idea is to change the motor supply voltage frequency instead of poles to achieve the desired speed.

After the revolution of power electronics and with the possibility to implement complex algorithms with microprocessor, the researcher shifted their attention to control the AC machines like DC machines. Principally, there are two modern vector control techniques for AC machines i.e. field oriented control (FOC) scheme and direct torque control (DTC) scheme. The latter is comparatively simpler. The main features of DTC scheme are:

- Direct control of motor torque and flux.
- Indirect control of stator voltage and current.
- Ideally, sinusoidal stator flux and current waves.
- High dynamic performance over the entire speed range.

The DTC is sophisticated, simpler and faster control scheme as compared to FOC. It does not need any synchronously rotating coordinate transformation like FOC and directly

2

control the motor torque. Therefore, in this thesis attempt has been made to improve its efficiency and dynamic characteristics.

1.2 Induction Motors

Induction Motor is the most popular electromechanical energy conversion device for the industry due to its simple and robust construction. Depending on the demand, IMs are manufactured form fraction to thousand of horse power. Based on the construction of rotor, IMs are classified as wound and squirrel cage type. Almost 90% of industrial IMs are of squirrel cage rotor type. The special advantages of squirrel cage type are rugged structure, no electrical connection to rotating part, efficient, high overload capability, low cost, compact, least maintenance requirement and due to inaccessible rotor can work even in volatile environment.

Rotor winding conductor   Body

Shaft
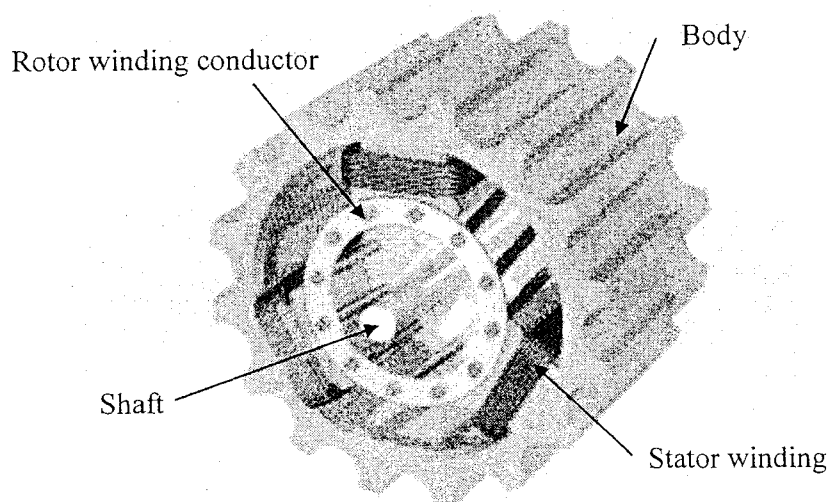
Stator winding

Fig. 1.1: Cross-sectional view of an induction motor.

3

The wound type IM has only edge that the rotor winding is accessible. This feature might be used to improve the starting torque. In the proposed drive scheme, the rotor accessibility is not required so the squirrel cage IM is used in this work. A cross-sectional view of the IM is shown in Fog.1.1, clearly showing the rotor and stator windings.
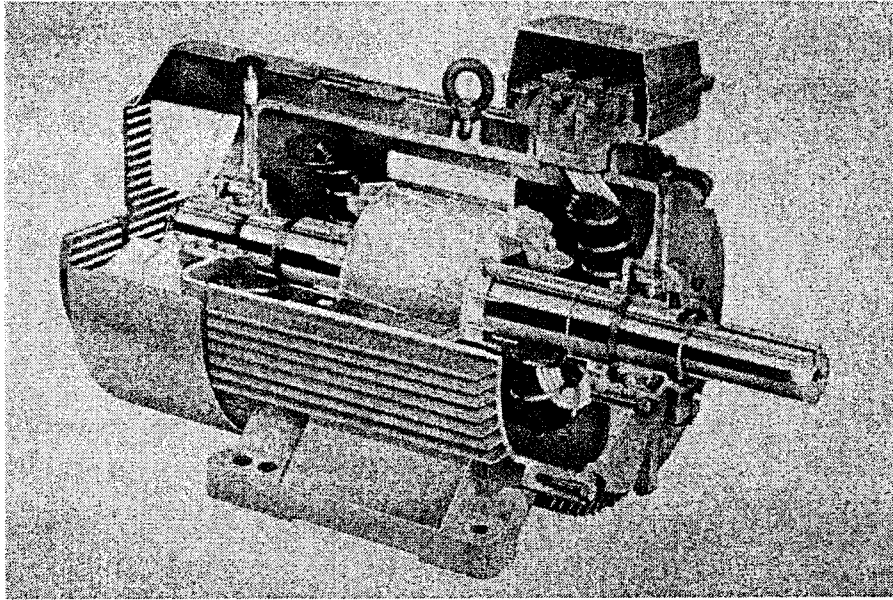
Fig. 1.2: Longitudinal view of a squirrel cage induction motor

In order to have a detailed view of stator, rotor and other mechanical parts, the longitudinal view of a squirrel cage IM is shown in Fig.1.2. As compared to the DC machines, the speed/position control of an IM is difficult due to its nonlinear characteristics. The introduction of vector control techniques has made it possible to independently control the stator and rotor fields of an induction motor like DC motors.

4

1.3 Literature Review

All the advancements in motor drive are thankful to the revolution of power electronics and microprocessor based digital signal processing (DSP) techniques. After 1970s these devices has made it economically possible to apply new algorithms for the motor control schemes. The only requirement to produce high performance drive (HPD) is the availability of a voltage source with variable amplitude and frequency. The change in frequency is to get a proportional change in speed and variable amplitude to meet the rated load of the motor. Before the advancement of power electronics, the only option to change the motor field was to vary its number of poles. That method was very costly with very small flexibility. After the availability of required tools for HPD now the only left over job is to find some suitable scheme for the motor control. The target is to get the simpler and practicable scheme which could produce desired results.

1.3.1 Control Schemes

The ideal goal of a control scheme is that the machine follows the command trajectory and it operates within its rated parameters with maximum efficiency. Motor control/drive means to control the motor speed or torque. When the variable speed drive (VSD) operates in 'Torque Control' mode, its speed is left uncontrolled and is determined by the load. Similarly, in 'Speed Control' mode, torque is determined by the load. Principally, there are two major control strategies. The first and primitive is scalar or non-vector control used for low performance drives. This scheme uses the stator voltage or current as control parameter for speed or torque control, respectively. The basic idea is to keep the stator field constant by varying the magnitude of voltage/current and frequency [4]. The main advantage of this scheme is its simplicity and it

5

can be used for both feed forward and feedback loops. The major drawbacks are its low accuracy and it response is satisfactory in steady state and poor response under transient conditions [5, 6]. Due to its simplicity, this scheme is still in use by the industry.

Contrarily, in vector control scheme both the magnitude and phase angle of the alternating current (manipulated variable) are controlled. It means the position vector of the manipulated variable is known after each sampling time for discrete control scheme. This characteristic, contrary to scalar control system, enable the controller to control both transient and steady conditions of the system [7, 8]. In vector control of AC machines, the torque and flux producing components of stator current are decoupled (being orthogonal to each other) and are controlled independently like a separately excited machine [9]. Vector control technique may be further sub-divided into field oriented and direct torque control schemes. These schemes do the same job but in a different way. They control the motor torque and flux in order to track the command trajectory irrespective to the system conditions and disturbances. Both schemes have successfully been implemented by the industry for HPD. The major drawback of the vector control scheme is the computational burden for transformation of the vectors to a specific reference frame and also they are motor parameter dependent [10].

For vector control of AC motors, the concept of field oriented control was introduced by Blasckke in 1970's [11]. The stator current is transformed into its real (flux producing) and imaginary (torque producing) components. Orthogonal nature of these components makes it feasible to control them independently [12, 13]. This scheme due to its accuracy of control is used for HPD. The drawback compared to scalar control is that this scheme for its implementation needs a lot of computations for conversion of parameters to a reference frame. This drawback is not of significant importance after the common use of microprocessor. After its

6

sensorless application by Toyo Electric Mfg. Co. Ltd Japan, this technique is becoming more popular in industry [14].

The direct torque control was introduced by Takahashi and Depenbrock in 1980s [15, 16]. The idea to control an IM by direct torque control scheme is similar to the FOC in the sense that both the motor field and torque are controlled independently. The difference is that in FOC the motor torque and stator flux linkage are controlled indirectly by the imaginary and real component of the stator current, respectively. While in DTC these quantities are controlled directly. Therefore, the DTC is faster than the FOC. There is no need of coordinate transformation and pulse width modulation (PWM) regulator as required in FOC. The DTC scheme is only sensitive to stator resistance which is a static component and undergoes comparatively smaller variations during operation as compared to rotor resistance. This aspect makes DTC scheme simpler for computations [17, 18]. The DTC scheme for the control of AC machines is becoming popular since its first industrial sensorless application introduced by ABB in 1995 [19]. According to ABB, the DTC is the ultimate and most advanced AC drive technology. The DTC scheme is almost 10 times faster than any AC or DC drive. The dynamic speed accuracy is 8 times better than any open loop AC drive and comparable to a DC drive that is using feedback [20]. The current industry is looking for a simple, reliable, faster, efficient, low noise producing and economical motor drive scheme. The only available VSD, matching most of the desired requirements is an IM with DTC scheme.

7

1.3.2 Controllers

The mathematical model of an IM is non-linear. The researchers have developed different controllers for this model. The proportional-integral-derivative (PID) controller was in use for governor design system since long. But the first analysis of the PID controller was made by Minorshy [21]. Due to its simplicity and acceptable results this most primitive controller is still used by the industry. The derivative part of the controller creates problems in real time implementation. It amplifies the noise and needs a low pass filter (LPF) for its working. Therefore, the most common form of this controller is proportional-integral (PI) controller which excludes derivative part. The working of PI controller is explained in Fig.1.3. The acronyms SP, PV & MV stands for the set/reference point, process/measured variable and manipulated variable respectively. Mathematically, the output of PI controller may be described by the following relation:

$$y = K_P \, e(t) + K_i \int_0^t e(\tau) \, d\tau \qquad (1.1)$$

Where 'e' is the difference between reference and measured values of the control variable. The effect of change in proportional gain 'K_P' on the output of the controller by keeping the integral gain K_i constant is shown in Fig.1.4.a. Similarly, Fig.1.4.b shows the results for variation in integral gain 'K_i' and keeping K_p as a constant. Conclusively, the PI-controller is characterized by high overshot and almost no steady state error. The overall performance of the conventional PI controller is compromising because it does not have any direct knowledge of the process. The fixed gain PI-controller is inherently sensitive to parameter variation and disturbance of the system and is difficult to use for HPD [22].

8
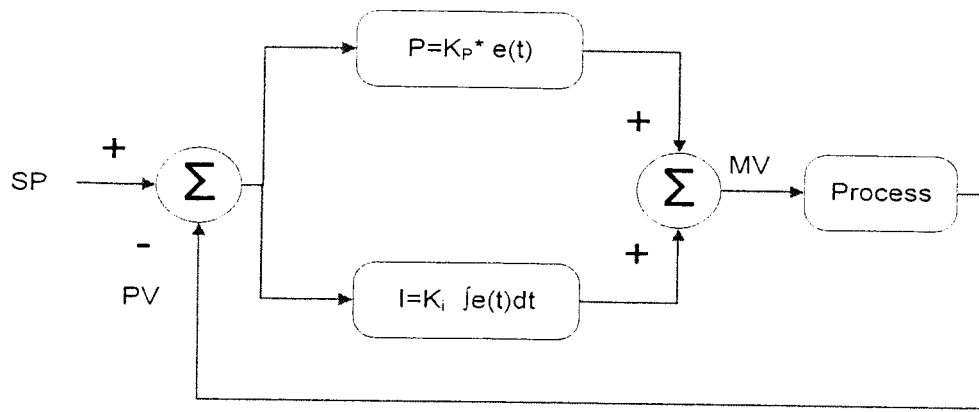
Fig. 1.3: Close-loop diagram of a PI-controller
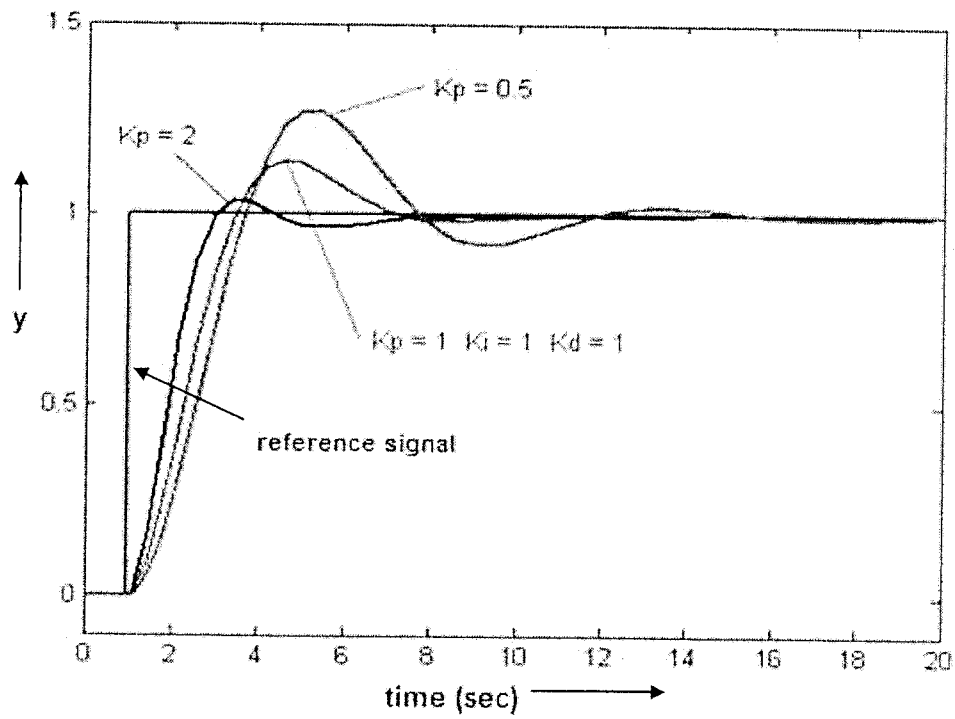
Fig. 1.4.a: Plots for output of PI-controller for various values of K_P and by keeping K_i constant.

9
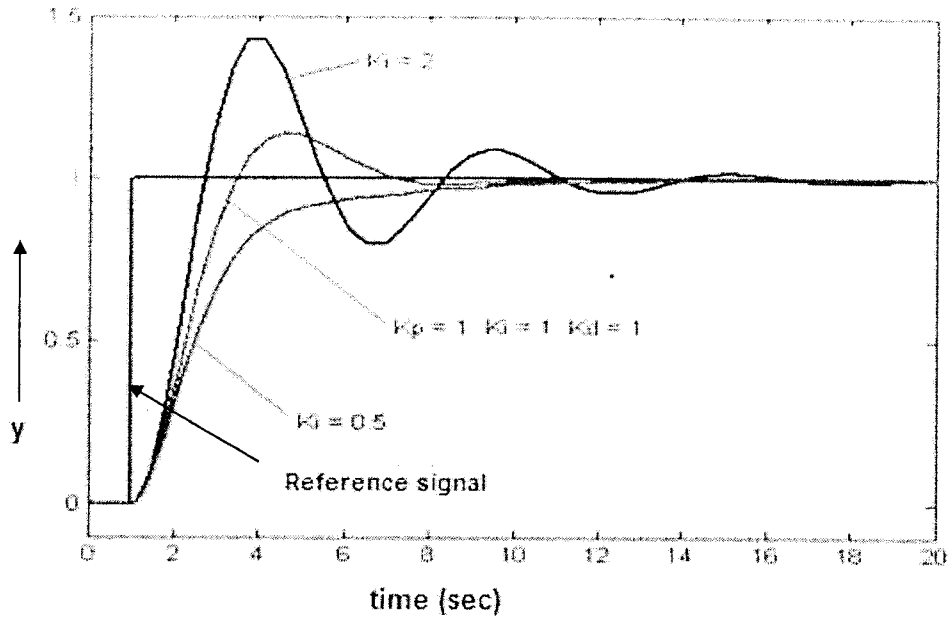
Fig. 1.4.b: Plots for output of PI-controller for various values of K_i and by keeping K_p constant.

The researchers proposed different technique to overcome the inherited problem with a PI-controller [23, 24]. They tuned the parameters of the PI-controller by both off-line [23] and on-line [24] methods. However, the new controller introduced complex tuning rules and requires very long sampling time up to 50ms, which is not acceptable for HPD.

The problem of sensitivity to system parameters change and disturbances was resolved by the introduction of adaptive controllers. The idea behind adaptive controller is that it updates the system parameters at each sampling time. Researchers have proposed mainly three types of the adaptive controllers [25-27]. These controllers modify the control laws to mitigate the parameter changes and system disturbances. This is achieved by changing the system gains in such a way to converge the tracking error between reference and actual machine models.

10

Sliding mode control (SMC) is comparatively simpler adaptive technique [28-29]. Due to discrete nature of control system and limitation of sampling time this technique causes the motor chattering around set point [30]. These vibrations cause stress on the load and can damage the motor bearings. The latest nonlinear control technique, called adaptive backstepping (AB) control technique, was introduced in 1990s [31]. This recursive technique is called backstepping because it starts with some virtually stable system and progressively steps back to the actual system, guaranteeing stability at each step [32]. Tan et. al. used this control technique with field oriented principle to control IM [33]. The major problem with this technique is the availability of finding an absolutely correct mathematical model of the IM.

The researchers [34-36] claimed that under ideal conditions it is possible to design globally stable adaptive systems. But later it was proved that the modelling errors e.g. bonded disturbances and/or unmodeled dynamics, the adaptive scheme designed for ideal conditions may go unstable [37]. The main reason for this instability was the adaptive law for estimation of parameters that made the closed loop system non-linear and more susceptible to the effects of modelling errors.

The precise dynamic control of a squirrel cage IM is complicated mainly due to the nonlinear relation between its winding currents (manipulated variable) and rotor speed (process variable). The nonlinearity in the motor developed torque due to magnetic saturation of the core adds further complexity for the controller [38]. The core advantage of the artificial intelligent (AI) controllers is that they don't need the exact mathematical model of the system and it can cope with system nonlinearities and disturbances [39]. The requirement for AI controllers for high performance variable speed drive (HPVSD) proper functioning is the approximate system mathematical model to handle system nonlinearities and disturbance [40-42].

11

The basic concept for the first type of artificial intelligent controller, called the fuzzy logic controller (FLC), was introduced by Zadeh [43]. Both fuzzy sets and fuzzy logic are based on the pattern the human brain deals with inaccurate information. The performance of fuzzy logic control and decision system depends on the input and output membership functions, the fuzzy logic rules and the fuzzy inference mechanism. Ideally, the FLC can handle any kind of the system nonlinearities [44]. Many researchers developed different FLCs based on their experience of drive behaviour, for the FOC/DTC based IM drive [45-52]. Most of the times, in DTC scheme, the researchers have used FLC to replace flux/torque hysteresis controllers. The FLC has been used to improve the torque response of the DTC based IM drive by replacing conventional torque hysteresis comparator [45-48]. The target is to make the hysteresis bandwidth variable parameter based on torque/speed variations. But the use of extensive membership functions and rules make the system cumbersome. Especially, the author of [46] has used 180 fuzzy rules which are almost impossible to implement in real-time. Most of the reported works on FLC based drive system is provided in the simulation only due to the high computational burden. Therefore, in this thesis, instead of a complicated FLC a simple linear hysteresis controller model is developed to achieve the optimum torque ripple and switching frequency of the voltage source inverter (VSI).

The artificial neural networks (ANN) has preference over the FLC that they are capable of learning the desired mapping between the inputs and outputs of the drive system stability and they do not require too much human knowledge about the system behaviour [53]. The ANNs are modelled after the physical architecture of the brain to solve a problem. The accuracy of performance of an ANN is based on the computational function of the neurons and the structure of the network [54]. The researchers have used ANN to produce the VSI input voltage vector

12

form the error signals [55, 56]. The author of [55] has used two neural networks. The first ANN finds the position of stator flux linkage vector. Though, the DTC scheme for its working just required the sector where flux linkage vector is lying and not its actual position. The second ANN is used to just replace the conventional DTC table without modifying its functionality. The author of [56] has also used the artificial intelligence to produce the lookup tables. Both of the citations don't have real time results.

To improve the speed response, another work on DTC scheme has been reported by the researcher [57]. The author in this work has used a hybrid controller, switching PI-controller for steady state and a FLC for transient state. The switching mechanism is based on the magnitude of the speed error. The switching transition of the controller always create real time problem. Further PI-controller is used in steady state which is highly sensitive to motor parameters and system disturbances. Even FLC has no learning mechanism and it is designed on trial and error.

1.4 Thesis Motivation

As the DTC scheme is simpler and faster than its competitive FOC scheme, it is selected as a control strategy for the squirrel cage IM in this work. The biggest problem in this scheme is the large ripples in the torque and stator flux both in transient and steady states. As discussed in the literature, various researchers have suggested different schemes based on the complicated neuro fuzzy techniques to reduce these ripples which are almost impossible to implement in real-time. Therefore, in this thesis a new simple and very low computational algorithm is designed to reduce the motor torque and stator flux ripples.

13

As per author information, no major work has been reported to improve the dynamic speed response of DTC scheme. Therefore, a simple neuro-fuzzy controller with two linguistic variables, each having two simple membership functions is proposed in this work to replace conventional PI-controller.

1.5   Thesis Organization

The remaining part of this thesis is organized in the following sequence. Chapter -2 is devoted to the modeling of a squirrel cage induction motor for the direct torque control scheme. It covers the production of torque and flux linkages in the motor.

Chapter-3 analyses the conventional DTC scheme. Motor torque and flux linkages are elaborated and the factors affecting the production of these quantities are discussed. Production of torque and flux ripples is further discussed and a new algorithm is presented for the optimization of these ripples and switching frequency of the inverter. Some simulation results, using Matlab/Simulink software is also presented for the performance investigation of the proposed adaptive hysteresis algorithm. Further, for the DTC scheme, instead of conventional, a simpler algorithm is developed to determine the stator flux linkage sector number.

Chapter 4 provides a detail discussion about the functioning of a NFC. Then a NFC has been proposed for dynamic characteristic improvement of the DTC scheme. The tuning of the NFC parameters in the control system is also discussed in this chapter. The new designed controller has been validated by some simulation results.

Chapter-5 shows the real time implementation of the proposed drive system. Real time set up and results of NFC based adaptive DTC scheme are presented taking into consideration all the

non-ideal behaviour of the drive system. Comparative experimental results of the proposed NFC based DTC scheme with the PI-controller based conventional DTC scheme is also presented in this chapter. Further this chapter discusses the contribution of this work, its future possible improvement/amendments. Finally a conclusion is drawn.

At the end all pertinent references and appendices are listed for convenience.

CHAPTER 2

Modelling of Induction Motor for DTC

The design of any kind of controller is based on the plant/machine dynamic model. The tolerance levels for different machine models are entirely different due to machine ratings and design. The machine model should be simple so that it could be implemented easily and at the same time it should be so accurate to provide the acceptable results. So, there exists a compromise between accuracy and economy. The transient and steady state behaviour of the machines are entirely of different nature. The model must be capable to work for both states. Generally, an IM is modelled by using space-phasor or two axes theory [58]. In this thesis the space-phasor theory is preferred since it provides more understanding of the physical picture of the system. For the squirrel cage induction motor the following assumptions are made to derive its mathematical model:

- Rotor core never saturate.

- Uniform air gap between stator and rotor windings.

- Machine iron losses and end effects are neglected

- Both stator and rotor windings are full pitch coils

- Slotting effects are neglected.

- Unity Winding Factor.

- Machine mmfs are pure sinusoidal centred on the magnetic axis of the respective winding.

16

- Zero Magnetic reluctance of stator and rotor cores.

- Flux density is radial in airgap between stator and rotor.

- Symmetrical two poles machine.

- Both rotor and stator has balanced three phase windings.

2.1 IM Space Phasor Model

2.1.1 Space Phasor Representation of Stator Flux Linkages

Space phasor model of the machine is used to simplify the machine analysis for real time implementation and to have better understanding of physical system [19]. The three phase stator current waveforms are shown in Fig.2.1. Corresponding to any instant of time 't' the three phase current phasors is drawn in Fig.2.2.
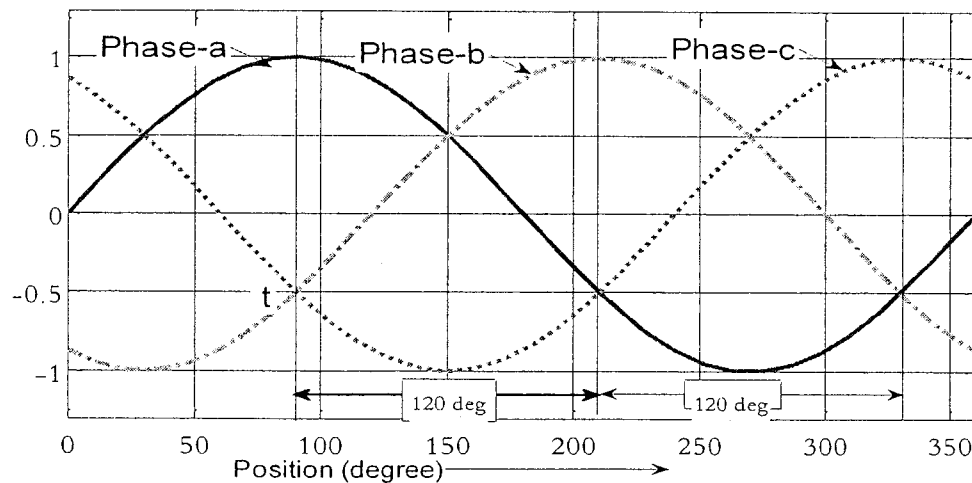
Fig. 2.1:   Three phase balanced current waveforms
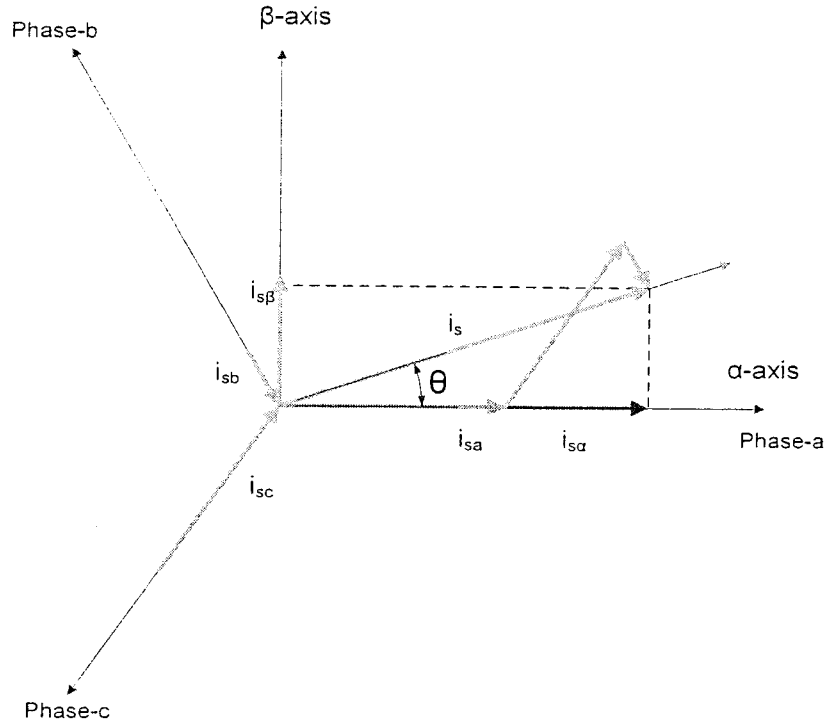
Fig. 2.2: Three phase current phasors

Where α and β-axes present the two phase stationary frame attached to the stator. The three phasors of IM flux linkages, produced by stator currents are converted to a complex plane located in the cross-section of the motor. The resultant flux linkage rotate with an angular speed equal to the three phase supply frequency. This single resultant space phasor can describe the rotating magnetic field like the regular three phases. This conversion of the system frame allows the analysis in terms of complex algebra which is easier to comprehend. Similar analysis can be made for the other motor parameters like voltages etc.

18

Fig.2.3 (a) & (b) shows the actual and equivalent net flux linkage diagrams of IM, respectively. Note that in both cases the net flux linkage rotates with the synchronous speed. For the balanced three phase system, the resultant stator space phasor flux linkage can be expressed as follows:

$$\vec{\psi}_s = 2/3[\vec{\psi}_{sa} + a\vec{\psi}_{sb} + a^2\vec{\psi}_{sc}]$$ (2.1.a)

or

$$\vec{\psi}_s = |\psi_s|e^{j\theta}$$ (2.1.b)
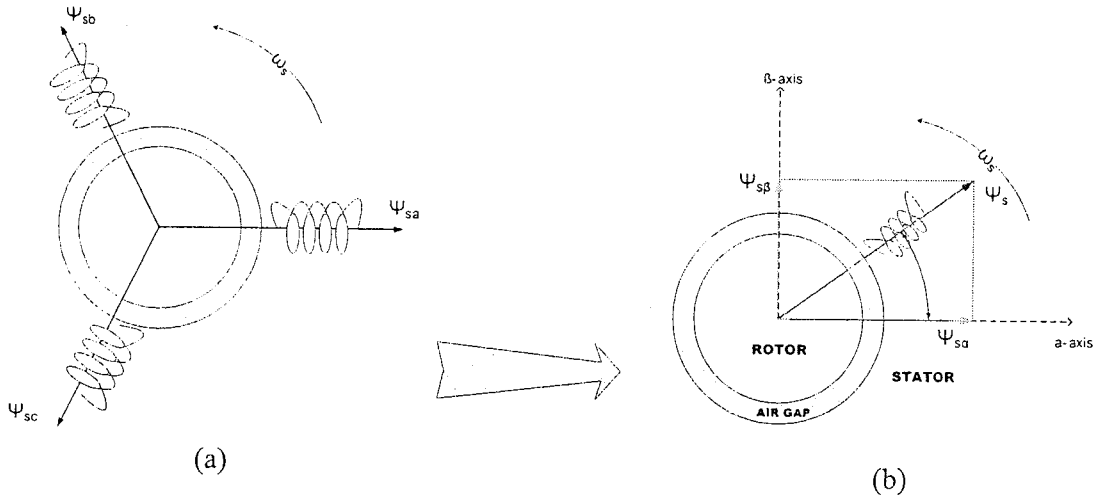

Fig. 2.3: (a) Three phases of stator flux linkages, (b) Equivalent phasor in two axes

The α, β-axes equivalent of the IM stator winding is shown in Fig.2.3 (b). From α, β- axes equivalent of flux linkage vectors, one can easily deduce the following mathematical relation:

$$\vec{\psi}_s = \vec{\psi}_{sa} + j\vec{\psi}_{s\beta}$$ (2.2)

Comparing (2.1.a) and (2.2) one can write as:

19

$$Re(\vec{\psi}_s) = Re\{2/3[\vec{\psi}_{sa} + a\vec{\psi}_{sb} + a^2\vec{\psi}_{sc}]\} = \vec{\psi}_{sa} \qquad (2.3)$$

$$Im(\vec{\psi}_s) = Im\{2/3[\vec{\psi}_{sa} + a\vec{\psi}_{sb} + a^2\vec{\psi}_{sc}]\} = \vec{\psi}_{s\beta} \qquad (2.4)$$

Based on the assumptions made in the opening paragraph of this chapter and considering only one stator and rotor winding for each phase, as single, multi-turn full pitch coils located on the two sides of the smooth air gap, the schematic diagram of IM is shown in Fig. 2.4. The phase windings of both rotor and stator are spaced 120 degree electrical apart from each other. In the frame of reference attached to the stationary stator, the voltage equations for the stator are as given below:
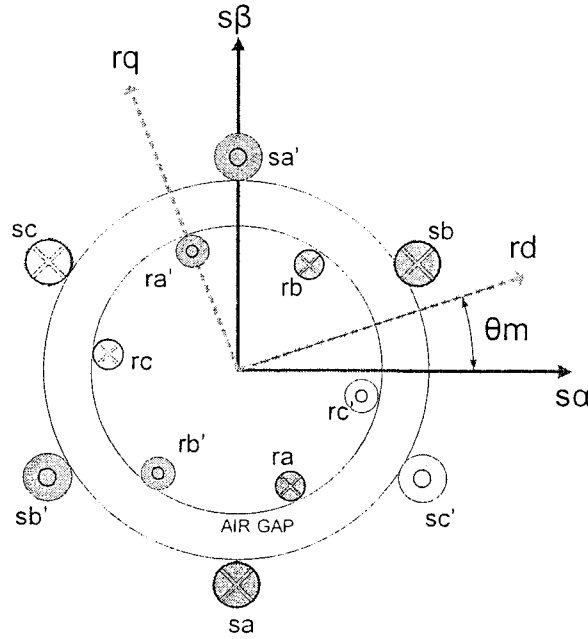

Fig. 2.4: Schematic diagram of an IM

20

$$v_{sa} = R_s i_{sa} + \frac{d}{dt}(\psi_{sa}) \qquad\qquad (2.5.a)$$

$$v_{sb} = R_s i_{sb} + \frac{d}{dt}(\psi_{sb}) \qquad\qquad (2.5.b)$$

$$v_{sc} = R_s i_{sc} + \frac{d}{dt}(\psi_{sc}) \qquad\qquad (2.5.c)$$

Following the same pattern the mathematical relations for the rotor voltages in the rotor's frame of reference can be expressed as:

$$v_{ra} = R_r i_{ra} + \frac{d}{dt}(\psi_{ra}) \qquad\qquad (2.6.a)$$

$$v_{rb} = R_r i_{rb} + \frac{d}{dt}(\psi_{rb}) \qquad\qquad (2.6.b)$$

$$v_{rc} = R_r i_{rc} + \frac{d}{dt}(\psi_{rc}) \qquad\qquad (2.6.c)$$

Considering all the magnetic interactions between stator and rotor, the total flux linkage of each stator phase wingding is given below:

$$\psi_{sa} = L_s i_{sa} + M_s i_{sb} + M_s i_{sc} + M_{sr} i_{ra} \cos\theta_m + M_{sr} i_{rb} \cos(\theta_m + {}^{2\pi}/_3) + M_{sr} i_{rc} \cos(\theta_m + {}^{4\pi}/_3) \qquad (2.7.a)$$

$$\psi_{sb} = L_s i_{sb} + M_s i_{sa} + M_s i_{sc} + M_{sr} i_{rb} \cos\theta_m + M_{sr} i_{rc} \cos(\theta_m + {}^{2\pi}/_3) + M_{sr} i_{ra} \cos(\theta_m + {}^{4\pi}/_3) \qquad (2.7.b)$$

$$\psi_{sc} = L_s i_{sc} + M_s i_{sa} + M_s i_{sb} + M_{sr} i_{rc} \cos\theta_m + M_{sr} i_{ra} \cos(\theta_m + {}^{2\pi}/_3) + M_{sr} i_{rb} \cos(\theta_m + {}^{4\pi}/_3) \qquad (2.7.c)$$

Similarly, for each rotor phase, the flux linkages are given below:

$$\psi_{ra} = L_r i_{ra} + M_r i_{rb} + M_s i_{rc} + M_{sr} i_{sa} \cos(-\theta_m) + M_{sr} i_{sb} \cos(-\theta_m + {}^{2\pi}/_3) + M_{sr} i_{sc} \cos(-\theta_m + {}^{4\pi}/_3) \quad (2.8.a)$$

$$\psi_{rb} = L_r i_{rb} + M_r i_{ra} + M_r i_{rc} + M_{sr} i_{sb} \cos(-\theta_m) + M_{sr} i_{sc} \cos(-\theta_m + {}^{2\pi}/_3) + M_{sr} i_{sa} \cos(-\theta_m + {}^{4\pi}/_3) \quad (2.8.b)$$

$$\psi_{rc} = L_r i_{rc} + M_r i_{ra} + M_r i_{rb} + M_{sr} i_{sc} \cos(-\theta_m) + M_{sr} i_{sa} \cos(-\theta_m + {}^{2\pi}/_3) + M_{sr} i_{sb} \cos(-\theta_m + {}^{4\pi}/_3) \quad (2.8.c)$$

21

Ψ, L & M stand for flux linkage, self inductance and mutual inductance, respectively. The first subscript e.g. 'r', 's' stands for the rotor and stator of the IM. θ_m stands for the rotor mechanical angle with respect to the stationary stator frame.

Combining all the equations from (2.1.a) to (2.8.c), the matrix form for the voltage mathematical model of IM can be obtained as:

$$
\begin{bmatrix} v_{sa} \\ v_{sb} \\ v_{sc} \\ v_{ra} \\ v_{rb} \\ v_{rc} \end{bmatrix} =
\begin{bmatrix}
R_s + pL_s & pM_s & pM_s & pM_{sr}\cos\theta_m & pM_{sr}\cos\theta_1 & pM_{sr}\cos\theta_2 \\
pM_s & R_s + pL_s & pM_s & pM_{sr}\cos\theta_2 & pM_{sr}\cos\theta_m & pM_{sr}\cos\theta_1 \\
pM_s & pM_s & R_s + pL_s & pM_{sr}\cos\theta_1 & pM_{sr}\cos\theta_2 & pM_{sr}\cos\theta_m \\
pM_{sr}\cos\theta_m & pM_{sr}\cos\theta_2 & pM_{sr}\cos\theta_1 & R_r + pL_r & pM_r & pM_r \\
pM_{sr}\cos\theta_1 & pM_{sr}\cos\theta_m & pM_{sr}\cos\theta_2 & pM_r & R_r + pL_r & pM_r \\
pM_{sr}\cos\theta_2 & pM_{sr}\cos\theta_1 & pM_{sr}\cos\theta_m & pM_r & pM_r & R_r + pL_r
\end{bmatrix}
\begin{bmatrix} i_{sa} \\ i_{sb} \\ i_{sc} \\ i_{ra} \\ i_{rb} \\ i_{rc} \end{bmatrix}
\quad (2.9)
$$

Equation (2.9) can be rewritten as:

$$
\begin{bmatrix} v_{sa} \\ v_{sb} \\ v_{sc} \\ v_{ra} \\ v_{rb} \\ v_{rc} \end{bmatrix} =
\begin{bmatrix}
R_s & 0 & 0 & 0 & 0 & 0 \\
0 & R_s & 0 & 0 & 0 & 0 \\
0 & 0 & R_s & 0 & 0 & 0 \\
0 & 0 & 0 & R_r & 0 & 0 \\
0 & 0 & 0 & 0 & R_r & 0 \\
0 & 0 & 0 & 0 & 0 & R_r
\end{bmatrix}
\begin{bmatrix} i_{sa} \\ i_{sb} \\ i_{sc} \\ i_{ra} \\ i_{ra} \\ i_{ra} \end{bmatrix}
+ p
\begin{bmatrix}
L_s & M_s & M_s & M_{sr}\cos\theta_m & M_{sr}\cos\theta_1 & M_{sr}\cos\theta_2 \\
M_s & L_s & M_s & M_{sr}\cos\theta_2 & M_{sr}\cos\theta_m & M_{sr}\cos\theta_1 \\
M_s & M_s & L_s & M_{sr}\cos\theta_1 & M_{sr}\cos\theta_2 & M_{sr}\cos\theta_m \\
M_{sr}\cos\theta_m & M_{sr}\cos\theta_2 & M_{sr}\cos\theta_1 & L_r & M_r & M_r \\
M_{sr}\cos\theta_1 & M_{sr}\cos\theta_m & M_{sr}\cos\theta_2 & M_r & L_r & M_r \\
M_{sr}\cos\theta_2 & M_{sr}\cos\theta_1 & M_{sr}\cos\theta_m & M_r & M_r & L_r
\end{bmatrix}
\begin{bmatrix} i_{sa} \\ i_{sb} \\ i_{sc} \\ i_{ra} \\ i_{rb} \\ i_{rc} \end{bmatrix}
\quad (2.10)
$$

where

$$\theta_1 = \theta_m + \frac{2\pi}{3} \qquad (2.11)$$

$$\theta_2 = \theta_m + \frac{4\pi}{3} \qquad (2.12)$$

This model is non-linear since it contains the parameters like rotor position which is a non-linear function of time. Additionally, under saturation conditions, the inductances may go under variation with currents. This model is too complex because it contains a bundle of mutual inductances

22

2.1.2 Space Phasor Model in Two Axes.

Park's transformation can be used to convert a, b, c to α-β frame as:

$$\begin{bmatrix} v_{s0} \\ v_{s\alpha} \\ v_{s\beta} \end{bmatrix} = \frac{2}{3} \begin{bmatrix} 1/\sqrt{2} & 1/\sqrt{2} & 1/\sqrt{2} \\ \cos\theta & \cos(\theta - 2\pi/3) & \cos(\theta + 2\pi/3) \\ -\sin\theta & -\sin(\theta - 2\pi/3) & -\sin(\theta + 2\pi/3) \end{bmatrix} \begin{bmatrix} v_{sa} \\ v_{sb} \\ v_{sc} \end{bmatrix} \tag{2.13}$$

The inverse Park's transformation can be written as:

$$\begin{bmatrix} v_{sa} \\ v_{sb} \\ v_{sc} \end{bmatrix} = \frac{\sqrt{2}}{3} \begin{bmatrix} 1/\sqrt{2} & \cos\theta & -\sin\theta \\ 1/\sqrt{2} & \cos(\theta - 2\pi/3) & -\sin(\theta - 2\pi/3) \\ 1/\sqrt{2} & \cos(\theta + 2\pi/3) & -\sin(\theta + 2\pi/3) \end{bmatrix} \begin{bmatrix} v_{s0} \\ v_{s\alpha} \\ v_{s\beta} \end{bmatrix} \tag{2.14}$$

The rotor position angle is defined as,

$$\theta_m(t) = \int_0^t \omega_m \, dt + \theta_m(0) \tag{2.15}$$

where θ_m defines the position of rotor or ω_m is the mechanical rotor speed.

Applying Park's transformation to (2.9) one can get

$$\begin{bmatrix} v_{s\alpha} \\ v_{s\beta} \\ v_{rd} \\ v_{rq} \end{bmatrix} = \begin{bmatrix} R_s + pL_s & -L_s p\theta & pL_m & -L_m(P\omega_m + p\theta_m) \\ L_s p & R_s + pL_s & L_m(P\omega_m + p\theta_m) & pL_m \\ pL_m & L_m(p\theta_s - P\omega_m) & R_r + pL_r & L_r p\theta_m \\ L_m(p\theta - P\omega_m) & pL_m & L_r p\theta_m & R_r + pL_s \end{bmatrix} \begin{bmatrix} i_{s\alpha} \\ i_{s\beta} \\ i_{rd} \\ i_{rq} \end{bmatrix} \tag{2.16}$$

Since the end ring bars in a squirrel cage IM short circuit the winding conductors, therefore,

$$v_{rd} = v_{rq} = 0$$

And for the synchronously rotating frame,

ω$_s$ =0

therefore,   ω$_r$ = -ω$_m$

applying these changes to (2.16) we get,

$$\begin{bmatrix} v_{s\alpha} \\ v_{s\beta} \\ 0 \\ 0 \end{bmatrix} = \begin{bmatrix} R_s + pL_s & 0 & pL_m & 0 \\ 0 & R_s + pL_s & 0 & pL_m \\ pL_m & P\omega_m L_m & R_r + pL_r & P\omega_m L_r \\ -PL_m\omega_m & pL_m & -P\omega_m L_r & R_r + pL_s \end{bmatrix} \begin{bmatrix} i_{s\alpha} \\ i_{s\beta} \\ i_{rd} \\ i_{rq} \end{bmatrix} \qquad (2.17)$$

This model is free from and trigonometric function of rotor position. It involves comparatively very few types of impedance as compared to model (2.9).

Overall, this equation is much simpler compared to the relevant equation in three phasor form.

2.1.3. IM Space Phasor Model in Steady-State

The stator and rotor voltage space phasor in the frame of reference attached to stationary stator, can be written as:

$$\vec{v_s} = R_s \vec{i_s} + \frac{d}{dt}\left(\vec{\psi_s}\right) \qquad (2.18)$$

$$\vec{v'_r}e^{-j\theta m} = R_r \vec{i'_r}e^{-j\theta m} + \frac{d}{dt}(\vec{\psi'_r}e^{-j\theta m}) \qquad (2.19)$$

Equation (2.19) can be simplified as:

$$\vec{v'_r} = R_r \vec{i'_r} + \frac{d}{dt}\left(\vec{\psi'_r}\right) - j.Pw_m \vec{\psi'_r} \qquad (2.20)$$

Similarly, in general the flux linkage space phaors with reference to same stator frame of reference can be written as:

$$\vec{\psi_s} = L_s \vec{i_s} + L_m \vec{i'_r} \qquad (2.21)$$

$$\vec{\psi'_r} = L_r \vec{i'_r} + L_m \vec{i_s} \qquad (2.22)$$

24

Ideally, when an IM is supplied by a symmetrical sinusoidal supply, in steady state the space vectors behave like phasor. Hence the following mathematical relations become valid in steady state condition.

$$\overrightarrow{V_s} = V_s \tag{2.23}$$

$$\frac{d}{dt}\left(\overrightarrow{I_s}\right) = j\,\omega_s I_s \tag{2.24}$$

$$\overrightarrow{v'_r} = V'_r e^{j\theta} \tag{2.25}$$

$$\frac{d}{dt}\left(\overrightarrow{i'_r}\right) = j\,\omega_r I'_r + jP\omega_m I'_r \tag{2.26}$$

The voltage equations (2.18) and (2.20) may be rewritten as:

$$\overrightarrow{V_s} = R_s \overrightarrow{i_s} + \left(L_{sl} + \frac{3}{2L_{sm}}\right)\frac{d}{dt}\left(\overrightarrow{i_s}\right) + \frac{3}{2}\,L_{rm}\,\frac{d}{dt}\left(\overrightarrow{i'_r}\right) \tag{2.27}$$

$$\overrightarrow{v'_r} = R_r \overrightarrow{i'_r} + \left(L_{rl} + \frac{3}{2L_{rm}}\right)\frac{d}{dt}\left(\overrightarrow{i'_r}\right) + \frac{3}{2}\,L_{sm}\,\frac{d}{dt}\left(\overrightarrow{i_s}\right) - jP\omega_m\left\{(L_{rl} + 3/2L_{rm})\overrightarrow{i'_r} + 3/2L_{sm}\overrightarrow{i_s}\right\} \tag{2.28}$$

By applying the steady state equations from (2.23-2.26) and short circuit condition squirrel cage rotor we get:

$$V_s = R_s I_s + j\omega_s(L_{sl} + 3/2L_{sm})I_s + j3/2\omega_s L_{sm}I'_r \tag{2.29}$$

$$0 = \frac{R_r}{s}I'_r + j\omega_s(L_{rl} + 3/2L_{sm})I'_r + j3/2\omega_s L_{sm}I_s \tag{2.30}$$

25

On the basis of these equations and using Kirchhoff's voltage law we can draw the circuit of an IM under steady state conditions as shown in Fig. 2.5.
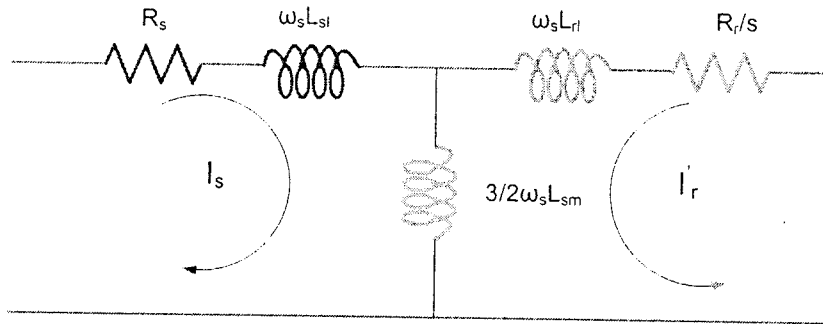

Fig. 2.5: Model of Squirrel cage IM in steady state

2.2 IM Torque Production

The developed torque of an IM for balanced three phase IM is given by [19].

$$T_e = \frac{3}{2} (\overrightarrow{\psi_S} \; X \; \overrightarrow{i'_r})$$ (2.31)

or

$$T_e = \frac{3}{2} P |\overrightarrow{\psi_S}| \; |\overrightarrow{i'_r}| \sin \theta_{sr}$$ (2.32)

or

$$T_e = \frac{3}{2} P |\overrightarrow{\psi_S}| \; |\overrightarrow{\psi_r}| \sin \theta_{sr}$$ (2.33)

26

Equation (2.33) indicates that for maximum torque generation the rotor and stator flux linkage vectors ($\psi_{s\ and}$ ψ_r) must be orthogonal to each other. In DC machines this feature is inherently exists. While in AC machines this property of vectors needs to be fabricated. In AC machines both these quantities are inter dependent and their position in space depends on both the stator and rotor positions. The control of squirrel cage IM adds further complexity due to inaccessibility of rotor winding. So the requirement is to make these quantities decoupled and be controlled independently. This is achieved by vector control scheme.

By Faraday's electromagnetic theory for two coils mutually coupled in the magnetic field of each other

$$\overrightarrow{\psi_s} = L_s \overrightarrow{i_s} + L_m \overrightarrow{i'_r} \tag{2.34}$$

$$\overrightarrow{\psi_r} = L_r \overrightarrow{i'_r} + L_m \overrightarrow{i_s} \tag{2.35}$$

Decomposing these flux linkage equations into real and imaginary part and then plug into torque equation one can get:

$$T_e = \frac{3}{2} P (\psi_{s\beta} * I_{s\alpha} + \psi_{s\alpha} * I_{s\beta}) \tag{2.36}$$

This equation will be used for estimation of developed torque for direct torque control scheme.

27

CHAPTER 3

Fundamentals of Hysteresis Band Adapted DTC Scheme

3.1 Introduction to Vector Control Schemes

Principally, there are two vector control techniques for the control of AC machines, named as direct vector control and indirect vector control. The first technique needs measurement/estimation of the machine stator and/or rotor flux linkage vector amplitude and position. Contrarily, latter requires machine model e.g. in case of induction motor slip relation etc. Hence, indirect vector technique is least motor parameter dependent. Different application still need indirect vector technique since at low frequencies they have comparatively better performance. In the development of motor theory, it is very common assumption that the mechanical time constant is very large compared to electrical time constant. This is valid only for the machines with high inertia. If in vector control, incorrect magnitude and position of flux linkage space vectors is used then the independent control of the machine flux and torque is lost. This factor degrades both the transient and steady state performance.

Today, there are many control schemes proposed by authors/researchers in books and research papers. But only few of them have industrial application. In order to design some control system for the motor drive we have to keep in mind the current industry requirements. If

we keenly observe, the motor drive industry is looking for the control scheme which has the following capabilities:

- A universal drive i.e. a single drive capable of bridging all needs for application irrespective of AC, DC or servo purposes.

- Faster torque and accurate position/speed responses.

- Free from sensor for economical reasons.

- Globally stable system with minimum down time i.e. it avoids unnecessary tripping of the system.

- Unaffected by interference like harmonics and radio frequency interference (RFI).

- Unaffected by system disturbances.

- Minimum running noise.

From either constant v/f or scalar technique to FOC scheme, none of the techniques meet all these requirements. We have to compromise between economy and accuracy requirements. The direct torque control is the latest and most effective ac drive technique [20]. It encompasses majority of the industrial demands.

3.1.1 Advantages of DTC Scheme

The DTC scheme has following preferences over its competitive FOC scheme:

- The FOC uses frequency and voltage as control parameter and needs pulse width modulation (PWM) as a control medium. For DTC scheme, there is no need of PWM.

- DTC uses torque and flux as control parameters that directly relate to the motor itself. Thus, the DTC scheme avoids the interface circuits and hence, becomes simpler.

- The static stator frame is used as a reference frame in this scheme. All the parameters used in the scheme also belong to stator. Therefore, it does not need any coordinate transformation to a synchronously rotating frame which is necessary for FOC scheme.

- DTC scheme needs only stator resistance as a motor parameter. The stator winding being static undergoes lesser variation during system operation as compared to rotor resistance.

- DTC scheme has faster dynamic speed recovery. It directly controls motor torque and field and hence response is faster as compared to FOC scheme, which indirectly control these parameters. According to ABB, it is 10 times faster than FOC scheme [19].

- DTC scheme is economical. For torque control, it does not require any sensor/observer for closed loop control. It estimates motor torque and flux using motor model. The FOC scheme requires sensor/observer for closed loop operation.

- By optimizing the motor flux, DTC scheme can make the system energy efficient. This feature helps to improve system efficiency with variable speed/load pumps.

- It provides very accurate torque control even at low frequencies. With or without any feedback sensor and even at zero speed it can supply the full load torque [20]. This feature also reduces the motor noise compared to VSD with high switching frequency PWM.

- DTC scheme provides rapid starting for the drive system irrespective of residual magnetism and mechanical load.

These features indicate that DTC scheme based motor drives are most suitable for HPD applications in future. The sole requirement is to eliminate/optimize some of operational drawbacks of this scheme.

3.1.2 Drawbacks of DTC Scheme

Despite numerous advantages of the DTC scheme, inherently, it has some limitations. The major drawbacks are as follows:

- DTC scheme controls the motor torque and flux directly. Therefore, ripples produced in these control parameters are larger. It causes motor vibration.

- This scheme is motor parameter dependent. The estimation of motor torque and flux involves the stator resistance. This parameter varies slightly during motor operation and needs some adaptive algorithm.

- It is difficult to start the motor with this scheme. This problem arises due to difficulties in torque and flux estimation at the start.

- Motor flux estimation involves an integral operation. This also adds the start up problems.

- DTC scheme for its proper functioning needs a very high frequency processor to keep the torque ripple within standard limits.

3.2. Critical Analysis of DTC Scheme

3.2.1 Conventional DTC Scheme

The stator flux linkage based basic DTC scheme is shown in Fig.3.1. Other forms of DTC scheme like rotor flux-based and magnetizing flux linkage based are also feasible [19].

31

However, in this thesis conventional DTC means always the stator flux linkage based DTC scheme.

The motor stator flux is estimated by using equation (2.18)

$$\psi_{s\alpha} = \int_0^t (V_{s\alpha} - R_s I_{s\alpha})\ dt \tag{3.1}$$

$$\psi_{s\beta} = \int_0^t (V_{s\beta} - R_s I_{s\beta})\ dt \tag{3.2}$$

It shows that the accuracy of flux linkage measurements depend on how accurate the sensors are used for measuring stator voltages, currents and integration technique.

The modulus of stator flux linkage is given by:

$$|\psi_s| = \sqrt{(\psi_{s\alpha}^2 + \psi_{s\beta}^2)} \tag{3.3}$$

However, the accuracy of this flux estimation may be highly unreliable at low frequencies due to the stator resistance variation, integral drift and noise. The solution to this problem is discussed in Section 3.2.2.
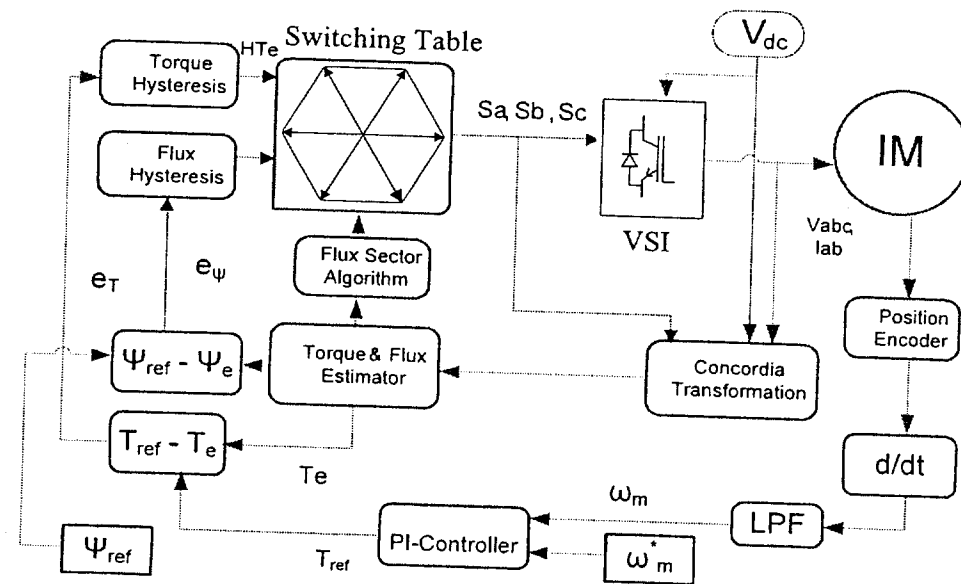
Fig. 3.1: Flow diagram of conventional DTC

32

The motor developed torque is estimated by using equation (2.36) as follows,

$$T_e = \frac{3}{2} P (\psi_{s\beta} * I_{s\alpha} + \psi_{s\alpha} * I_{s\beta})$$ (3.4)

These estimated values are compared with their reference/command values and the error signals (e_ψ and e_T) proceed to the corresponding hysteresis comparators. The flux linkage hysteresis comparator is of two, while torque hysteresis comparator is of three levels. The position of stator flux linkage is determined as,

$$\theta = \tan^{-1}(\psi_{s\beta} / \psi_{s\alpha})$$ (3.5)

Using this angle, the flux sector number (1 to 6) is determined by using the flux Simulink default sector algorithm shown in Fig. 3.2.
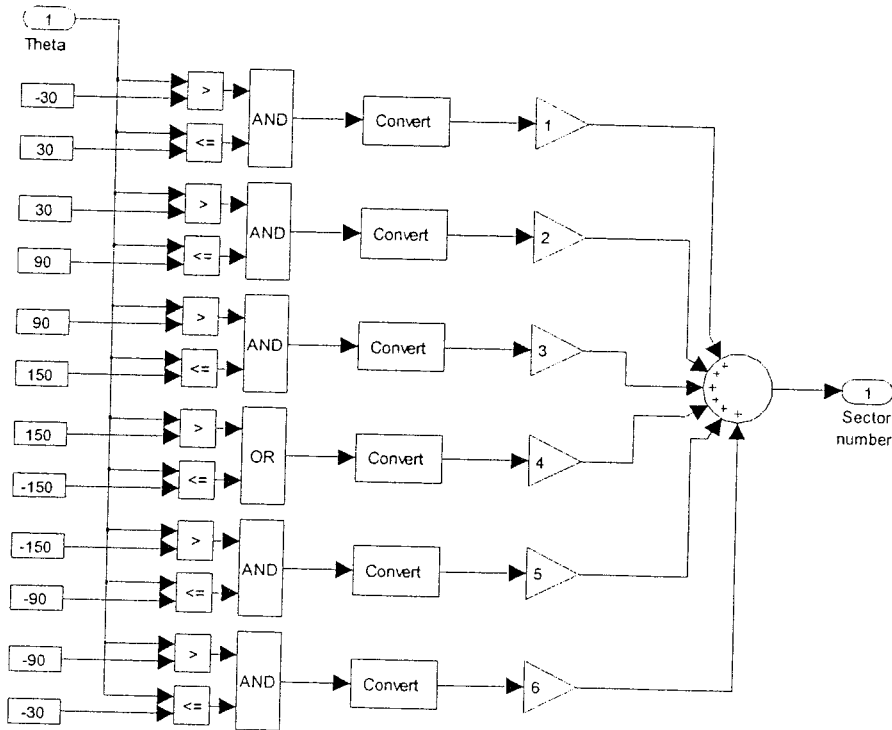
Fig. 3.2: Simulink diagram for flux linkage sector number determination

33

The two digits produced by hysteresis comparators and one by flux position are collectively used to trigger the switches of the VSI by selecting appropriate voltage vector using the optimizing switching lookup table (Table-1) shown below. This appropriate voltage vector keeps the motor flux and torque within their specified band limits.

Table-1: Look-up table for DTC switching

flux	torque	Sector (Sn)					
$H\psi_s$	HT_e	S1	S2	S3	S4	S5	S6
1	1	V2	V3	V4	V5	V6	V1
	0	V7	V0	V7	V0	V7	V0
	-1	V6	V1	V2	V3	V4	V5
-1	1	V3	V4	V5	V6	V1	V2
	0	V0	V7	V0	V7	V0	V7
	-1	V5	V6	V1	V2	V3	V4

The sectors of flux and possible eight inverter voltage vectors are shown in Fig. 3.3. It is worth to note that equation (3.5) gives the exact position of the stator flux linkage vector but for the DTC scheme it needs only the sector number of this vector. A simpler algorithm is proposed for sector determination in Section-3.3.
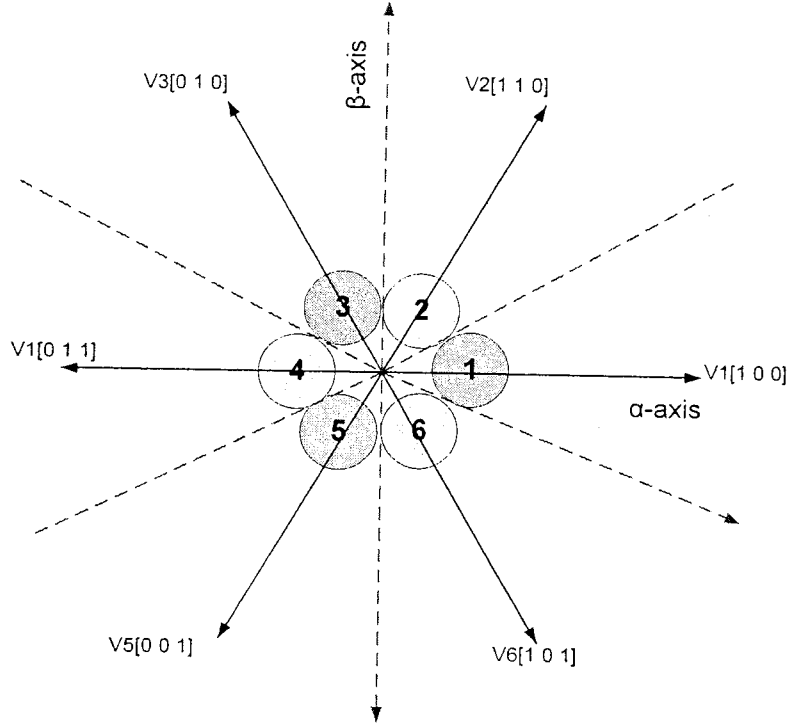
Fig. 3.3: Stator flux linkage sectors and inverter voltage vectors

3.2.2   Stator Flux Linkage and IM Developed Torque Analysis

This section critically analyse the control variables for DTC scheme i.e. stator flux linkage and motor developed torque. Further, it elaborates the different factors which affect these variables.

Using equation (2.18) stator flux linkage may be estimated as:

$$\psi_s = \frac{1}{T_N} \int_0^t (V_{s\alpha} - R_s\, I_{s\alpha})\ dt + \psi_{s0} \tag{3.6}$$

35

This estimation of flux involves integration. But the integration needs initial condition (ψ_{so}) during start-up operation. At low frequencies, the drift problem associated with pure open loop integrator introduces more complexities for real time implementation. At low speeds, the electrical signals (voltage and current) are dominated by the harmonics which causes inaccuracy in flux estimation.

These problems are resolved by just introducing a switch at the output of flux estimator. The threshold for the switch is greater than or equal to 30 rad/s. If the rotor speed is below the threshold then a constant magnitude of 0.2wb is passed through the switch. But over threshold the actual estimated value of flux is selected. The selection of initial flux is of critical importance. It should be possible low so as to be capable to run the motor. Figure 3.4 shows the simulation results by estimation flux linkage using prescribed technique for IM having rated flux of 0.75 wb.
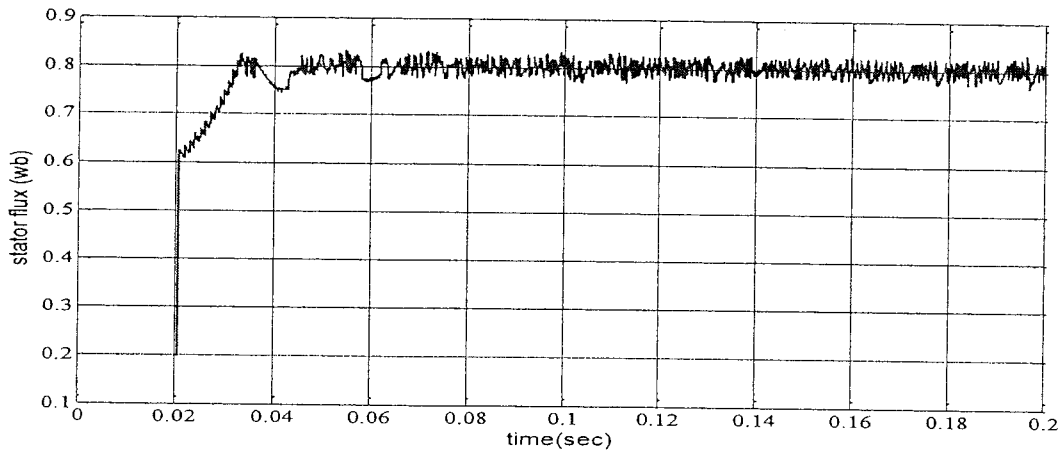
Fig. 3.4: Stator flux linkage including estimation at low speeds

By neglecting the stator resistance (Rs) in equation (3.6) it may be simplified as,

$$\Delta \psi_s = V_s \Delta t \tag{3.7}$$

$\Delta\psi_s$ is the change in stator flux caused by the application of new stator voltage vector. Equation (3.7) indicates that the change in stator flux is dependent on stator input voltage vector and the duration Δt for which this vector is applied. Figure 3.5 also shows the radial and tangential components of $\Delta\psi_{sr}$ and $\Delta\psi_{st}$ respectively.
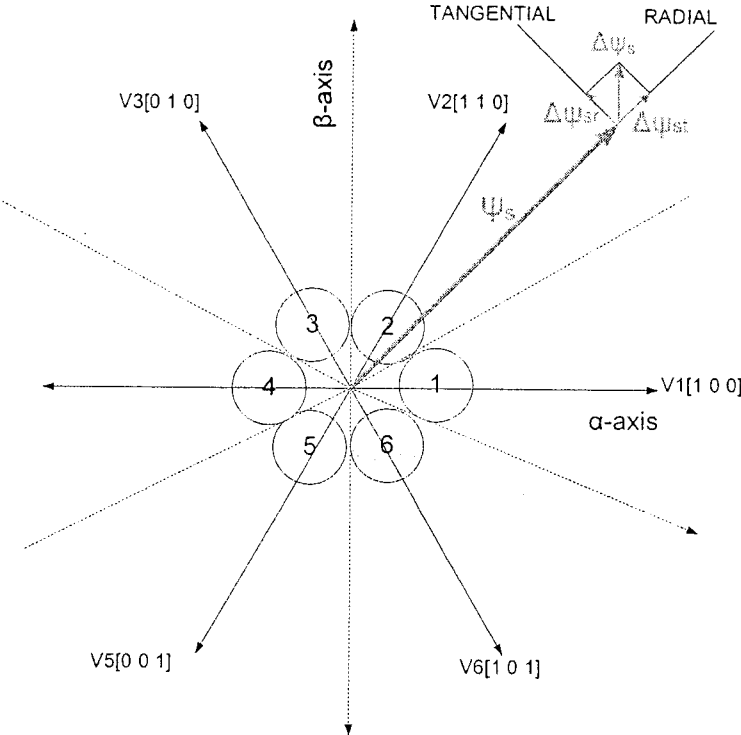

Fig. 3.5: Components of stator flux linkage

From Fig. 3.5, it can be observed that in order to increase ψ_s we must select a voltage vector which produces a higher radial component of $\Delta\psi_{sr}$.

Another form of equation (2.33) for the developed torque in IM is given using as [59],

37

$$T_e = P \frac{L_m}{\sigma \ L_s \ L_r} |\psi_s| * |\psi_r| \ \sin\theta_{sr} \tag{3.8}$$

Where $\qquad$ $Leakage \ Factor = \sigma = 1 - \dfrac{L_m^2}{L_s \ L_r}$ $\qquad$ (3.9)

P= number of pole pairs

ψ_s and ψ_r are the stator and rotor flux linkages respectively.

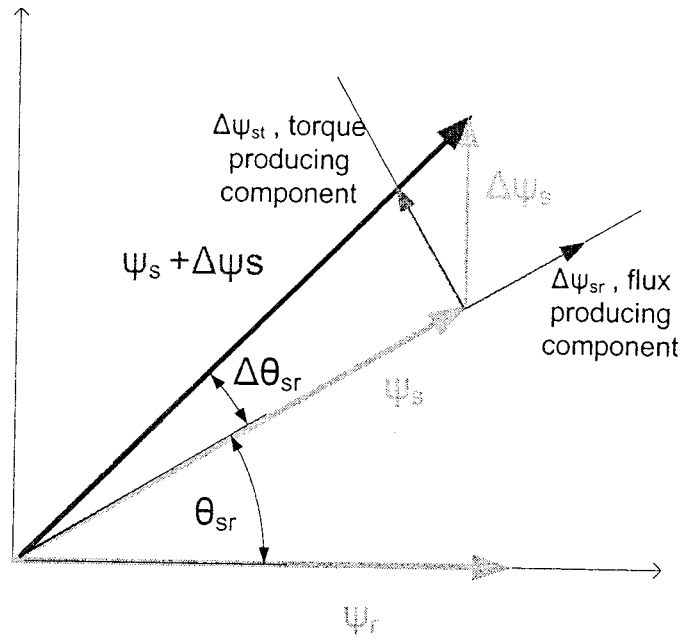L_s and L_r are the stator and rotor self inductance respectively.

Fig. 3.6: Rotor and stator flux linkage vectors

In the steady state $|\Delta\psi_r|$ & $|\Delta\psi_s|$ are almost constant and T_e depends on the torque angle θ_{sr}. Hence, a stator voltage vector which produces larger $\Delta\psi_{st}$ will control the torque more effectively. From Figure 3.6 it can be observed that forward switching of V_s causes rapid movement of ψ_s from ψ_r and thereby increasing θ_{sr} and T_e. When a zero stator voltage vector

(V_0, V_7) is applied, ψ_s stops while ψ_r continues to move forward, reducing θ_{sr} as well as T_e. If the application of zero vectors is sufficiently long enough so that ψ_r overtakes ψ_s vector, then θ_{sr} becomes negative [45]. It will produce the retarding torque. Hence, the duration of application of any stator voltage vector plays an important role on the torque ripple. By cyclic switching of active and zero stator voltage vectors we can control the motor torque with optimal level of the ripple. At low rotor speeds, the ψ_r motion is too slow to achieve rapid torque reduction. In such situation, instead of zero vectors, an active vector moving backward is preferred choice for effective torque control.

3.2.3 IM Torque Ripples Analysis

Under the influence of any active stator voltage vector, motor torque keeps on increasing or decreasing until it touches the boundary defined by torque hysteresis band. At next sampling interval, Table-1 is used to select another stator voltage vector which mitigates the effect of previous one. Due to the independent control of torque and flux, the torque ripple is only affected by the width of torque hysteresis band and is independent of the width of flux hysteresis band. But due to discrete nature of the control system, there might be still torque ripples even with zero width of hysteresis band. This is due to the limitation imposed on sampling period by the rated switching frequency and losses of the inverter.

The width of torque hysteresis band must be selected in such a way that the torque ripple level and switching frequency of the inverter are within limits. Too small band may result the selection of reverse voltage vector instead of zero vector and very high switching frequency of the VSI. Selection of reverse voltage vector may then cause the torque undershoots. Hence,

39

the torque ripple will become higher than hysteresis band limits. The torque slope is a function of

motor speed, stator voltage, stator flux, and rotor flux vectors and is given below [59]:

$$slope^+ = -\frac{T_{e(n)}}{\sigma\,\tau_{sr}} + \frac{3PL_m}{8\sigma L_s L_r}[(v_s - j\omega_m\psi_s)j\psi_r \qquad (3.10)$$

$$slope^- = -\frac{T_{e(n)}}{\sigma\,\tau_{sr}} + \frac{3PL_m}{8\sigma L_s L_r}[(-jw_m\psi_s)j\psi_r] \qquad (3.11)$$

$T_e(n)$ is the torque at nth sampling instant. Both of these equations are motor speed, ω_m

dependent. However, at lower speed positive slope is larger than negative slope. It means that the

time taken by torque to reach upper and lower band limits, as well as switching frequency, varies

with the rotor speed. This concept can be further consolidated by using the motor dynamic

equation. For simplicity neglecting the frictional losses this equation may be expressed as:

$$T_e = T_L + J\frac{d\omega_m}{dt} \qquad (3.12)$$

The speed error can be defined as,

$$\Delta\omega = \omega_m - \omega_m^* \qquad (3.13)$$

therefore, $\qquad\qquad T_e - T_L = J\frac{d}{dt}(\Delta\omega + \omega_m^*) \qquad (3.14)$

Since ω_m^* is a constant, therefore, this relation may be further simplified as:

$$\frac{d}{dt}(\Delta\omega) = \frac{T_e - T_L}{J} \qquad (3.15)$$

This relation indicates that slope of speed error is a good approximation of torque ripples.

3.3 Algorithm for determination of Stator Flux Linkage Sector Number

It has already been discussed how to find the current sector number of stator flux

linkage space vector in Section 3.2.1. The calculation involves a trigonometric function (tangent)

and then an algorithm to find the current sector number of stator flux linkage. The microprocessor evaluates the trigonometric function by using time consuming complex calculations as compared to normal arithmetic relations [60]. The requirement for the DTC scheme is only the current sector number of the stator flux linkage vector and not its accurate position. Keeping in view this reality, this thesis proposes a simple algorithm to find the current sector of the stator flux linkage vector. The algorithm is based on logic decisions and needs only a digit-by-digit calculation to do the job. The division of stator voltage vectors in four quadrants is shown in Fig.3.7. The flow diagram of the proposed algorithm is shown in Figure.3.8.
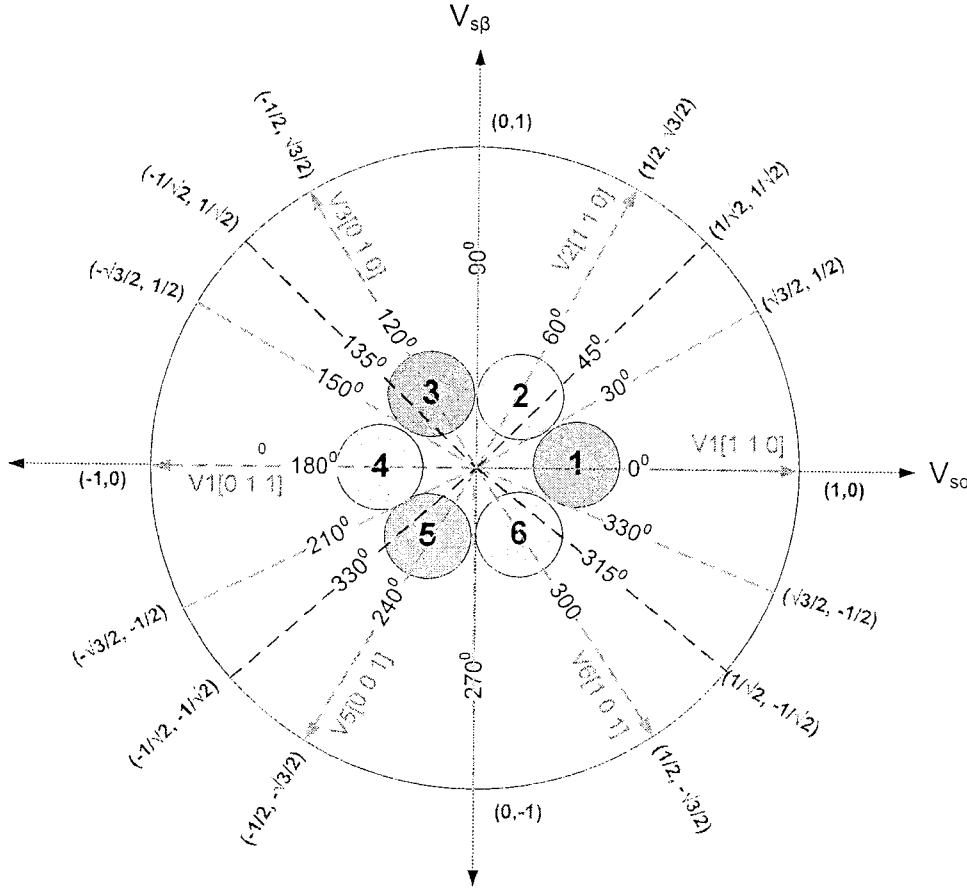
Fig. 3.7: Stator voltage vectors and stator flux linkage sectors.

41

$\Psi_{s\alpha}, \Psi_{s\beta}$

Yes

$\Psi_{s\alpha} \geq 0$

No

n=1,2,6

n=3,4,5

$\Psi_{s\beta} \geq 0$

Y

N

n=1,2

n=1,6

$(\Psi_{s\alpha} - \sqrt{3}\,\Psi_{s\beta}) \geq 0$

$(\Psi_{s\alpha} + \sqrt{3}\,\Psi_{s\beta}) > 0$

Y

N

N

OR

n=1

n=2

n=6

$\Psi_{s\beta} \geq 0$

Y

N

n=3,4

n=4,5

$(\Psi_{s\alpha} + \sqrt{3}\,\Psi_{s\beta}) \geq 0$

$(\Psi_{s\alpha} - \sqrt{3}\,\Psi_{s\beta}) > 0$

Y

N

Y

N

OR

n=3

n=4

n=5
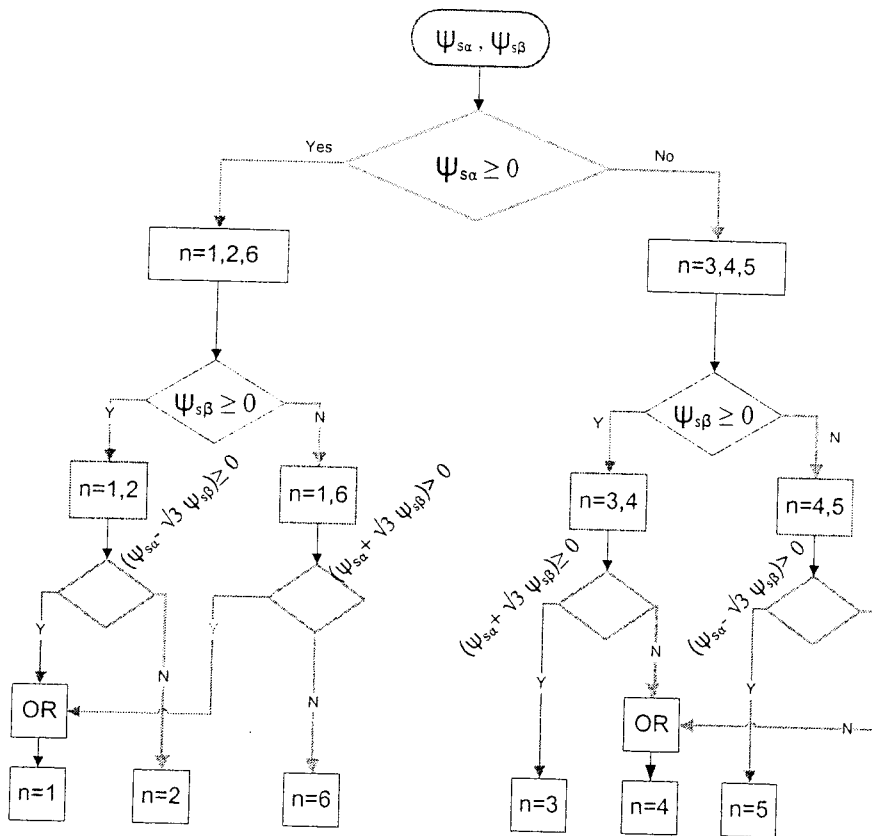
Fig. 3.8: Flow diagram for stator flux linkage sector selection algorithm.

Conventional sector algorithm

Proposed sectoralgorithm

Sector Number

Time(sec)
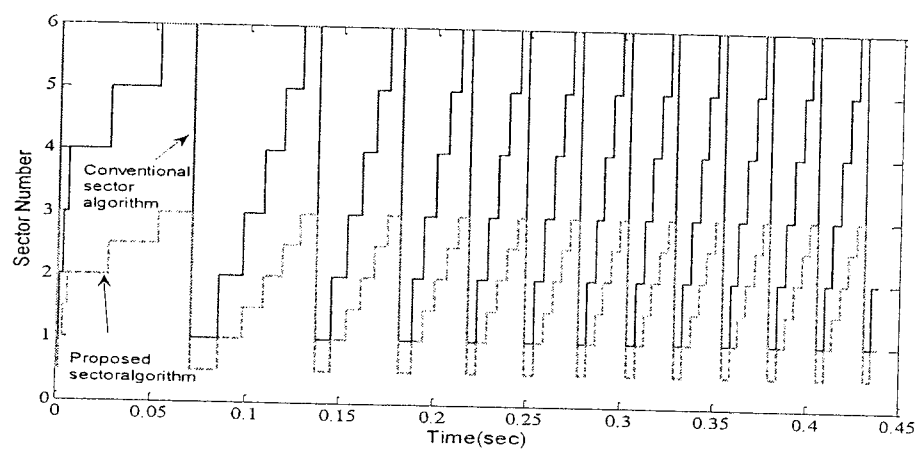
Fig. 3.9: Stator flux linkage sector for IM running at 120rad/s at 50% rated load (10Nm)

Figure 3.9 shows the simulation plots for DTC scheme operated by using conventional flux linkage sector number determination algorithm (continuous line graph) and by using proposed algorithm to do the same task (dashed line graph). The results for the proposed algorithm are scaled by factor ½ to avoid the overlapping of the two graphs. From Figure 3.9 it can easily be concluded that the proposed algorithm though simpler is functionally equivalent to the conventional algorithm.

3.4 Hysteresis Comparators for DTC Scheme

Two hysteresis comparators are used for basic DTC scheme. First one is used to control the stator flux linkage and the other to control the motor developed torque.

3.4.1 Conventional Hysteresis Comparators

Conventionally, both the hysteresis comparators used for DTC scheme have fixed band limits. The 2-level hysteresis comparator, used to keep the stator flux linkage within limits, is shown in Fig.3.10. The switching criteria for this hysteresis comparator is like an electric relay and may be defined as,

$$H\psi_s[n] = 1 \ \ if \ \ \Delta\psi_s > HB_{\psi U} \tag{3.16.a}$$

$$H\psi_s[n] = -1 \ \ if \ \ \Delta\psi_s < HB_{\psi L} \tag{3.16.b}$$

$$H\psi_s[n] = H\psi_s[n-1] \ \ if \ \ HB_{\psi L} \leq \Delta\psi_s \leq HB_{\psi U} \tag{3.16.c}$$

Where $HB_{\psi U}$ and $HB_{\psi L}$ denotes the upper and lower limits of flux linkage hysteresis comparator, respectively, $\Delta\Psi_s$ is the difference between command and actual value of the flux linkage,

43

$H\Psi_s[n]$ and $H\Psi_s[n-1]$ are the present and previous samples of flux hysteresis comparator output, respectively.
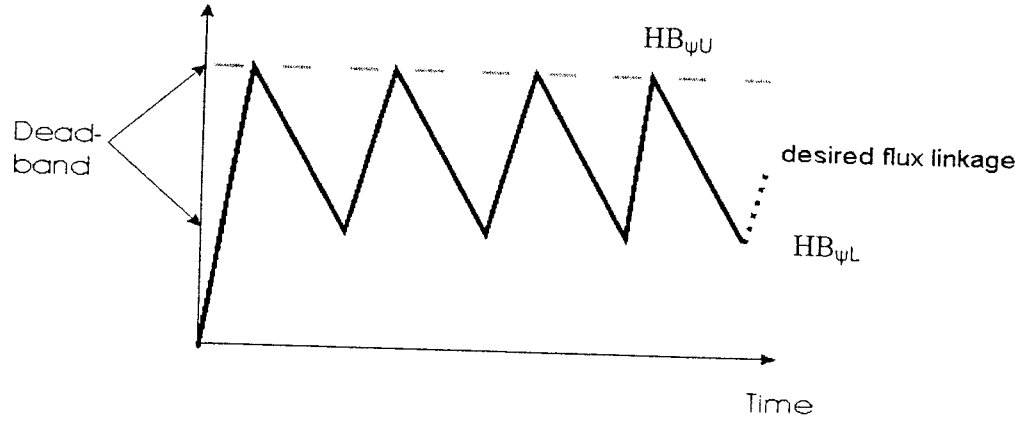
Fig.3.10: Two level stator flux linkage hysteresis comparator

According to author of [61], the three level hysteresis comparator is used to control the torque ripples of an IM and the switching criteria for this hysteresis comparator are defined as:

$$HT_e = 1 \ for \ T_e < (T_c - HB_{TU}) \tag{3.17.a}$$

$$HT_e = 0 \ for \ T_e = T_c \tag{3.17.b}$$

$$HT_e = -1 \ for \ T_e > (T_c - HB_{TL}) \tag{3.17.c}$$

HB_{TU} and HB_{TL} denote the upper and lower limits of torque hysteresis comparator, respectively. HT_e presents the output of the torque hysteresis comparator.

Due to the discrete nature of control system, equation (3.17.b) almost never satisfies i.e. application of zero vector from inverter is rare to occur. Consequently the powerful application of forward (1) and backward (-1) voltage vectors will control the system. This will increase the switching rate as well as ripples in negative torque area. Additionally, it will consume relatively

larger energy for control system due to extra energy utilized by backward inverter voltage vector to reduce the torque quickly.

The 3-level hysteresis comparator used for DTC scheme in Simulink library [62] is the parallel combination of two relays. The first relay has ON and OFF point HB_{TU} and zero respectively. While the second relay has ON and OFF point as zero and HB_{TL} respectively. The major drawback with this hysteresis comparator is that the second relay operates only if the application of zero voltage vectors fails to decrease the motor developed torque and it touches the lower limit of the hysteresis comparator. Conclusively, it is equivalent to reduce the bandwidth by half or to double the inverter switching frequency.

Both the conventional hysteresis comparators have fixed band limits. But the slope of the parameter they control (flux or torque) is variable. Due to discrete nature of the control system, a torque ripple with very high slope will cross the boundaries set by the hysteresis comparator if at the time of sampling it is slightly less than the band limit. This introduces very high ripples in the control variable and especially, in the case of motor torque it causes vibration of the motor.

3.4.2 Proposed Hysteresis Comparators

3.4.2.1 Torque Hysteresis Comparator

The proposed algorithm for the three level torque hysteresis comparator is shown in Fig.3.11. Digits 1,2 & 3 are used for 1, 0 & -1 in DTC Table-1, respectively. $HTe[n]$ and $HTe[n-1]$ are the current and previous samples of output digits produced by the torque hysteresis comparator, respectively. This proposed torque hysteresis may mathematically be modelled as:

$$HT_e[n] = 1 \quad if \quad \begin{cases} e_T[n] > HB_{TU} \\ OR \\ e_T[n] > K_0 \quad AND \quad HT_e[n-1] == 1 \end{cases} \tag{3.18.a}$$

$$HT_e[n] = 2 \quad if \quad \begin{cases} e_T[n] \leq HB_{TU} \quad AND \quad e_T[n] \geq HB_{TL} \quad AND \quad HT_e[n-1] \neq 1 \\ OR \\ e_T[n] \geq HB_{TL} \quad AND \quad e_T[n] \leq K_0 \end{cases} \tag{3.18.b}$$

$$HT_e[n] = 3 \quad if \; e_T[n] < HB_{TL} \tag{3.18.c}$$

The input-output curves for the proposed torque hysteresis comparator are shown in Fig.3.12. The value selected for HB_{TL}, HB_{TL} & K_0 are 1, -1 & -0.3 respectively. Both HB_{TL} and K_0 are negative numbers. The torque error, e_T is the difference between command and actual values of the IM torque. $e_T[n]$ and $e_T[n-1]$ denotes the current and previous torque error samples, respectively. The basic idea is to use the zero voltage vectors for reduction of the torque and to avoid the application of negative voltage vector to the possible limit.

This reduces the negative slope of the developed torque which tends to reduce switching rate from inverter and hence to reduce the torque ripples in negative torque region. Moreover, it saves the extra energy required to apply negative torque vector and hence make the system efficient. But in order to improve the system dynamics under varying loading conditions and to avoid big positive torque ripples, proposed hysteresis regulator applies negative voltage vector a small interval before HB_{TL} at point K_0. This margin is of critical nature. The value for K_0 and its distance from HB_{TL} is determined on the basis of simulation results of system characteristics under varying load and speed conditions.

46
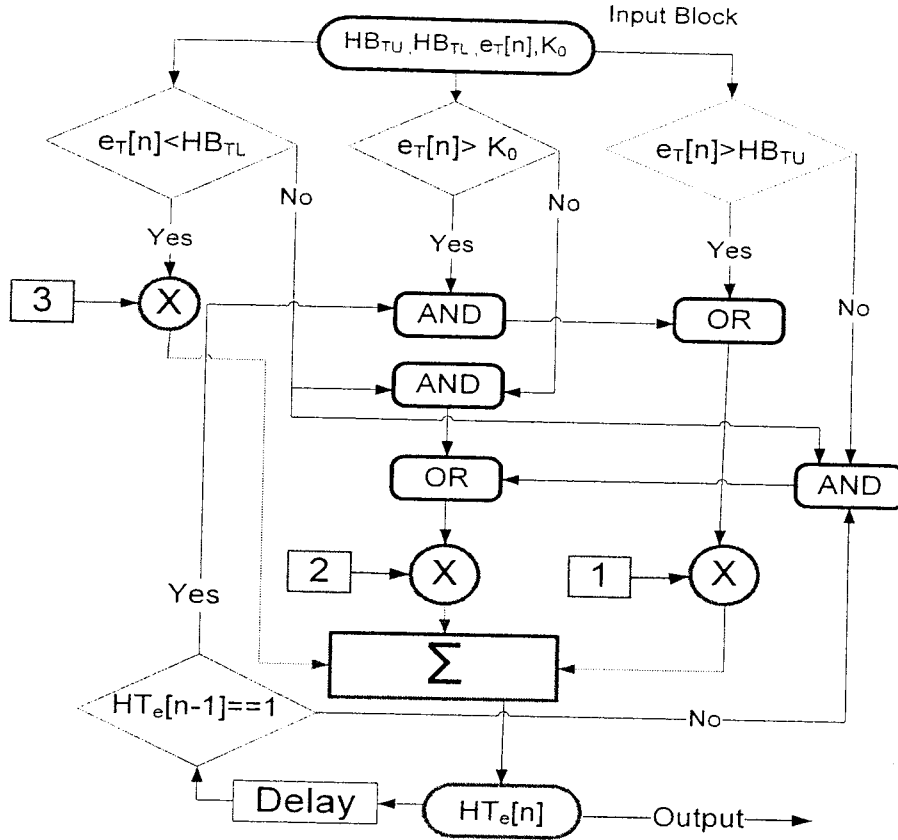
Fig. 3.11: Proposed three levels torque hysteresis comparator algorithm.
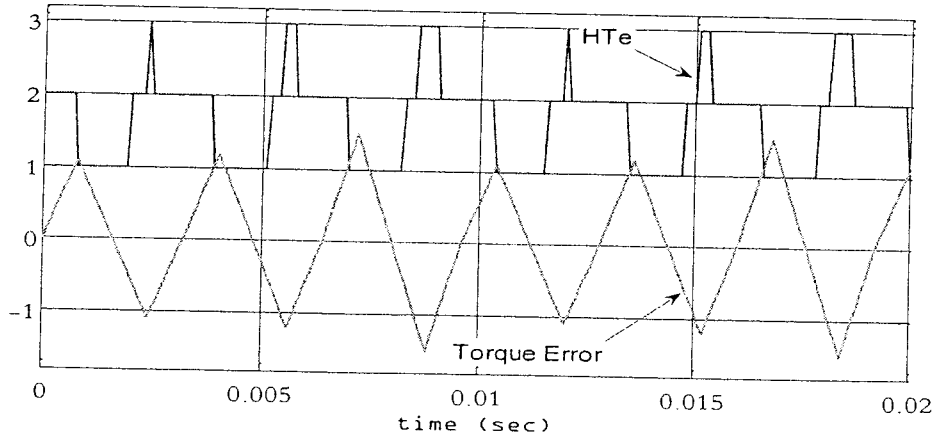
Fig. 3.12: Input Output curves for the proposed three levels torque hysteresis comparator.

The bandwidth of hysteresis is not constant in this scheme. The control of torque ripple is achieved through the dynamic change of the hysteresis bandwidth. The required change (ΔBW) is evaluated by using algorithm shown in Fig. 3.13.
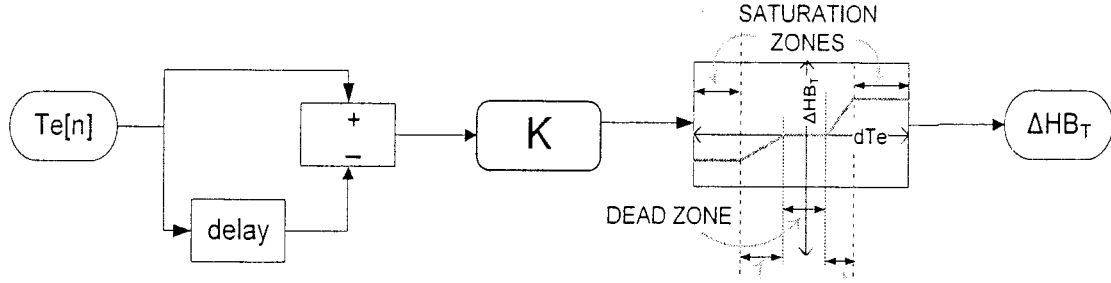

Fig. 3.13: Proposed bandwidth adaptation algorithm.

Once again the length of three zones is based on simulation results of the system response under variable conditions. Most effective part is the critical zone. The change in current bandwidth is predicted on the basis of change in estimated torque in previous sampling time. Net upper and lower band limits of the torque hysteresis are given by:

$$HB_{TU}^{n} = HB_{TU} - K_{TU} * \Delta HB_{T} \tag{3.19}$$

$$HB_{TL}^{n} = HB_{TL} + K_{TL} * \Delta HB_{T} \tag{3.20}$$

The values of the scaling factors K_{TL} and K_{TU} used for the present work are 0.14 and 0.1 respectively. The net bandwidth is so selected that the torque peaks (both positive and negative around set position) remain near to the boundaries (HB_{TU} , HB_{TL}) within permissible small deviations. Due to the limitation imposed by maximum switching rate of the inverter, it is almost impossible that the peaks of torque always touch the maximum defined limits.

48

3.4.2.2 Flux Hysteresis Comparator

Since the fit has only two levels The criteria for band adaption of flux hysteresis regulator are simple as compared to torque regulator.. The slope of stator flux linkage is determined as

$$\Delta \psi s = \psi s\,(n) - \psi s\,(n-1)$$

(3.21)

where 'n' stands for present and 'n-1' for previous sample value.

The variation in bandwidth of flux hysteresis controller is based on the slope of flux and the algorithm is similar to the torque hysteresis comparator which is shown in Fig.3.13. Principally, larger is the flux slope smaller is the net bandwidth. Remember that flux hysteresis is of two levels like a relay. After following the same steps like adapted band torque hysteresis, the net adapted band limits for the flux hysteresis comparator are given below:

$$HB_{\psi U}^{n} = HB_{\psi U} - K_{\psi U} * \Delta HB_{\psi}$$

(3.22)

$$HB_{\psi L}^{n} = HB_{\psi L} + K_{\psi L} * \Delta HB_{\psi}$$

(3.23)

$K_{\psi L}$ and $K_{\psi U}$ are the scaling factors. The values used for these constant for the present work are 0.214 and 0.214 respectively. The net bandwidth is so selected that the torque peaks (both positive and negative around set position) remain near to the boundaries ($HB_{\psi U}$, $HB_{\psi L}$) within permissible small deviations.

3.5 Performance Investigation

To investigate the performance of the proposed variable band hysteresis controllers based direct torque control scheme for an IM drive, a simulation model is developed using Matlab/Simulink

software [62]. The overall block diagram of the simulation model is shown in Fig. 3.14. The subsystems of Simulink model are attached in Appendix-B.
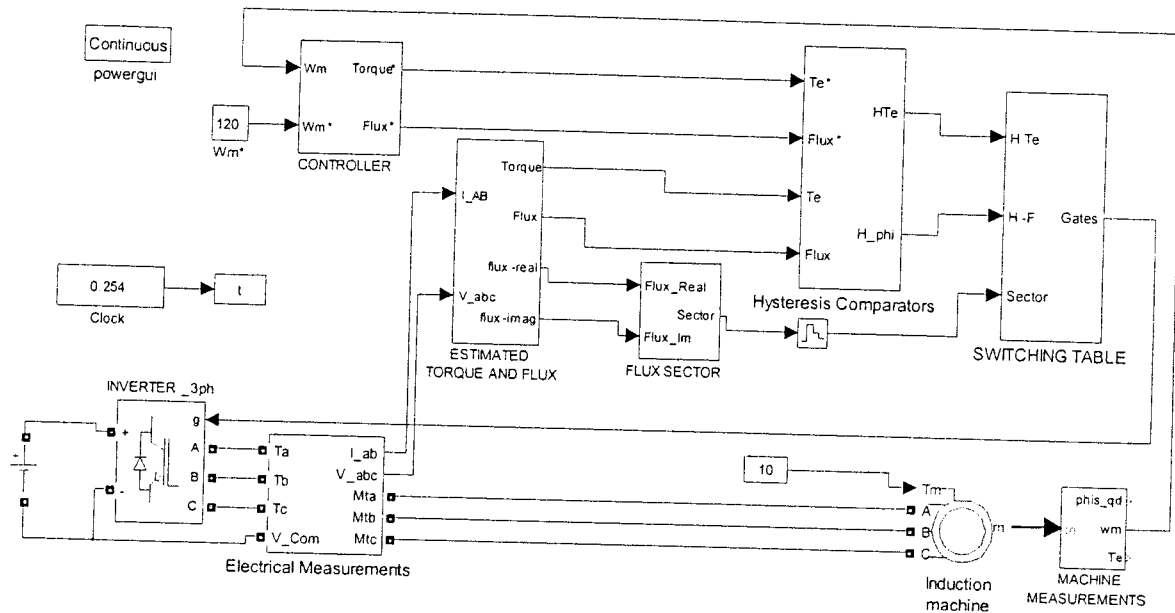
Fig. 3.14: Simulink diagram for DTC scheme implemented with proposed flux linkage sector and hysteresis algorithms

Sample simulation results are shown in Figs 3.15-3.18. These simulations have been carried out while the motor is running at 120 rad/sec and no-load conditions. The parameters of the motor used for simulation are given in Annex-A. Fig.3.15 shows the results for hysteresis model given by mathematical model (3.17.a-c) for a time interval from 0.25 to 0.256 sec in steady state. The ripples are of variable amplitude and max variation in torque is 5.5 Nm (peak to peak). The application of quick forward and backward voltage vectors makes the switching rate high. Almost 36 switching events occur during the selected time intervals. Hence lower torque ripples are achieved at the cost of very high switching frequency of the VSI.

Fig. 3.16 shows the results for 3-level torque hysteresis given by Simulink library DTC model. The maximum peak to peak ripple level is 7Nm and the number of switching events is 33. The system tends to stabilize under the set point torque and margin of stability reduces. Fig.3.17 shows the results for proposed torque hysteresis. Almost every peak is touching the band limits defined by the hysteresis comparator. Max peak to peak ripple level is slightly less than 6Nm. There are least switching events (24) in this case. The system tends to stabilize around the set point torque and hence more stable control. Conclusively, optimization of torque ripples and inverter switching frequency is achieved through the proposed algorithm for the torque hysteresis comparator. Fig.3.18 shows the net adapted bandwidth for proposed hysteresis comparator. The upper and lower curves show the net positive and negative bandwidths, respectively.

Figures 3.19-3.22 show the system responses for motor load of 10Nm (50% rated load) and rotor speed 120rad/s. Fig.3.19 (a & b) shows the comparison of stator flux linkage with conventional 2-level hysteresis and proposed band adapted one. Evidently, the results have improved a lot. The ripple level has been confined to a very small bandwidth without any abrupt peaks. The stator current ripples are proportional to the flux linkage [44]. Therefore, similar better results like flux are achieved for stator currents as well. The comparison is shown in Figures 3.20(a, b). Figures 21(a, b) show the zoom in view of Fig.20. There is slightly lesser current is drawn by the motor under the same loading condition with band adapted hysteresis controllers. This is proportional to the save in energy by the proposed system. The most important property to be observed in DTC scheme is its torque ripple level. Figures 22(a, b) show the comparison of conventional and proposed band adapted hysteresis comparator based DTC schemes. The comparison proves that amount of ripples, both in steady and transient state,

51

have been reduced considerably and by the proper selection of stator voltage vectors, the steady state is achieved a bit earlier as well.
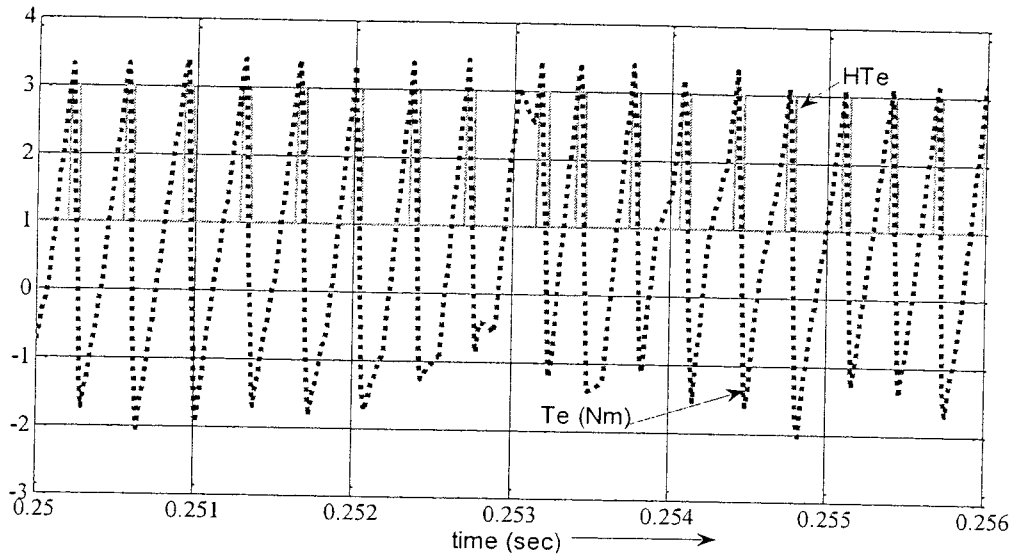
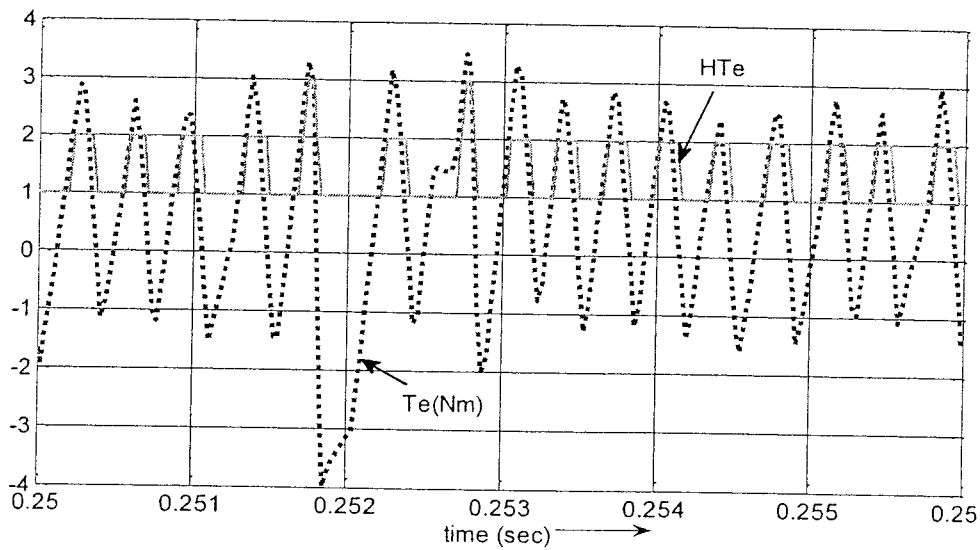Fig. 3.15: Output levels of torque hysteresis controller

Fig. 3.16: Output levels of torque hysteresis controller for the conventional hysteresis model.
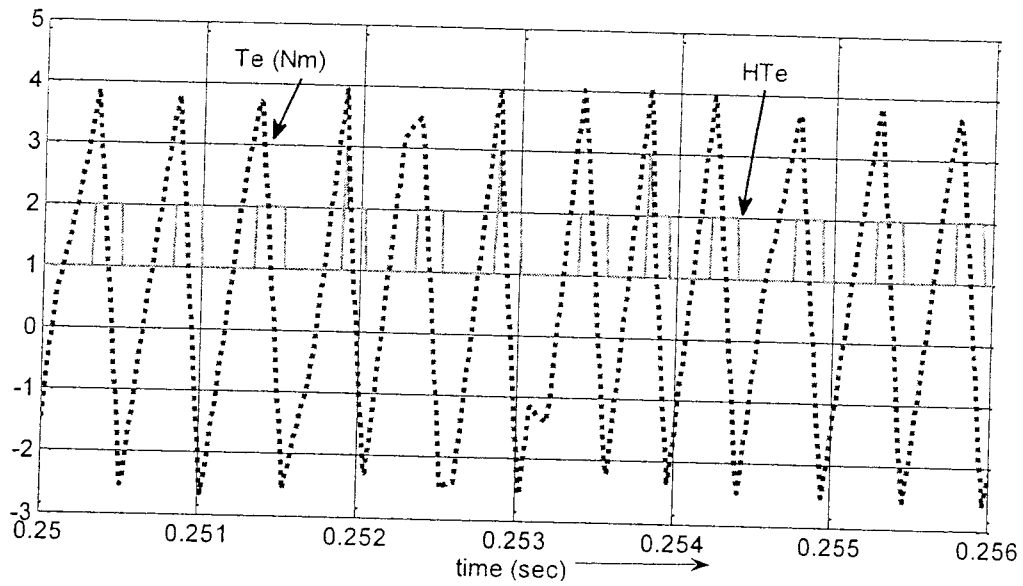
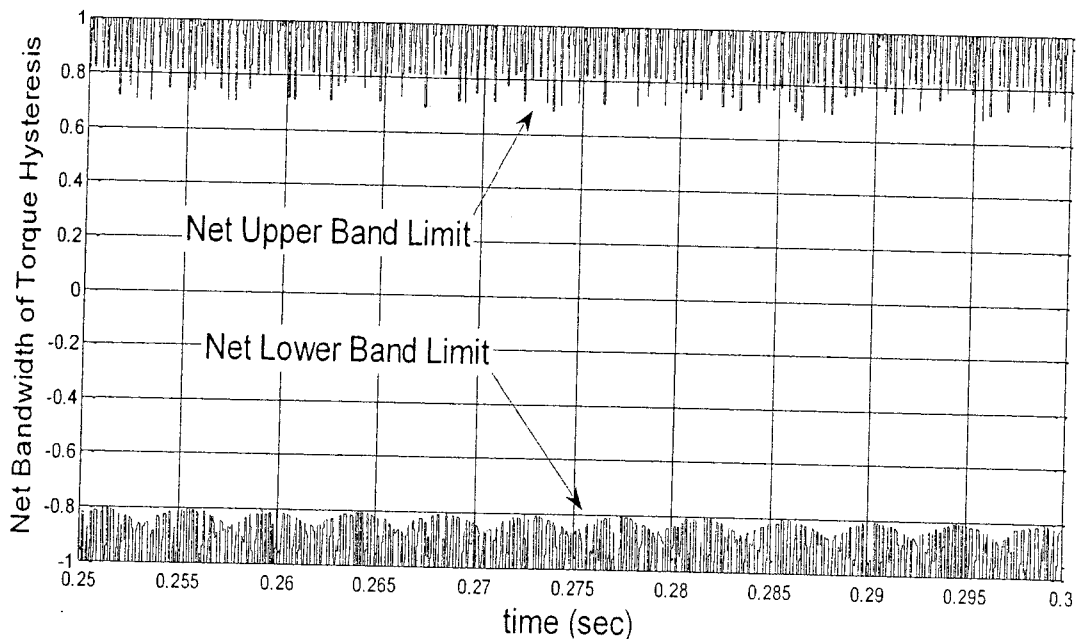Fig. 3.17: Te & HTe by using proposed band adapted hysteresis controller

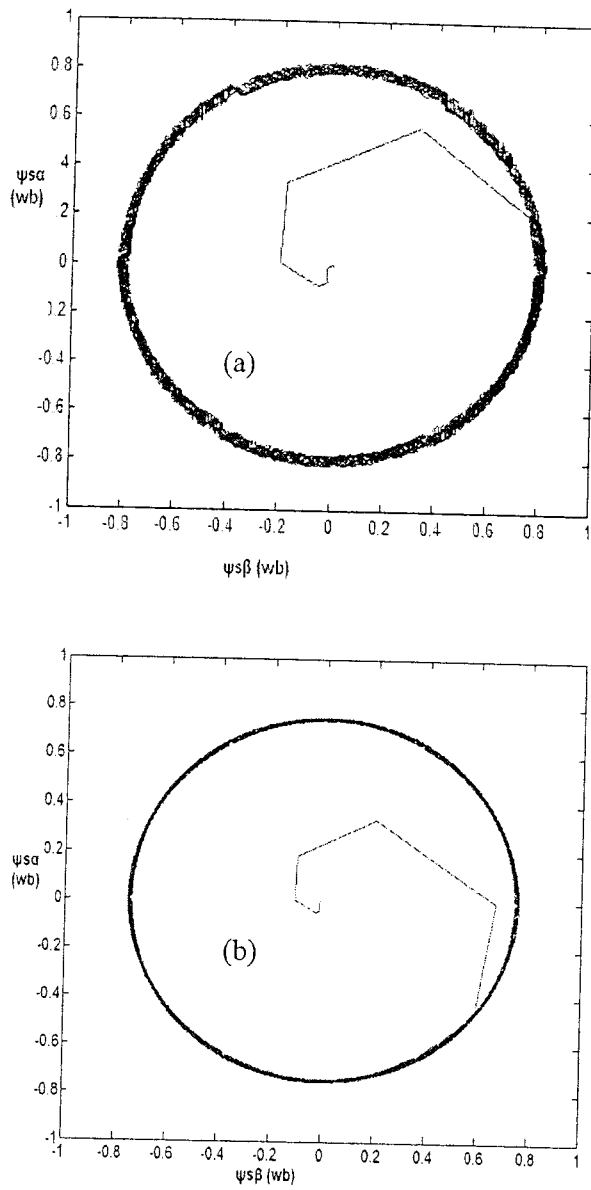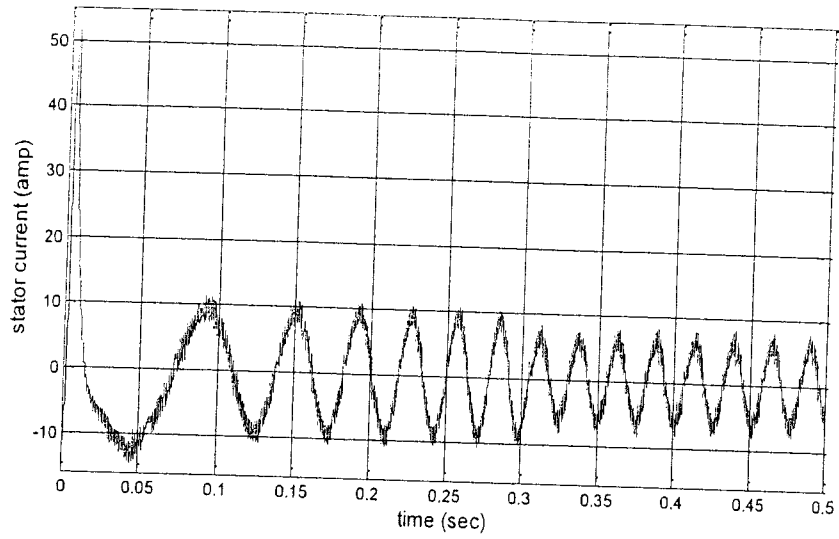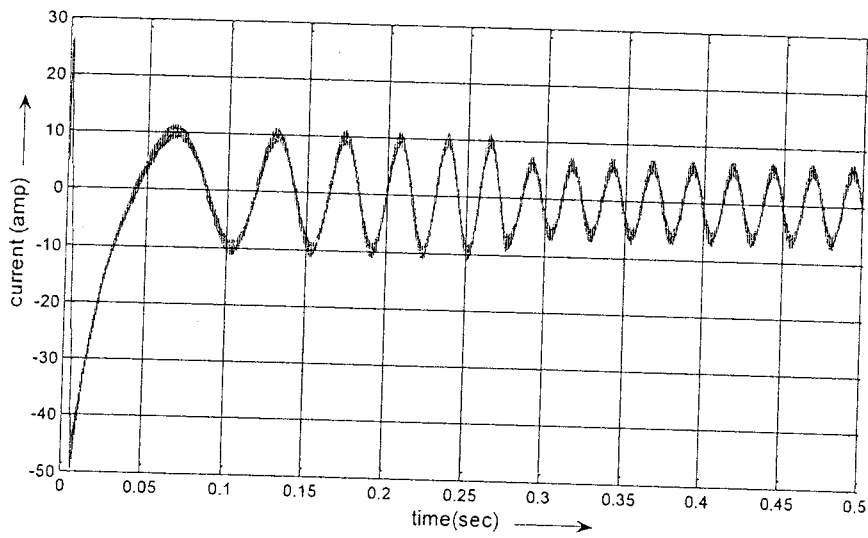Fig. 3.18: Adapted hysteresis band limits, HB_{TU} and HB_{TL}.

Fig. 3.19: Transient and Steady State Stator flux linkage responses of IM drive at 50% rated load (10Nm) and speed of 120 rad/s, (a) conventional DTC, (b) proposed band adapted hysteresis comparators based DTC scheme.

54

(a)

(b)

Fig. 3.20: Transient and steady state stator current responses of IM drive at 50% rated load (10 Nm) and command rotor speed 120 rad/s , with 2-level stator flux linkage hysteresis (a) conventional hysteresis based DTC (b) proposed band adapted hysteresis comparators based DTC scheme.

55
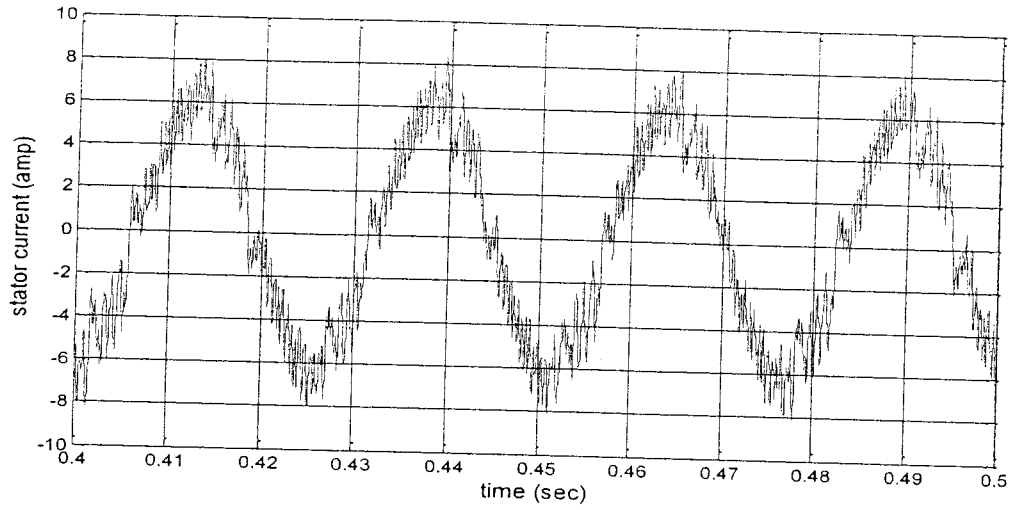
(a)
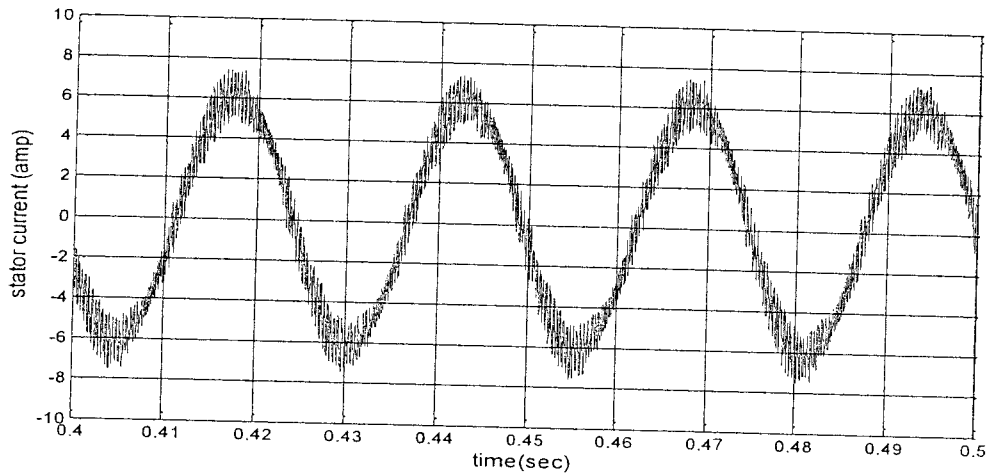
(b)

Fig. 3.21: Zoom-in-view of stator current responses of IM drive at 50% rated load (10 Nm) and speed of 120 rad/s; (a) conventional DTC (b) proposed band adapted hysteresis comparators based DTC scheme.
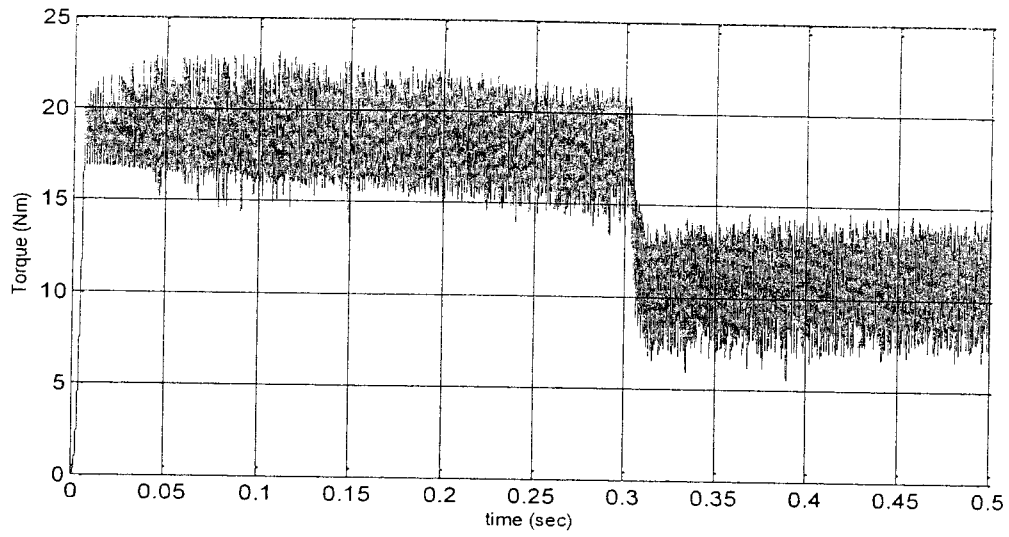
(a)
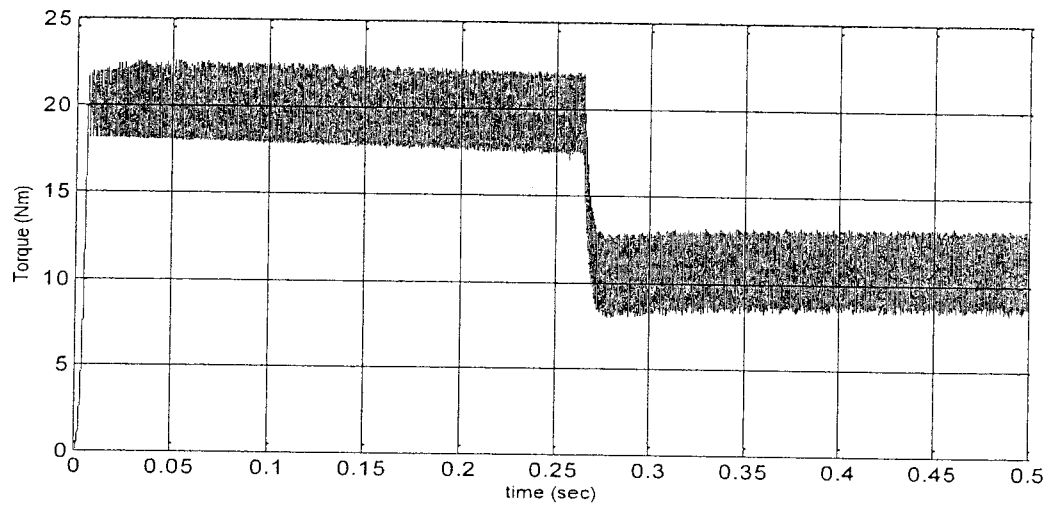
(b)

Fig. 3.22: Transient and steady state torque responses of IM drive at 50% rated load (10 Nm) and speed of 120 rad/s; (a) conventional hysteresis based DTC, (b) proposed band adapted hysteresis comparators based DTC scheme.

57

3.6 Conclusion

The band adaptation models presented in this chapter proved successful in following aspects:

- Motor torque ripples were reduced both in transient as well as in steady state.
- Stator flux and current ripples were reduced significantly.
- Inverter switching rate decreased appreciably and it was almost at constant rate.
- Lesser consumption of energy with proper selection of switching scheme obtained by band adapted hysteresis controller.
- Lesser noise production due to decreased ripples in torque.
- The proposed new algorithm to find the sector of stator flux linkage is simpler but equivalent in functionality to conventional one.

CHAPTER 4

Development of Neuro-Fuzzy Controller for DTC based IM Drive

4.1 Introduction

In classical control systems the accuracy of the control is highly plant mathematical model dependent. Unfortunately, the majority of the models are parameter dependent and are based on many assumptions for simplicity. These assumptions introduce inaccuracy in the model. Conclusively, the approximated model based classical controllers are inaccurate and parameter sensitive. The use of artificial intelligence was industrialized since 1960s [63]. The earlier use was limited to only decision making process for monitoring the industrial process. The major advantage of intelligent controllers is that they need only an approximate mathematical model. The ideal behaviour of artificial intelligent controller (AIC) is capable to learn, recall and generalize from training patterns like human brain [64]. The use of advanced electronics has made it possible to implement complex controllers by using powerful microprocessor. There are mainly three kinds of AICs which include fuzzy, neural networks and their hybrid neuro-fuzzy controller. There also exist some other forms of AI like genetic algorithm(GA) assisted neural networks. But these algorithms are not the function approximators rather they are simple and powerful general purpose stochastic optimization methods.

The pure fuzzy logic controller is based on the expert knowledge. If high performance is wanted, it needs manual adjustments by trial and error. In most FLCs, the response accuracy is

largely dependent on the number of membership functions and the rules used for designing the controller [65, 66]. The expert knowledge is the key for formulating the rules. Any deficiency in the rules directly affects the controller performance. Moreover, larger number of rules and membership functions cause high computational burden, which is the major limitation for their practical industrial applications.

The artificial neural network (ANN) can cope with any system nonlinearities and uncertainties. Optimization of number of hidden layers and their nodes are the main features in the design of such controllers [39]. Generally, a larger ANN requires proportional computation burden and converges slowly. The design of a supervised ANN with error back propagation scheme needs three kinds of data set. The training data algorithm plays extremely important role in the design of neural network and requires a careful selection. Sometimes, it is tough to create a serial of training data for ANN that can handle all the operating modes [67]. The concept of a neuro fuzzy controller (NFC) combines the advantages and eliminates the drawbacks of both standalone FLC and ANN. The NFC utilizes the transparent and linguistic representation of a fuzzy system with the learning ability of artificial neural networks. NFC enables the system to be adaptive and requires minimum human intervention for the tuning.

To the best of the author's knowledge no major work has been reported on the dynamic control of DTC scheme based IM drive by using a self-tuned NFC. Majority of the reported works have improved the performance of DTC scheme by using AI based DTC table or hysteresis comparators [45-48,55]. In these works the target is to minimize torque ripples and not the dynamic characteristic improvement of the drive system. In [57] the author has used a PI-controller for steady state and a FLC for transient state. The switching mechanism is based on the magnitude of the speed error. The threshold limit of the switching mechanism for two

60

controllers is based on the sampling frequency and the type of the FLC used. These factors make the transition of switching very complicated and restrict the application of this hybrid controller only to specific drive under specific conditions. Further the PI-controller is used in steady state which is highly motor parameters and system disturbances dependent. Even complicated FLC, with two input variables, each comprising seven membership functions and 49 rules, has no learning mechanism and is based on trial and error. Therefore, in this thesis, to improve dynamic performance, a Takagi Sugeno Kang (TSK) type self-tuned NFC is developed. This controller is robust to parameter sensitivity and has a learning/training algorithm to adapt with system uncertainties. There is no need to change the controller during the course of running as in the above cited work.. The adaptive-network-based fuzzy inference system (ANFIS) is relatively fast convergent due to neural learning and the ability of fuzzy logic to construct reasonably good input membership functions. It has better tracking performance and better adaptability than the other controllers. An online self tuning algorithm is also developed in order to adjust the consequent part of the controller. Finally, the proposed NFC is integrated with the band adapted hysteresis based DTC scheme in order to achieve both high dynamic performance and optimum torque ripples.

4.2 Development of a Neuro-Fuzzy Controller

4.2.1 Design of a TSK-Type Neuro-Fuzzy Controller

After their successful industrial applications by Hitachi and Yaskawa, AICs are gaining practical popularity in the drive realm [67]. These manufacturers applied pure fuzzy and pure neural network based controllers separately. But the general/universal motor drive must have a tuneable

61

controller. None of the motor manufacturers have prior knowledge of the load it will run. The manually tuned controller is useless without expert knowledge. Since the AICs are the future of drive schemes, therefore, the motor manufacturer must provide a controller which could be tuned without expert knowledge.

This thesis presents a simple online self-tuned NFC based DTC scheme for IM drive. The nonlinear mapping from input (normalized speed error) to the output (motor developed torque) is done by using a TSK-type NFC. The general structure of a TSK-type NFC with two inputs, for the control of electrical motors is shown in Fig.4.1 [67, 68]. Each linguistic variable consists of three exponential membership functions i.e. one Gaussian, for zero membership function and two sigmoidal membership functions, one for positive and other for negative membership function as shown in Fig.4.2. This combination naturally produces nine rules for the neuro fuzzy controller as shown in Fig.4.1. The excellence of exponential function is that it changes slowly as it approaches to its extreme saturation values and its slope is almost constant and maximum in the middle portion. Generally, this is one of the speed controller desired property. But this property has to be paid back in the main two costs for the controller. Primarily, the value of exponential function is calculated by using some computer algorithms based on approximation of some infinite series like Taylor Series. Secondly, the exponential function value is non-zero for the whole operating range of the controller input variables. It means that all the rules are non-zero all the time irrespective their values are of no significance for the controller. Both the factors introduce a high volume of calculation burden on the processor [69]. This may cause the processor for real time implementation to over run. Consequently, to run the controller smoothly it may need to increase the sampling time which ruin the whole advantage of the exponential function.
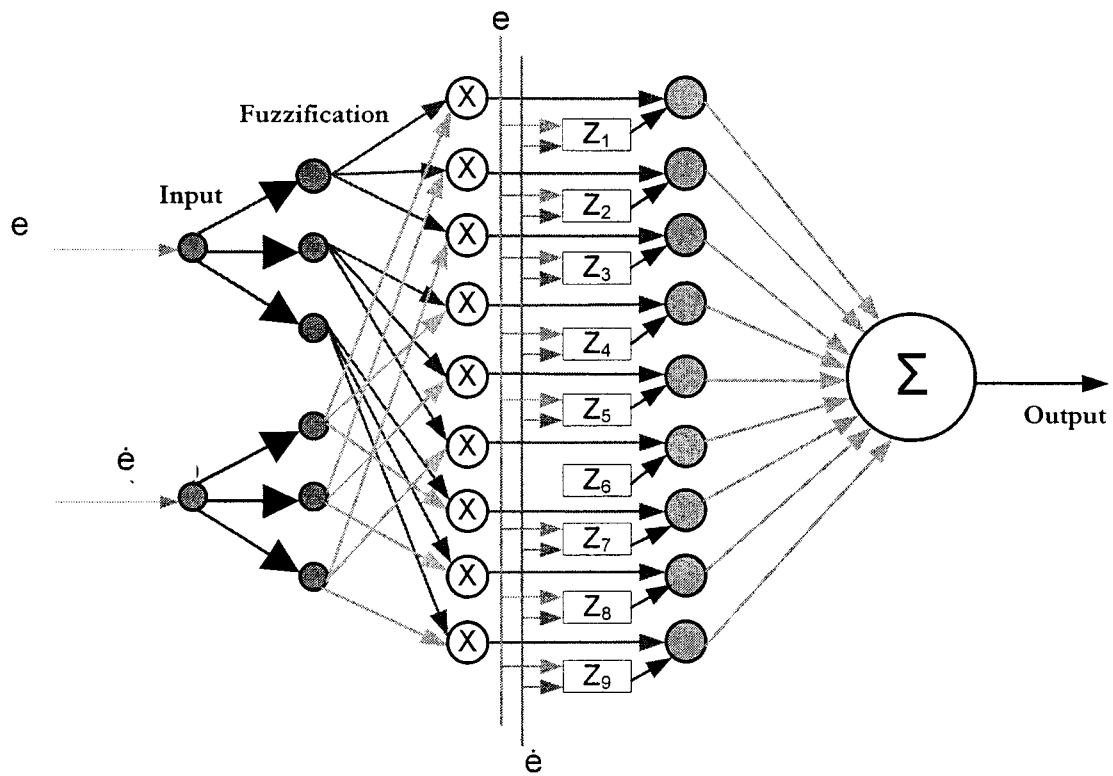
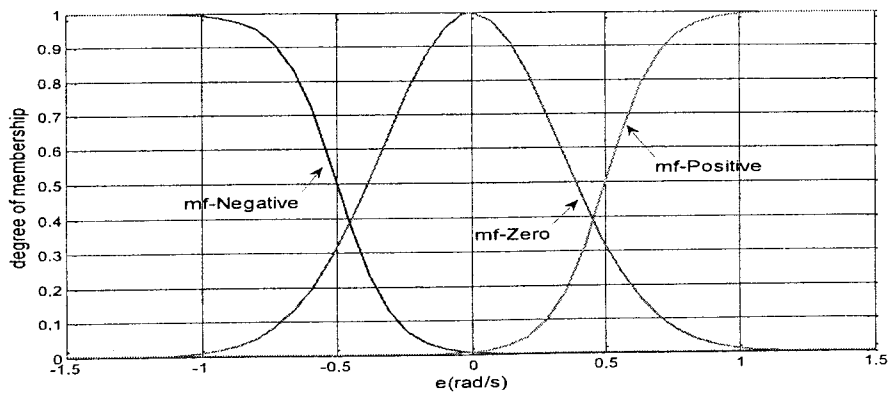Fig. 4.1: General Structure of conventional TSK-Type NFC.

Fig. 4.2: Commonly used membership functions

In the controller shown in Fig.4.1, the first layer is the input layer. This layer just passes the scaled controller input to the next layer. The second layer is the fuzzification layer. Each input is fuzzified by using some suitable membership functions (mfs) like sigmoid, triangular and bell shaped etc. These are not the revealed membership functions and may be customized according to requirement. The number of membership function used may vary based on the system requirement. The third and fourth layers are the rule layers. The common fuzzy if---then rules may be replaced by product, minimum or some different technique. Each technique has its own relevant advantages and drawbacks. In order to quickly converge the system error the parameters of the 4th layer are modified by using a tuning block.

4.2.2 Detailed Design of Proposed TSK-Type NFC

The function of each layer of the proposed NFC is briefly described as follows:

Layer I: In the first layer normalized speed error and the motor acceleration i.e. rate of change of actual speed are calculated. The output of first layer or input to the second layers is given as:

$$e = O_1^I = \frac{\omega_m^* - \omega_m}{\omega_m^*}$$

(4.1)

$$\dot{e} = O_2^I = \omega_m[n] - \omega_m[n-1]$$

(4.2)

The letter 'O' stands for the output of the layer and its subscript and superscript for member function number and layer number, respectively. ω_m^* is the command speed, $\omega_m[n]$ and $\omega_m[n-1]$ present the present and previous sample of the actual speed.

64

Layer II: This is the fuzzification layer. Each crisp input value is fuzzified by using its membership functions. In the proposed controller strategically two membership functions are selected for both the inputs as shown in Fig. 4.3(a, b). In these figures their equivalent exponential functions are also shown by dotted lines. It is clear from the figure that the line segments of proposed membership functions almost approaches to their equivalent exponential functions. All the membership functions involve only calculation for linear function i.e. a straight line equation. This linear characteristic of the mfs avoids the extra computational burden as already discussed in section 4.2.1. These membership functions do almost the same job as their equivalent exponential functions.
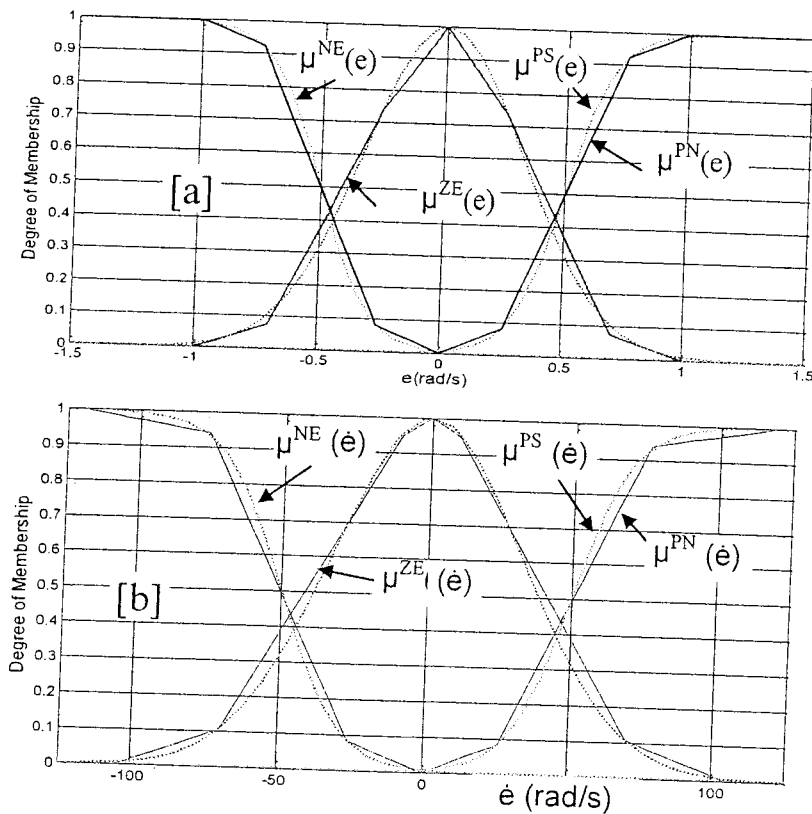
Fig. 4.3(a, b): Membership functions for linguistic input variables 'e' & 'ė'.

65

Keenly, observing Fig.4.3 (a, b) it is clear that the mfs $\mu^{ZE}(e)$ and $\mu^{ZE}(\dot{e})$, both are symmetric about origin. Also, the mfs $\mu^{PS}(e)$ and $\mu^{NE}(e)$ are mirror image of each other. Similar is the case with linguistic variable 'ė' mfs. By choosing the absolute crisp values of the variables 'e' and 'ė' make the case simpler and reduce the mfs for each variable to two instead of three. The node equations for membership function in layer II is given as,

$$O_1^{II} = \mu^{PN}(e) = \begin{cases} 0.32\,|e| & 0 \le |e| \le 0.26 \\ 1.72\,|e| - 0.364 & 0.26 < |e| \le 0.75 \\ 0.3\,|e| + 0.7 & 0.75 < |e| \le 1 \\ 1 & |e| > 1 \end{cases} \tag{4.3}$$

$$O_2^{II} = \mu^{ZE}(e) = \begin{cases} 1 - \frac{27}{26}\,|e| & 0 \le |e| \le 0.26 \\ 1.12 - 1.49\,|e| & 0.26 < |e| \le 0.7 \\ 0.25(1 - |e|) & 0.7 < |e| \le 1 \\ 0 & |e| > 1 \end{cases} \tag{4.4}$$

$$O_3^{II} = \mu^{PN}(d\dot{e}) = \begin{cases} 3.07 * 10^{-3}\,|e| & 0 \le |\dot{e}| \le 26 \\ 0.017\,|e| - 0.366 & 26 < |\dot{e}| \le 76 \\ 1.37 * 10^{-3}\,|e| - 1043 & 76 < |\dot{e}| \le 120 \\ 1 & |\dot{e}| > 120 \end{cases} \tag{4.5}$$

$$O_4^{II} = \mu^{ZE}(\dot{e}) = \begin{cases} 1 - 0.005\,|e| & 0 \le |\dot{e}| \le 10 \\ 0.81 - 0.014\,|e| & 10 < |\dot{e}| \le 70 \\ 0.315 - 0.003\,|e|) & 70 < |\dot{e}| \le 105 \\ 0 & |\dot{e}| > 105 \end{cases} \tag{4.6}$$

Layer III: This is the first step of fuzzy rule evaluation. The rule may be evaluated by any of appropriate method like minimum, product or height etc. In the proposed NFC the product method is chosen to implement the 'AND' logic. The output of each node in this layer gives the firing strength of corresponding rule. Since there are two inputs with each having two membership functions, therefore, four nodes are assigned in this layer covering all possible cases. Hence in the proposed NFC the maximum active rules at any time reduce to four instead of nine as in the conventional NFC. The node equation in layer- III can be specified as,

$$O_i^{III} = w_i = \prod_{j=1,2}^{k=3,4}(O_j^{II} * O_k^{II})$$

(4.7)

O_i^{III} denotes the output for i^{th} node in layer III, O_j^{II} and O_k^{II} are components of fuzzy numbers from 'e' and 'ė', respectively, which denote inputs for i^{th} node in layer III.

Layer IV: The normalized firing strength of each rule is determined in this layer. This is the 2nd and final step of fuzzy rule evaluation. The node equation in this layer can be specified as,

$$O_i^{IV} = \overline{w_i} = \frac{w_i}{\sum w_i}$$

(4.8)

Where $\overline{w_i}$ is the normalized firing strength of ith rule.

Layer V: The parameters in this layer are called the consequent parameters. The crisp values of the variable are used in this step instead of their fuzzified values. This is the preference of Sugeno type NFC over Mamdani which uses fuzzified values of the variable and need dufuzzification at the end [67]. Hence, the computational burden in Sugeno type NFC is lesser than its competitive Mamdani type NFC. The output of each node in this layer can be specified as:

$$O_i^{V} = Z_i^{IV} * O_i^{IV}$$

(4.9)

Z_i^{IV} is the adaptive weight factor for the ith node. It is a function of crisp values of variables 'e' and 'ė'.

Layer VI:. This is the last step for the calculation of output of the controller. The out of this layer may be specified as:

$$O^{VI} = \Sigma(O_i^{III} * O_i^V) / \Sigma O_i^{III} \tag{4.10}$$

This is the final output of the controller. Plug in (4.9) into (4.10) the command torque may be rewritten as:

$$T_c = O^{VI} = \Sigma(O_i^{III} * Z_i^{IV} * O_i^{IV}) / \Sigma O_i^{III} \tag{4.11}$$

This is the command torque of DTC scheme for IM drive. This torque forces the motor to follow the command speed. The schematic diagram for the proposed TSK-type NFC and its Simulink model are shown in Fig.4.4 & Fig.4.5 respectively.
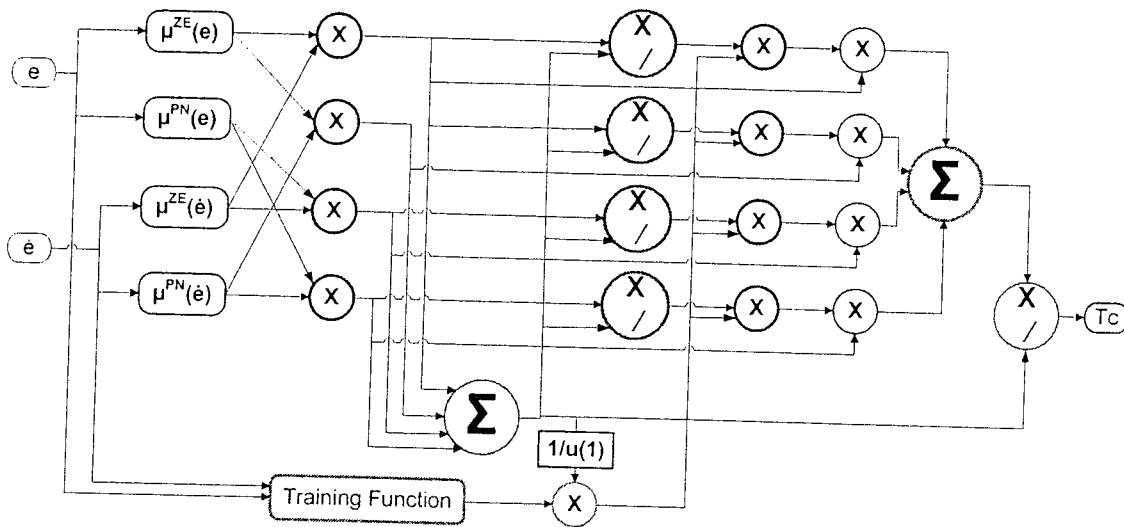
Fig. 4.4: Structure of proposed TSK-type NFC

68
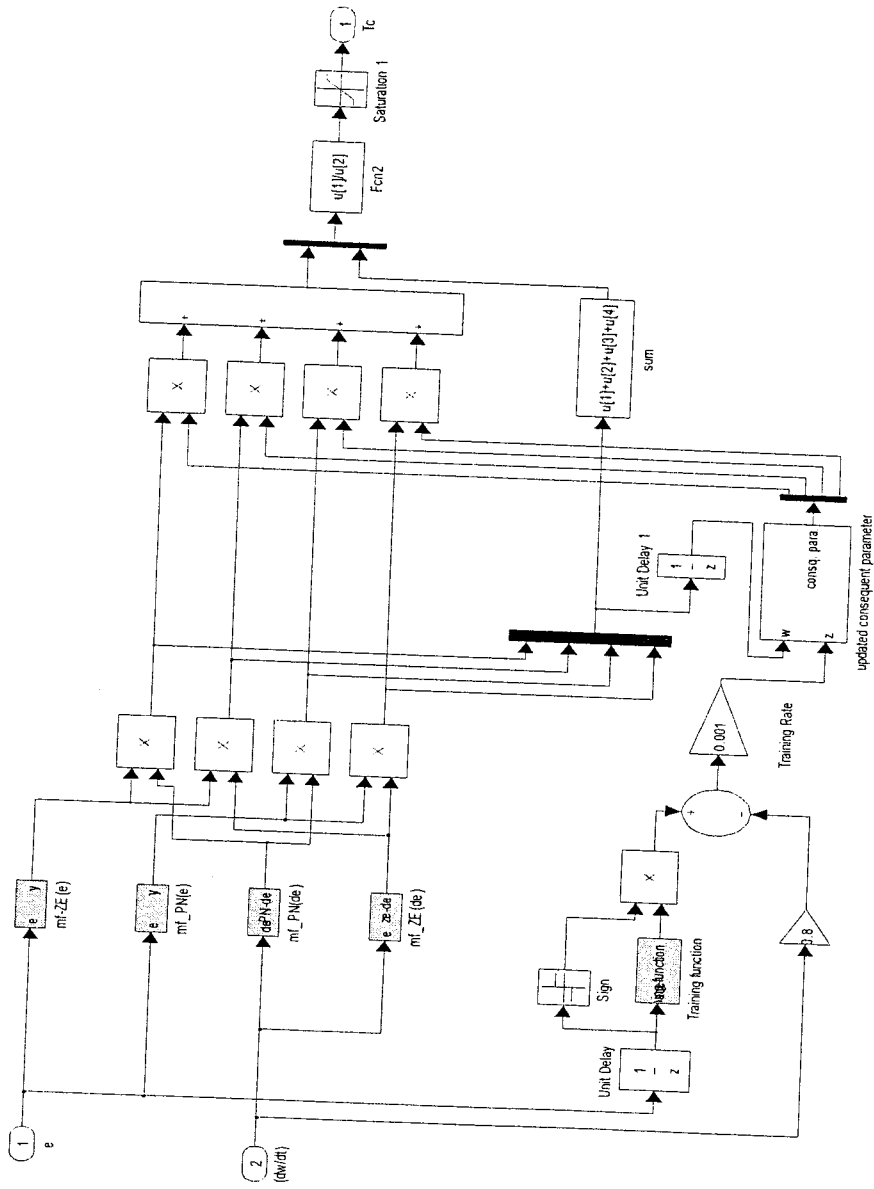
Fig. 4.5. Simulink/Matlab model of the proposed NFC

69

4.2.3 Tuning Algorithm for the Proposed Controller

Under varying dynamic conditions of the IM drive it is almost impossible to determine the NFC desired output, T_c. Ideally, it requires a unique operating curve for the motor under each dynamic condition even for the same speed error. Obviously, under different operating conditions, it requires a kind of on-line self-tuning method for the controller to work properly. The tuning algorithm for the consequent parameters Z_i^{IV} can be developed using a reinforcement signal, 'r' which is based on the difference between the reference $(d\omega_m/dt)^*$ and actual $(d\omega_m/dt)$ IM acceleration models. The reference acceleration model is designed on the basis of specific requirement of IM. The reinforcement signal is utilized to generate control action to produce the desired speed response. The reference acceleration model designed $(d\omega/dt)^*$ is shown in Fig.4.5. The mathematical model is given below:

$$y = \left(dw_m/dt\right)^* = \begin{cases} (0.99\,|e|)K_1\,sign(e) & 0 \le |e| \le 0.02 \\ (2.854\,|e| - 0.0373)K_1\,sign(e) & 0.02 < |e| \le 0.04 \\ (3.3\,|e| - 0.055)K_1\,sign(e) & 0.04 < |e| \le 0.32 \\ K_1\,sign(e) & |e| > 0.32 \end{cases} \quad (4.12)$$

K1=12000, is a gain and operation 'sign' yields the sign e.g. positive or negative, of the error signal 'e'. The error between reference and actual acceleration of the IM for the controller may be defined as:

$$E = \frac{1}{2}r^2 = \frac{1}{2}(y - 0_2^l)^2 \quad (4.13)$$

The consequent parameters, Z_i^{IV} in the fifth layer is updated by the controller in each sampling time to converge this acceleration error to zero. Since the IM acceleration is proportional to the developed torque or vice versa. Therefore, it may be summarized as:

$$O_2^I = K_2 \ T_c = K_2 \ O^{VI}$$

(4.14)

Where, K2 is proportionality constant. Combining (3.11) and (3.12) the updated laws may be expressed as:

$$Z_i^{IV}(n) = Z_i^{IV}(n-1) - \acute{\eta}\frac{\partial E}{\partial Z_i^V} = Z_i^{IV}(n-1) - \acute{\eta}\frac{\partial E}{\partial O_2^I}\frac{\partial O_2^I}{\partial Z_i^V}$$

(4.15)

Using (3.11), (3.14) and (3.15), the self-learning algorithm may be redefined as,

$$Z_i^{IV}(n) = Z_i^{IV}(n-1) + \eta(y - {^{dw_m}\!/\!_{dt}})\frac{O_i^{III}}{\sum O_j^{III}}$$

(4.16)

Where $\eta = k\eta' = 0.001$, is the learning rate.

The value of η may be obtained by trial and error method or a self-tuning method. For the proposed controller, the value of η is obtained by trial and error method. Smaller values of training rate η results in small acceleration and takes a very long time to reach the reference speed even sometimes the controller may never be able to get the desired targeted speed. Larger η converges the acceleration error quickly but at the cost of big torque and current ripples just before and during the steady state. This results in speed ripples causing motor vibration. The complete IM drive with the proposed Neuro-Fuzzy Controller is shown in Fig.4.7.

71
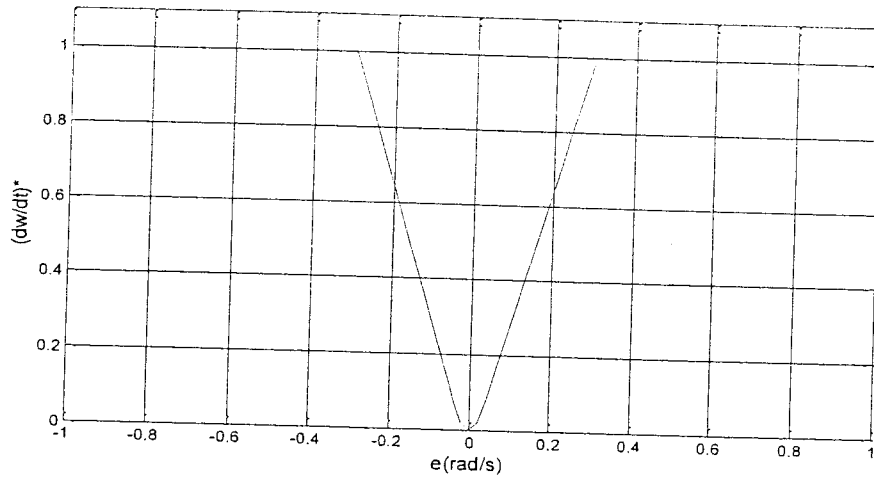
Fig. 4.6: Reference acceleration $(d\omega/dt)^*$ for tuning algorithm.
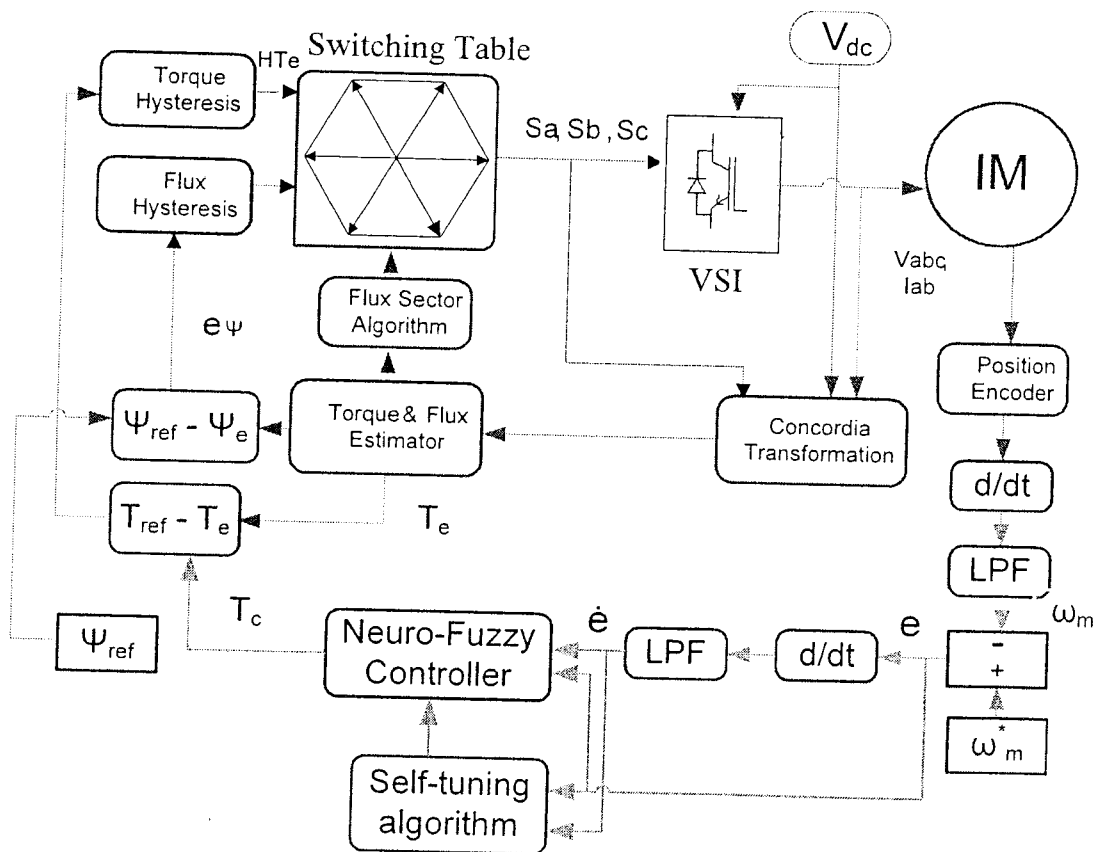
Fig. 4.7: Block diagram of the proposed NFC based IM drive

72

4.3 Simulation Results

The effectiveness of the proposed NFC based IM drive is investigated thoroughly by simulation. The simulation model was developed by using Matlab/Simulink software [62]. The Simulink model is shown in Fig.3.14. The only difference is that the PI-controller has been replaced by TSK-type NFC. The NFC Simulink model is shown in Fig.4.5. The parameters of the motor used for simulation are listed in Appendix-A. The detailed Simulink subsystems of the NFC are attached in Appendix-B. From here to onward to avoid the repetition of phrase "NFC based band adapted DTC scheme" will be replaced by "proposed DTC scheme". Similarly, instead of "PI-controller and conventional hysteresis comparators based DTC scheme" the phrase "conventional DTC scheme" will be used for simplicity. In order to test the effectiveness of the proposed NFC and variable band hysteresis controllers based DTC scheme for IM drive numerous simulations have been carried out. The performance of the proposed DTC scheme is also compared with the conventional DTC scheme to prove its superiority. Sample simulation results are presented below.

Figures 4.8 to Fig. 4.11 show the various simulation results of the IM drive at no load and command rated speed of 180 rad/s. Fig. 4.8 shows the simulated speed responses, including the zoom in view, using the conventional DTC scheme and the proposed DTC schemes. It is evident that both the overshot and settling time has been reduced considerably by the proposed DTC scheme.   Fig.4.9 presents the torque responses of the conventional and proposed DTC schemes. The torque ripples have been reduced significantly in the proposed scheme in steady-state. From the zoom-in-view it can be seen that in steady-state the peak to peak (p-p) torque

73

ripple for conventional scheme is approximately 6.5Nm while in the proposed scheme it is only 2.75Nm, which clearly proves the superiority of the proposed DTC scheme over the conventional one. Fig.4.10 shows the phase-a stator current of the conventional and proposed IM drives. The proposed scheme has improved both the transient and steady state currents. The peak to peak values have been reduced from 18A to 17A and 4.5A to 4.2A for the proposed scheme in transient and steady-states, respectively. Furthermore, by the use of the proposed DTC scheme, the peak-to-peak steady-state current ripple has been reduced from 2.5A to 1.8A. Fig.4.11 shows the stator flux linkage responses both conventional and proposed DTC schemes. It is found that the proposed NFC and variable band hysteresis controllers based DTC scheme exhibits smoother response and lesser ripples in flux as compared to the conventional DTC scheme.
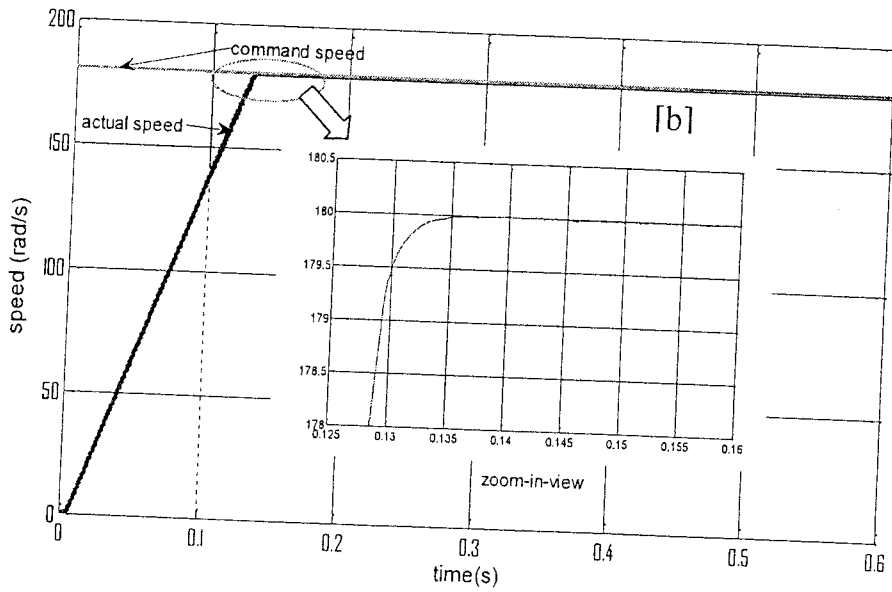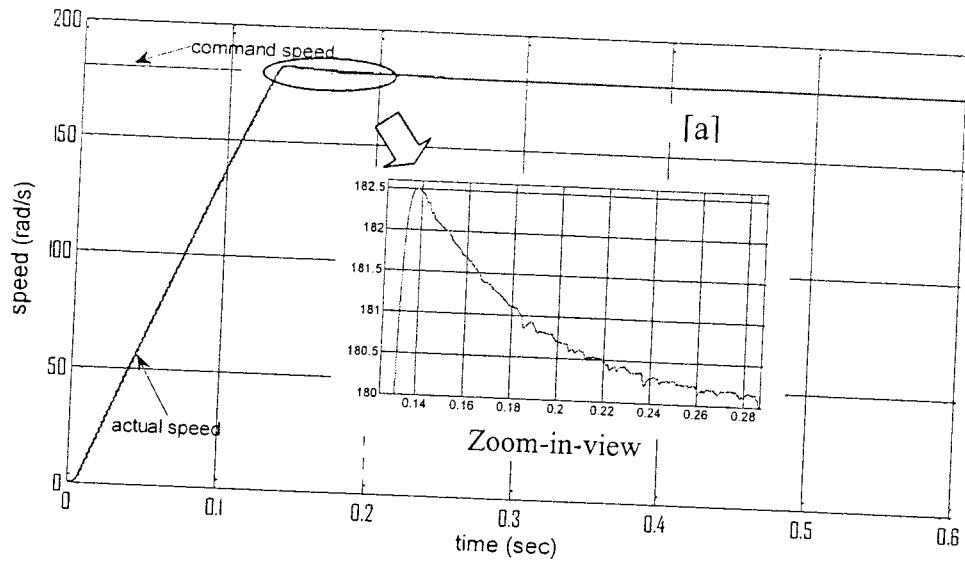
Fig. 4.8: Speed response of the IM drive (with zoom-in-view of the encircled part of response) at no-load and rated speed of 180 rad/s; (a) conventional DTC, (b) proposed NFC and variable hysteresis controller based DTC scheme.
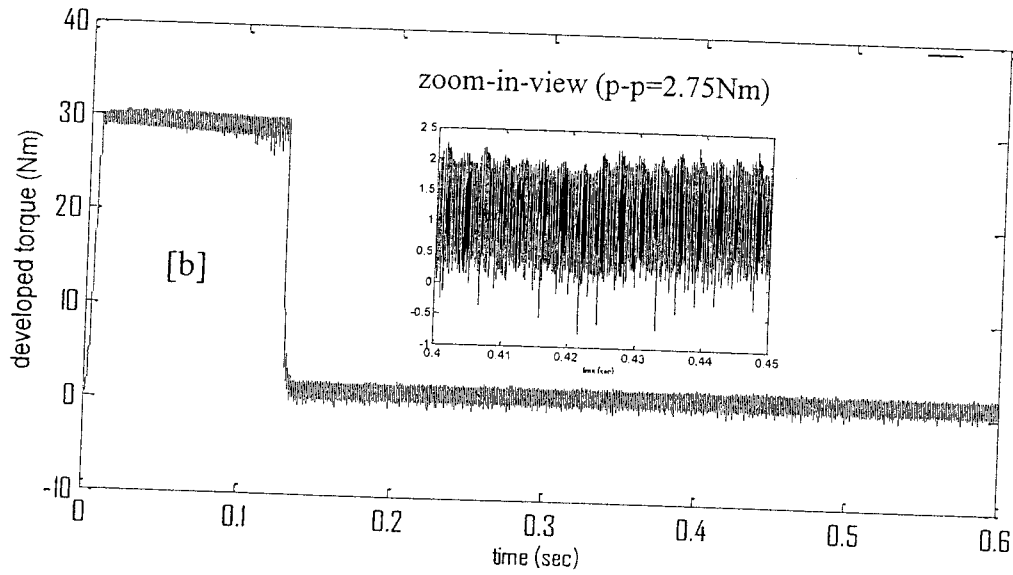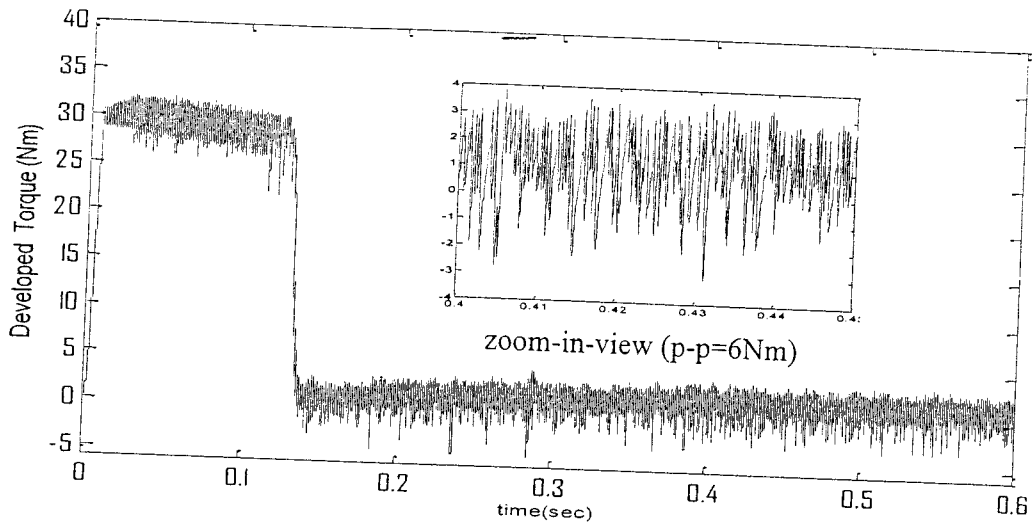
Fig. 4.9: Torque response of the IM drive (with zoom-in-view for the interval 0.4-0.45sec, clearly showing peak to peak (p-p) values) at no-load and rated speed of 180 rad/s (a) conventional DTC, (b) proposed NFC and variable hysteresis controller based DTC scheme.
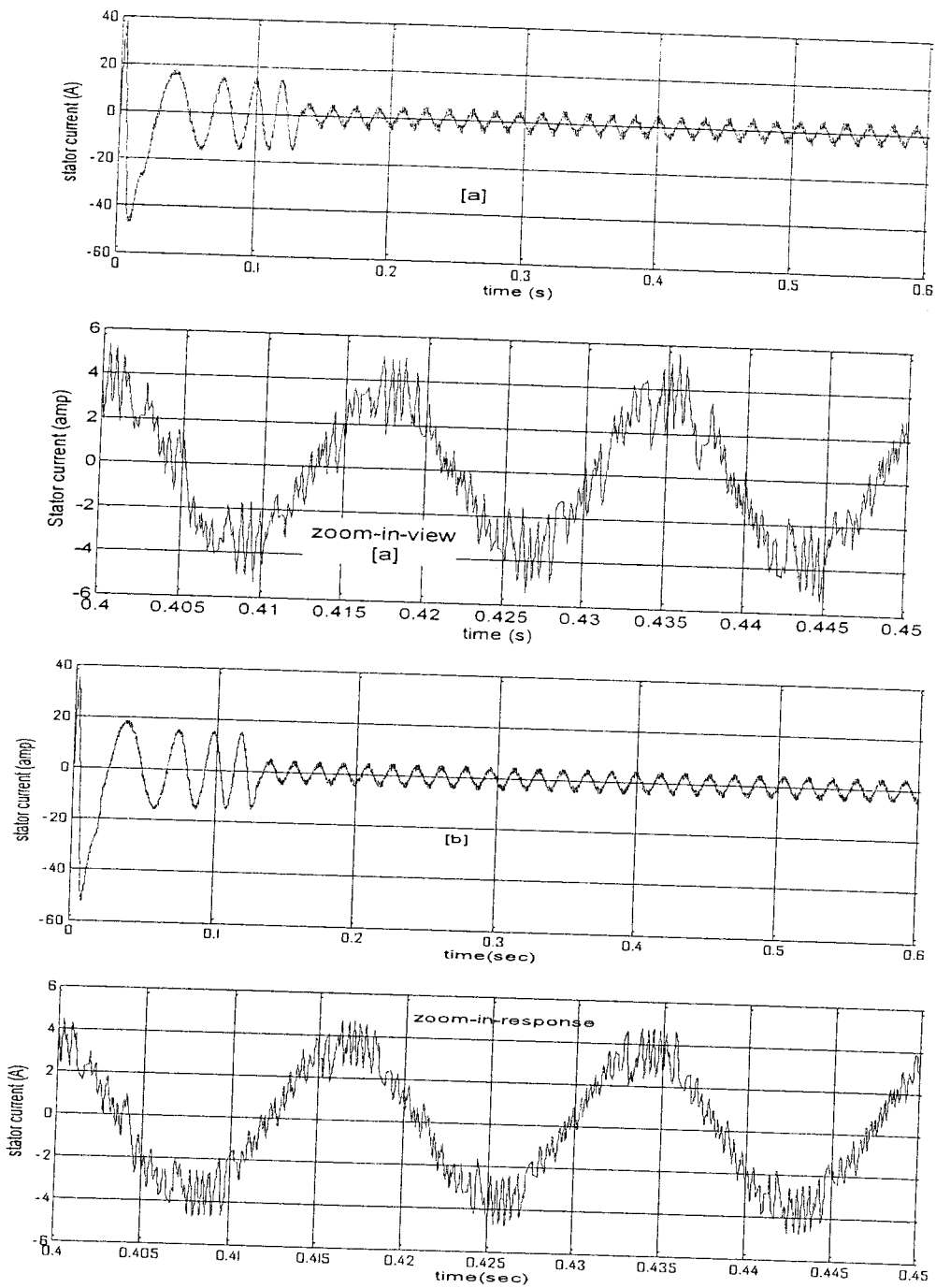
Fig. 4.10: Stator current response of the IM drive (with zoom-in-view for the interval 0.4-0.45sec) at no-load and rated speed of 180 rad/s; (a) conventional DTC, (b) proposed NFC and variable hysteresis controller based DTC scheme.
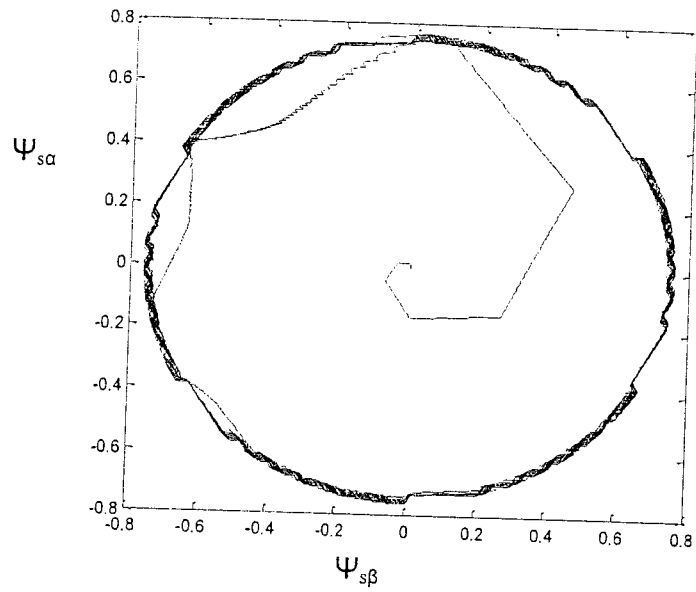
(a)
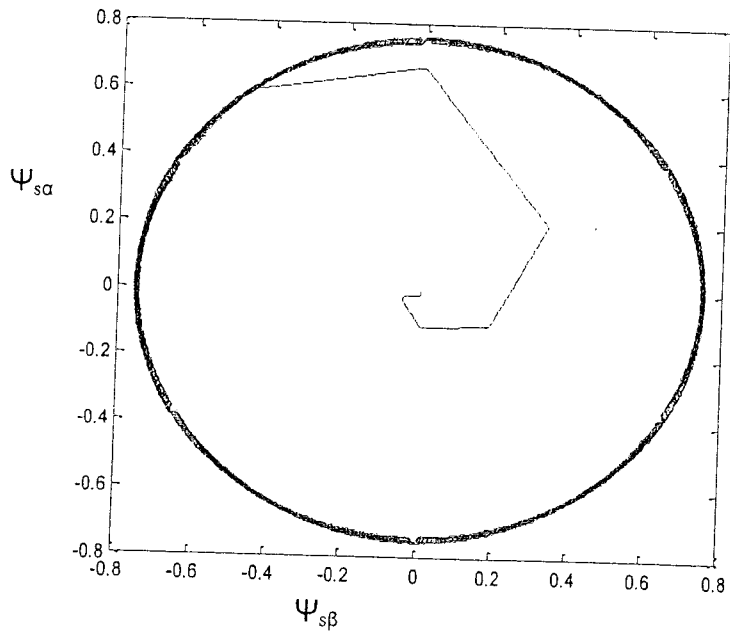
(b)

Fig.4.11: Stator flux linkage of the IM drive, at no-load and rated speed of 180 rad/s; (a) conventional DTC, (b) proposed NFC and variable hysteresis controller based DTC scheme.

78

Figures 4.12 to Fig. 4.14 show the different simulation responses for a step change in command speed from 120 to 150 rad/s while the motor is running at 50% rated load (10 Nm). The abrupt change in speed is applied at the instant 0.3 seconds. Fig.4.12 shows the speed responses using the conventional and the proposed DTC schemes. The proposed scheme is quite superior to the conventional one in respect of settling time. Moreover, it has smoother response with lesser speed ripples. Fig.4.13 presents the corresponding torque responses of the two DTC schemes. It can be compared that in steady state the torque ripples in conventional scheme are approximately 6Nm while in the proposed scheme they are only 2.5 Nm. This comparison proves the superiority of the proposed DTC scheme over the conventional one. Fig.4.14 shows the phase-a stator current of the conventional and proposed IM drive, respectively. The proposed scheme has improved both the transient and steady state currents. The peak value of current in new scheme is lesser than the conventional one proving its better efficiency. Additionally, by the use of the proposed DTC scheme the maximum steady state current ripples have reduced considerably.

Figures 4.15-4.17 show the responses of the IM drive for a step change in load from 10Nm-15Nm at command rated speed of 180 rad/s. The change in load is applied at instant 0.3 seconds. Fig.4.15. shows the simulated speed response, followed by the zoom in view for interval 0.28sec to 0.30sec, using the conventional and the proposed DTC schemes. The zoom in view of the each speed response clearly shows that both the dips in speed and settling time have reduced considerably by the use of the proposed scheme. Fig.4.16 shows the corresponding torque response for the conventional and the proposed DTC schemes for a step change in load at 0.3sec. The torque ripples have significantly reduced in proposed scheme both in transient and

79

steady states. Especially, the negative torque ripples are very big in conventional DTC scheme. Moreover, the transition for change in load is very smooth in the proposed scheme as compared to the conventional one. Fig.4.17 shows the phase-a stator current of the conventional and proposed DTC based IM drives. It is clearly seen that the improvement in current ripple level and peak current values have been achieved by the use of proposed DTC scheme.

The speed and torque responses of the IM drive at rated load and rated speed conditions are shown in Figures .4.18 & 4.19 for both conventional and proposed DTC schemes. Fig.4.18 shows the simulated speed response, followed by the zoom. The zoom in view of the speed response clearly shows that both the dips in speed and settling time have reduced considerably by the use of the proposed scheme. The undershot in speed for proposed DTC scheme is very small as compared to the response produced by the conventional DTC scheme. Fig. 4.19 presents the torque responses of the conventional and proposed DTC schemes, respectively. The torque ripples have substantially reduced in proposed scheme both in transient and steady states.
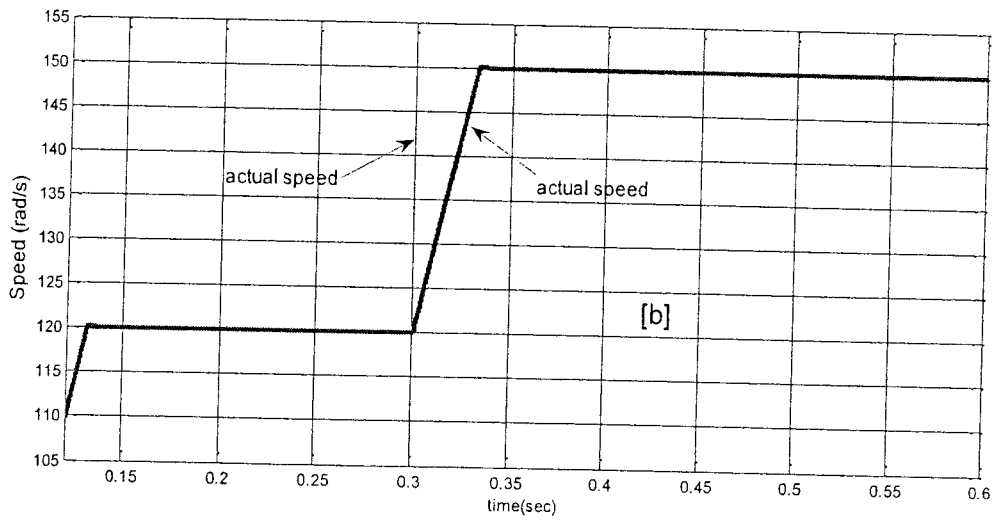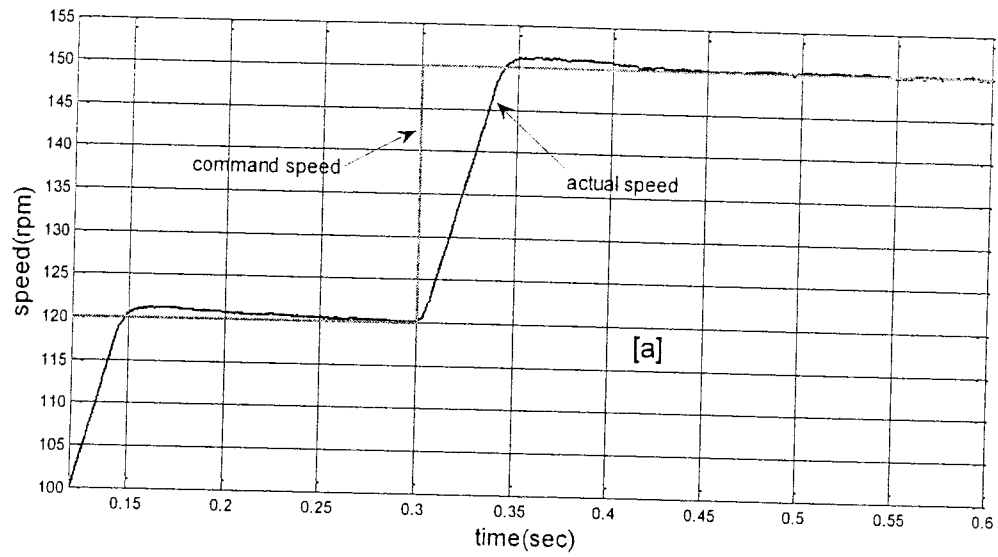
Fig. 4.12: Speed responses of the IM drive for a step change in command speed from 120-150 rad/s at 50% of rated load, (a) conventional DTC, (b) proposed NFC and variable hysteresis controller based DTC scheme.
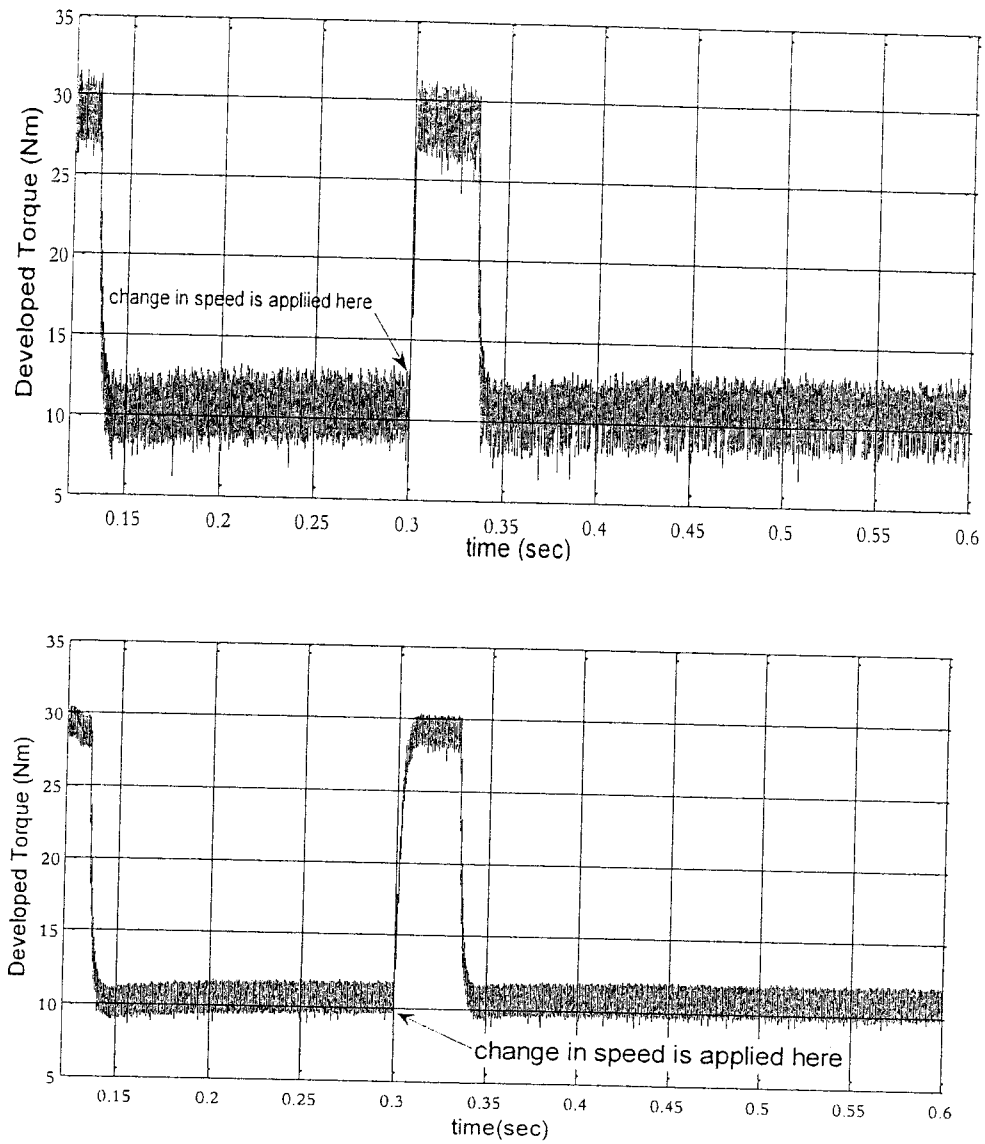
Fig. 4.13: Developed Torque of the IM drive at 50% of rated load. The step change in speed from 120-150 rad/s is applied at 0.3 sec., (a) conventional DTC, (b) proposed NFC and variable hysteresis controller based DTC scheme.
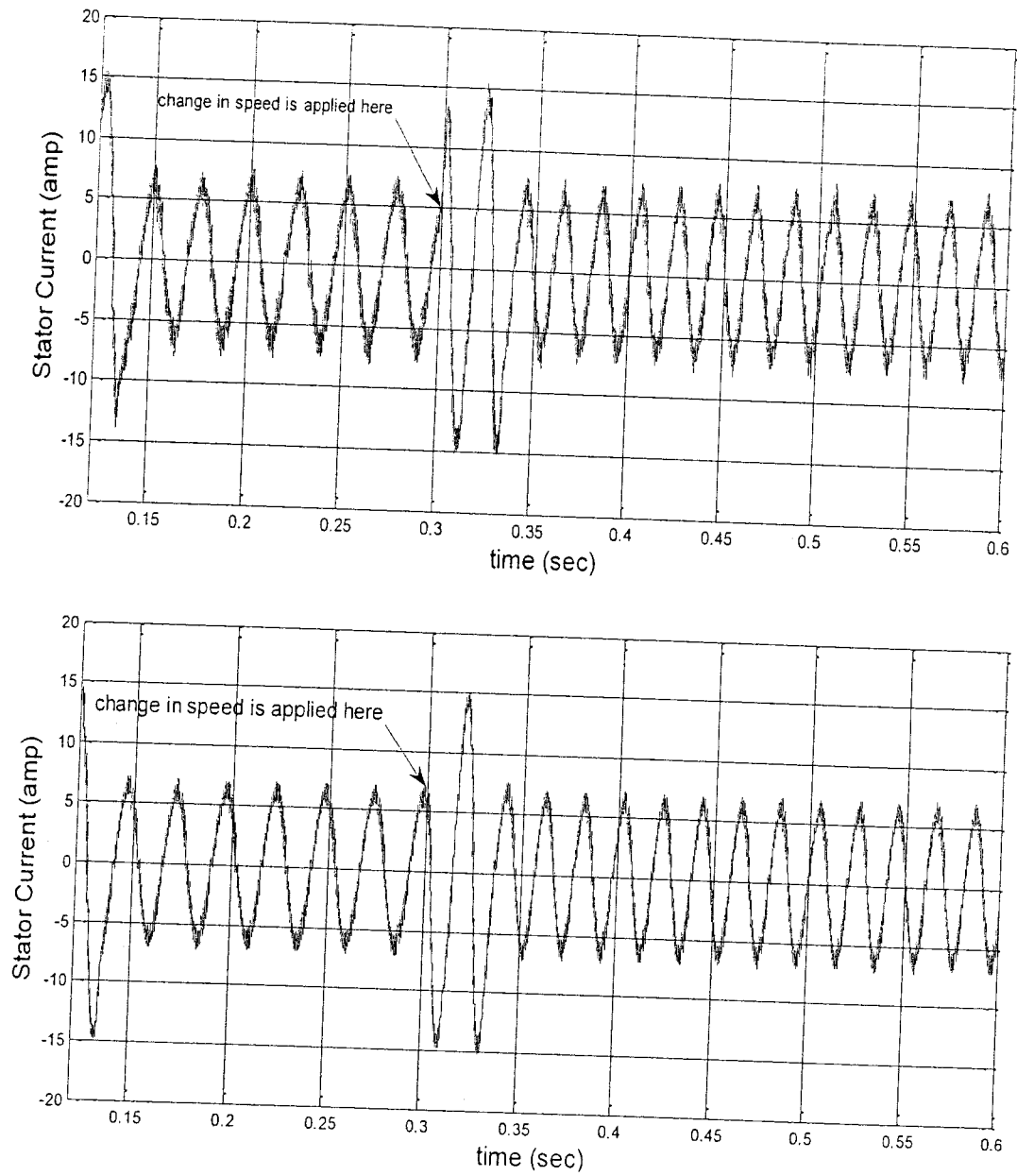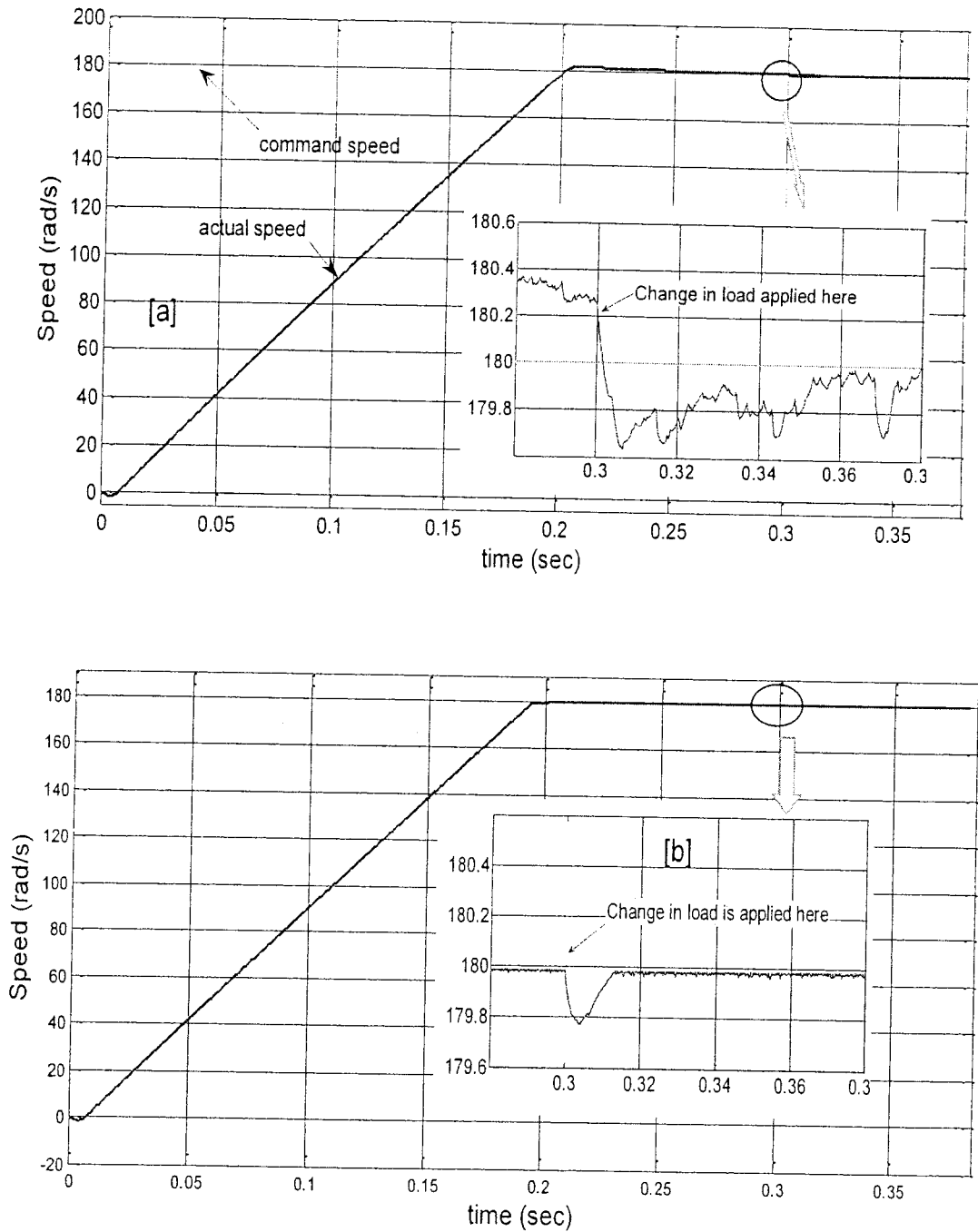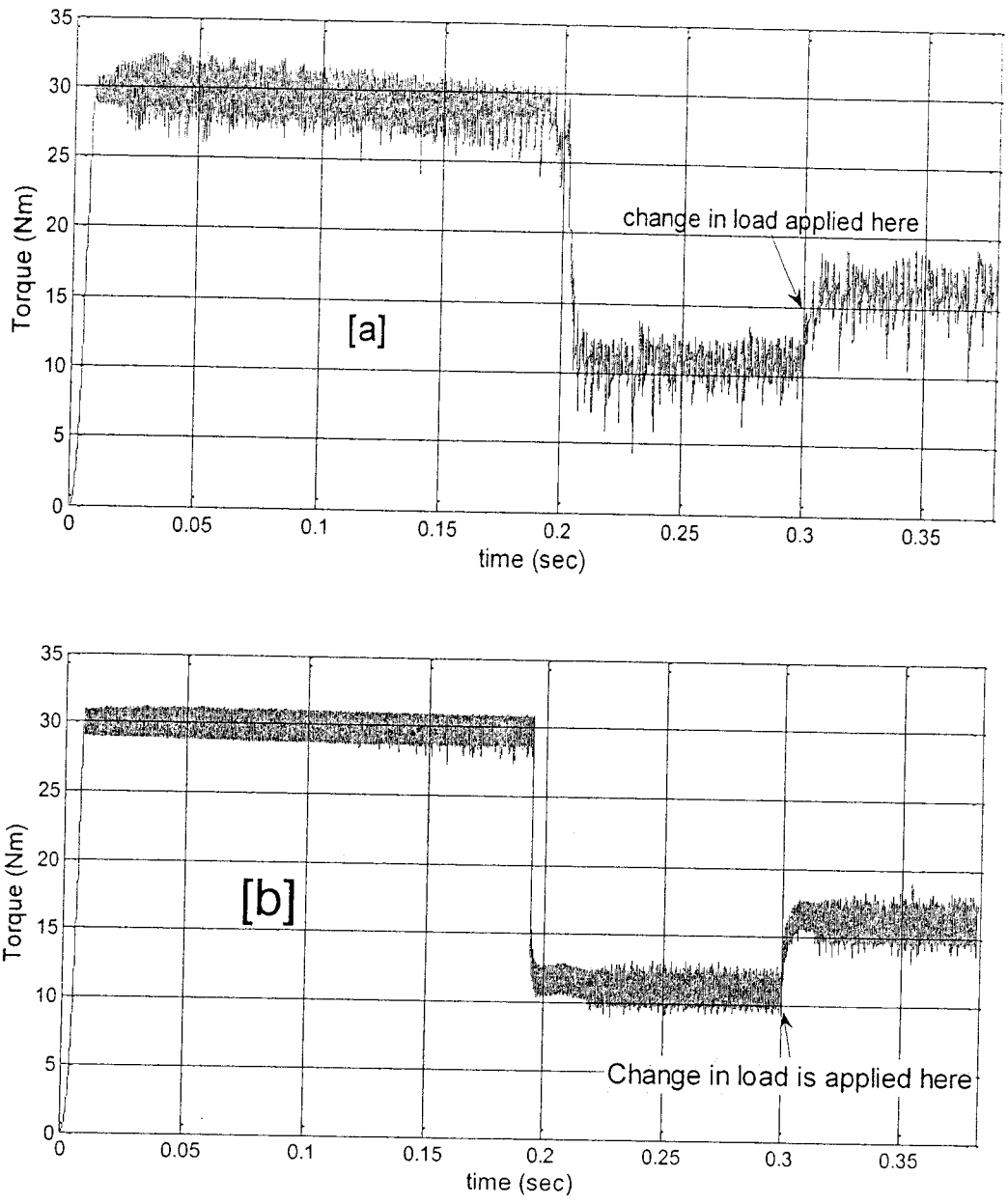
82

Fig. 4.14: Stator current of the IM drive at 50% of rated load. The step change in speed is applied at 0.3 sec., (a) conventional DTC, (b) proposed NFC and variable hysteresis controller based DTC scheme.

83

Fig. 4.15: Speed responses of the IM drive (with zoom-in-view for the interval 0.28-0.38s) for a step change in load from 10-15 Nm at rated speed of 180 rad/s, (a) conventional DTC, (b) proposed NFC and variable hysteresis controller based DTC scheme.
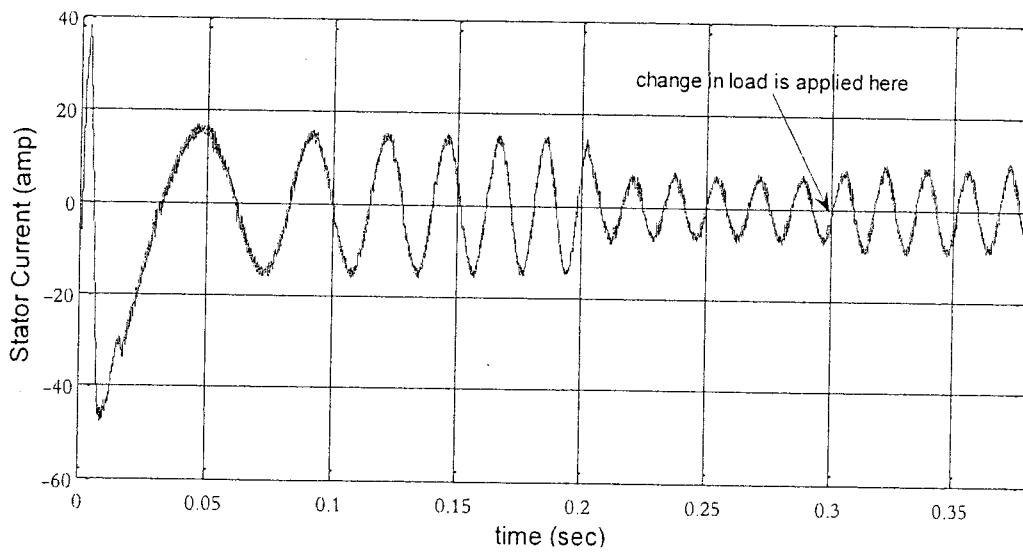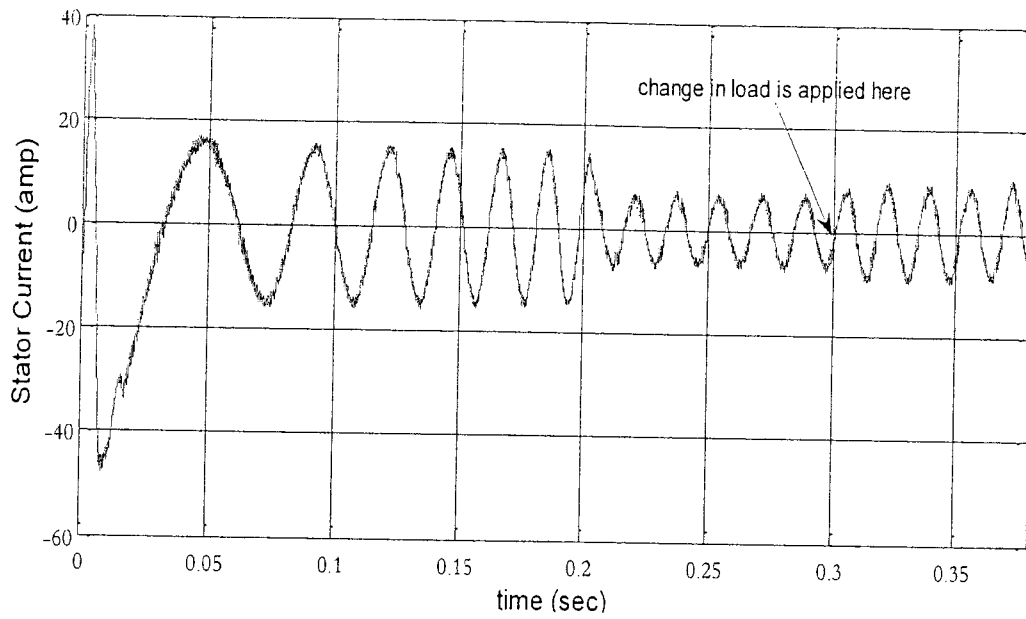
84

Fig. 4.16: Developed Torque responses of the IM drive for a step change in load from 10-15Nm
at rated speed of 180 rad/s; (a) conventional DTC, (b) proposed NFC and variable hysteresis
controller based DTC scheme.

Fig. 4.17: Stator current responses of the IM drive for step change in load from 10-15 Nm at rated speed of 180 rad/s; (a) conventional DTC, (b) proposed NFC and variable hysteresis controller based DTC scheme.
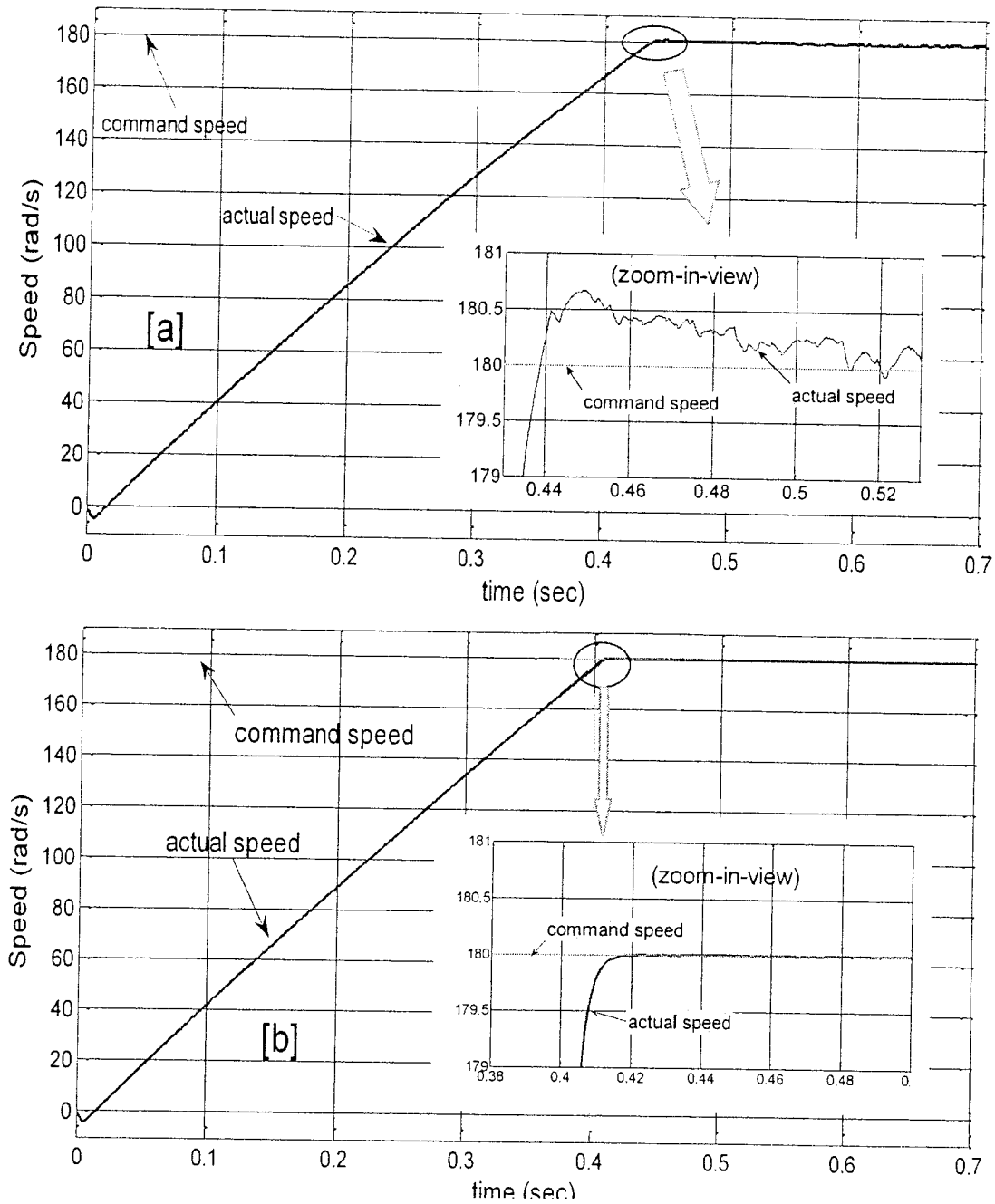
86

Fig. 4.18: Speed responses of the IM drive (with zoom-in-view of the encircled part of response) at rated-load and rated speed of 180 rad/s; (a) conventional DTC, (b) proposed NFC and variable hysteresis controller based DTC scheme.
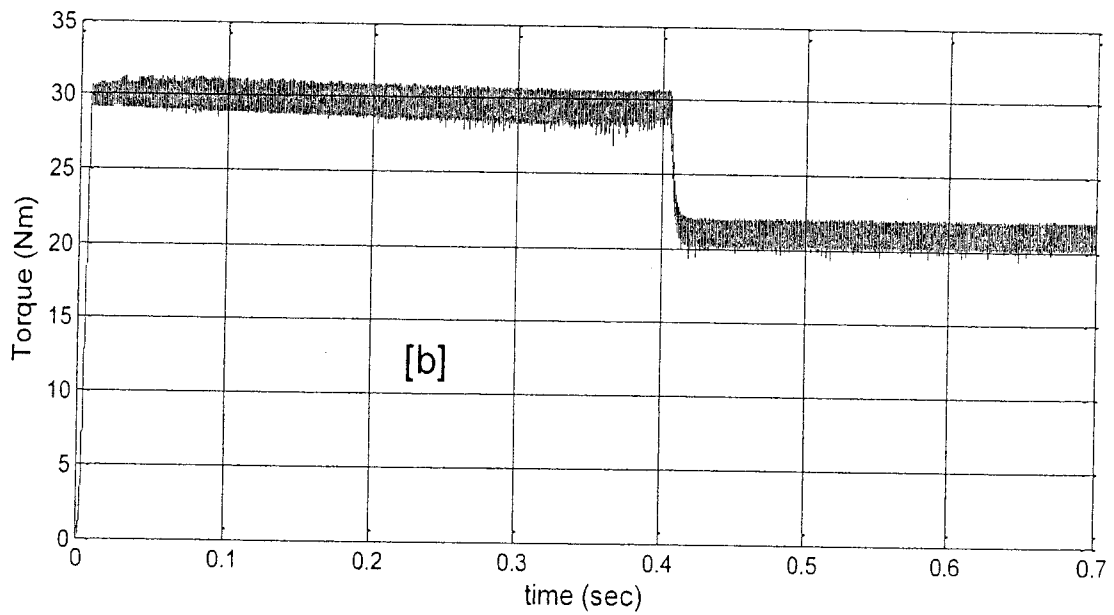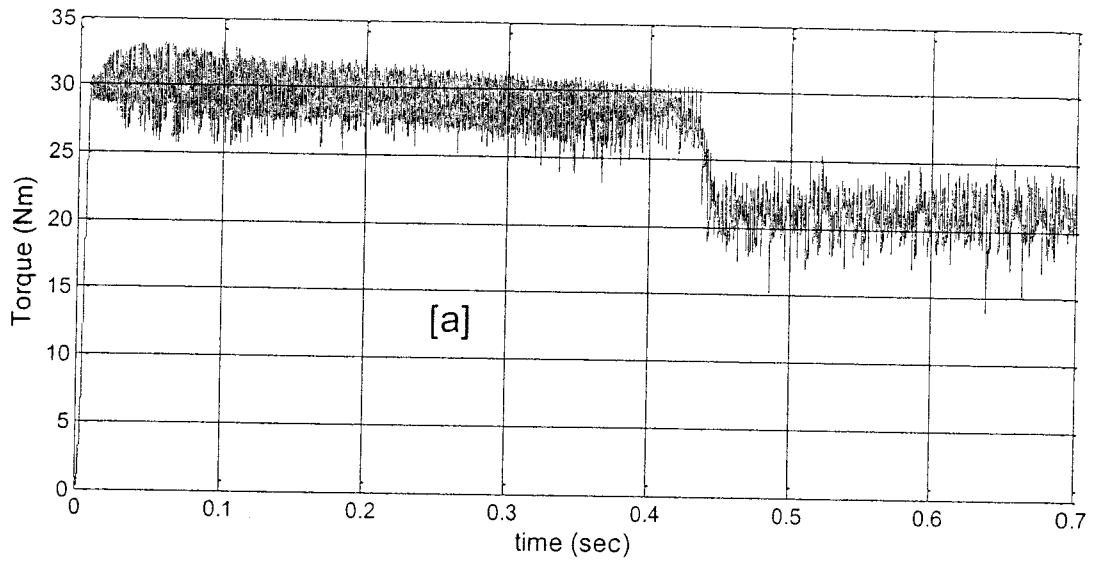
87

Fig. 4.19: Developed Torque responses of the IM drive at rated load (20Nm) and rated speed of 180 rad/s; (a) conventional DTC, (b) proposed NFC and variable hysteresis controller based DTC scheme.

The overall comparison of the proposed DTC scheme with the conventional scheme is shown below in the Table.2. The comparison shows how effective the new proposed scheme in all dynamic respect.

Table-2. Comparison of conventional and proposed DTC schemes

operating condition Parameter	Rated speed at no-load		Rated speed with step load change (10-15Nm)		Step change in speed (120-150 rad/s) at 50% rated load		Rated speed at rated load	
	Conventional	Proposed	Conventional	Proposed	Conventional	Proposed	Conventional	Proposed
% Overshot	1.39	0.01	0.31	0.14	0.89	0.06	0.39	0.02
Rise time (s)	0.132	0.13	0.006	0.005	0.034	0.032	0.438	0.41
Settling time (s)	0.053	0.005	0.06	0.005	0.166	0.038	0.072	0.01
%Speed ripple	0.11	0.02	0.22	0.03	0.11	0.03	0.33	0.01
%Torque ripple	35	11	30	17.5	25	12.5	45	10
%Flux ripple	3.93	2	5	3.33	9.33	3	5.33	1.6
%Current ripple	25	17.08	12.5	8.33	12.5	8.33	12.5	8.33

4.4 Conclusion

The NFC and variable band hysteresis controllers based DTC scheme has been proposed in this chapter. Neuro-fuzzy technique has been used to get both the good feature of FLC and ANN controller. The NFC has been used as a speed controller to improve dynamic speed response. The proposed NFC is simple and hence levies very low computational burden on the processor. The simulation results verify the feasibility of the proposed drive for real life industrial drive applications. The main advantages of the new proposed scheme over the conventional DTC scheme are as follows:

- Improved IM torque response with lesser ripples both in transient and steady states.
- The speed response has lesser overshot, ripples and settling time.
- Lesser transient and steady state currents indicating the better efficiency of the new scheme.
- Smooth with lesser ripples in stator flux linkage.

CHAPTER 5

Real-Time Implementation

5.1 Introduction

The chapter is devoted to the experimental verification of the proposed IM drive. It concisely provides the detail of DSP controller board DS1104 and other supporting equipment used for experimental work. The testing of current and voltage sensors is also discussed. The experimental setup and extensive real-time results are presented to prove the effectiveness of the proposed DTC scheme based IM drive.

5.2 Experimental Setup

The detailed experimental setup for the implementation of the proposed DTC scheme is shown in Figs 5.1 and 5.2. Fig.5.1 shows the whole setup while second figure zoom in the sensor and drive circuits. The schematic diagram of the real-time setup is shown in Fig.5.3. A three phase autotransformer 'Tr' is used as a source of variable AC supply. It is connected to rectifier through a single throw switch 'Sw'. A single assembly 'RFI' encompasses the rectifier, filtering capacitor and inverter. The inverter is equipped with short circuit protection, under voltage and thermal abnormalities. The thermal protection operates on heat sink temperature. The gating signals generated by the DSP board are available on its D/A ports. These signals are not strong

91

enough to trigger the inverted gate bipolar transistors (IGBTs) of the inverter. Therefore, a drive circuit 'Dr1' is used as an interface which also provides isolation between low power control and the high power supply circuits. The inverter output is connected to the test induction motor 'IM'. The supply current and voltage are measured by using two Hall Effect Sensors 'Cs' and a three phase voltage sensor 'Vs', respectively. The current sensors have a linear response over wide range of frequencies up to 250 kHz. Again it need drive circuits 'Dr2' and 'Dr3' between these sensors and A/D ports of the DSP board to make them reasonably strong. The speed of IM is measured by using an optical incremental encoder 'E' which is directly coupled with the rotor
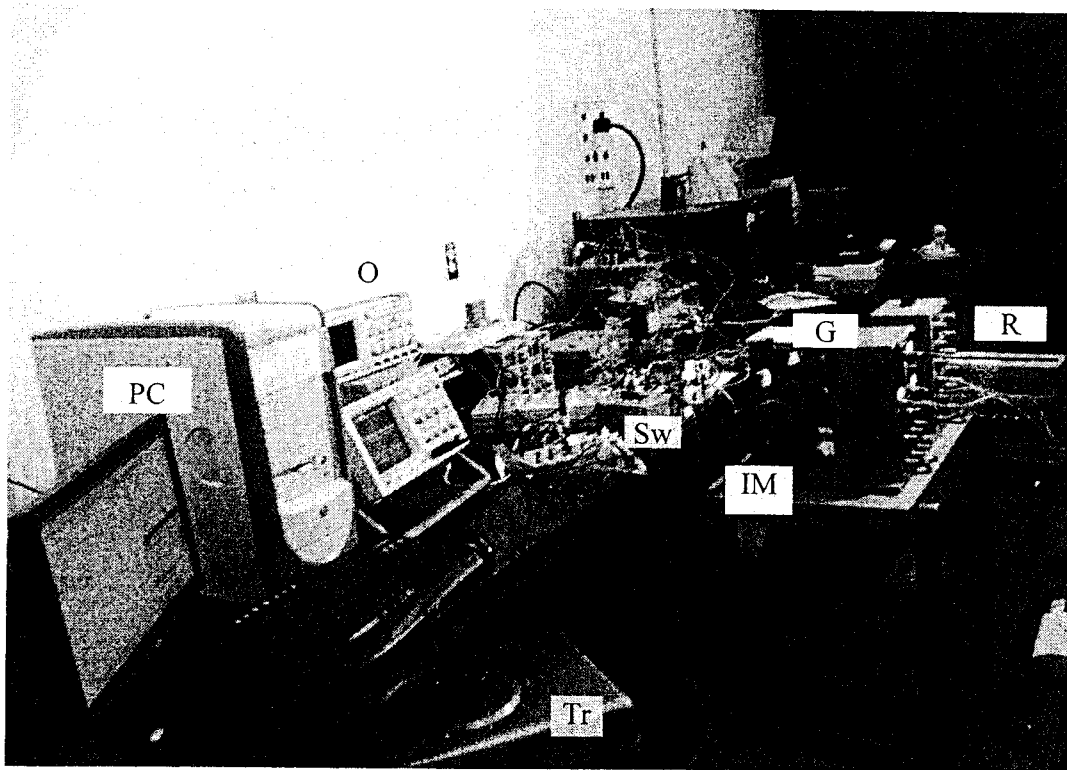

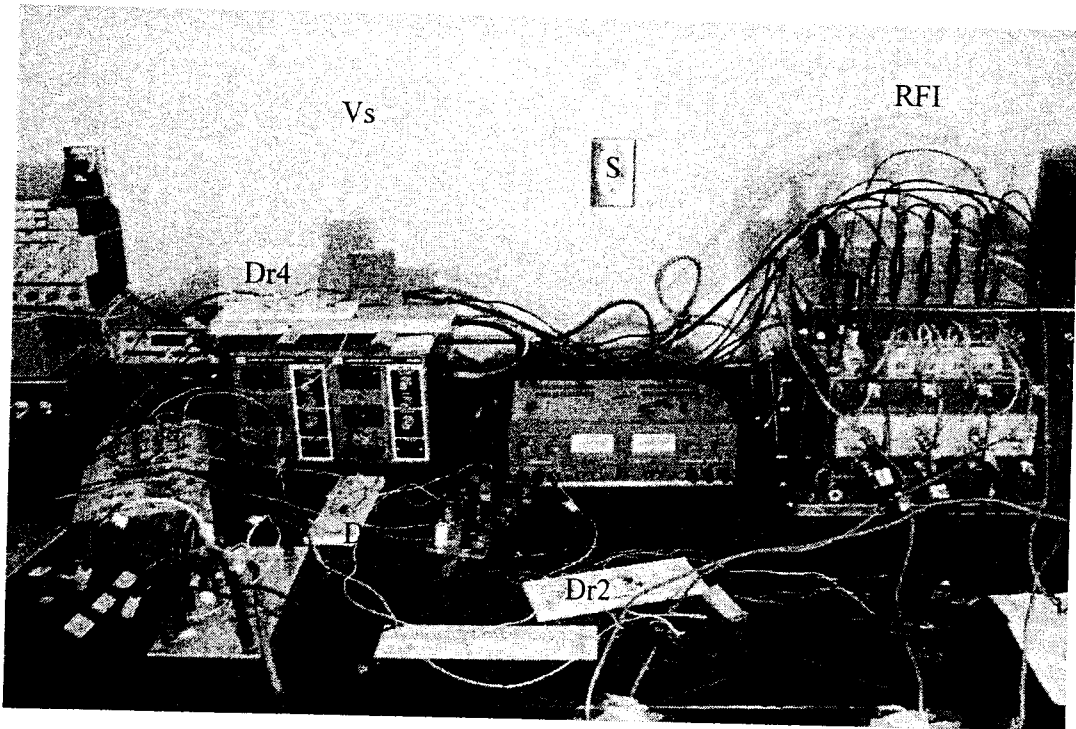Fig .5.1: Experimental setup of the proposed DTC scheme based IM drive.

Fig. 5.2: Experimental setup of the proposed DTC scheme (zoom-in-view).

shaft. A DC generator 'G' is also coupled with the rotor shaft. This generator works as load on the test motor. The rheostat 'R' connected to the terminals of DC generator acts as variable load on the IM. The DSP board DS1104 is connected with the personal computer 'PC' in which the dSPACE software is installed. A digital oscilloscope 'O', is used to capture the desired analog signal from D/A port of the DSP. Both the hardware and software details of the complete motor drive system are detailed in the next sub-sections.
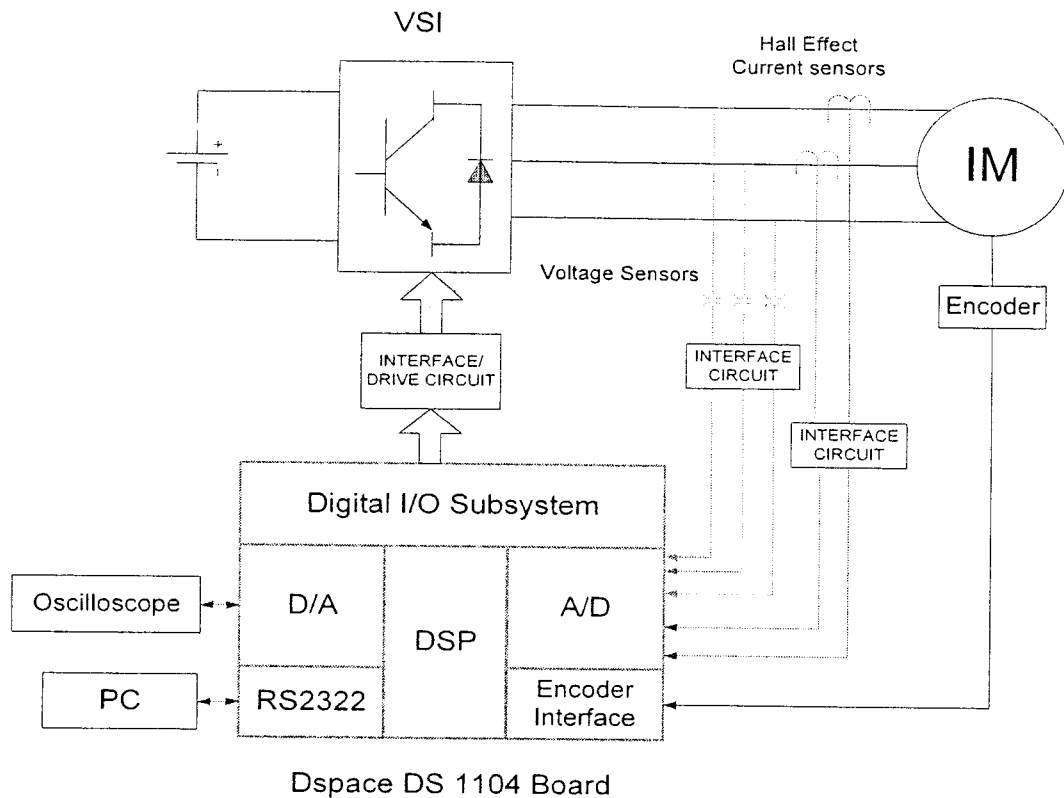
VSI

Hall Effect
Current sensors

IM

Voltage Sensors

Encoder

INTERFACE/
DRIVE CIRCUIT

INTERFACE
CIRCUIT

INTERFACE
CIRCUIT

Digital I/O Subsystem

Oscilloscope

D/A

DSP

A/D

PC

RS2322

Encoder
Interface

Dspace DS 1104 Board

Fig. 5: Block diagram of hardware schematic for VSI fed IM drive.

5.3 Hardware Implementation of the Drive

The DS1104 board is used for the real time implementation of the proposed NFC controller [70]. It is installed and connected with an Intel PC with uninterrupted communication through dual port memory (global and local) to implement the control scheme in real-time. The DS1104 is also equipped with Control Panel CP1104 for its I/O connections. The block diagram of the DS1104 board is shown in Fig.5.4. This board has Texas Instrument MPC8240 64-bit

94

digital signal processor. The DS1104 board uses a Power PC type PPC603e processor which operates at the clock of 250 MHz frequency with 32 KB cache. This board has a 32 MB of SDRAM global memory and 8 MB of flash memory. For the peripheral devices connection CP1104 has each eight A/D (analog to digital) and D/A (digital to analog) ports. The control panel has two encoder interfaces (Inc1 & Inc2) for the connection of incremental encoders. The rotor position is sensed by an optical incremental encoder which is directly coupled to its shaft and is fed back to the DSP board through Inc2 interface in present case.
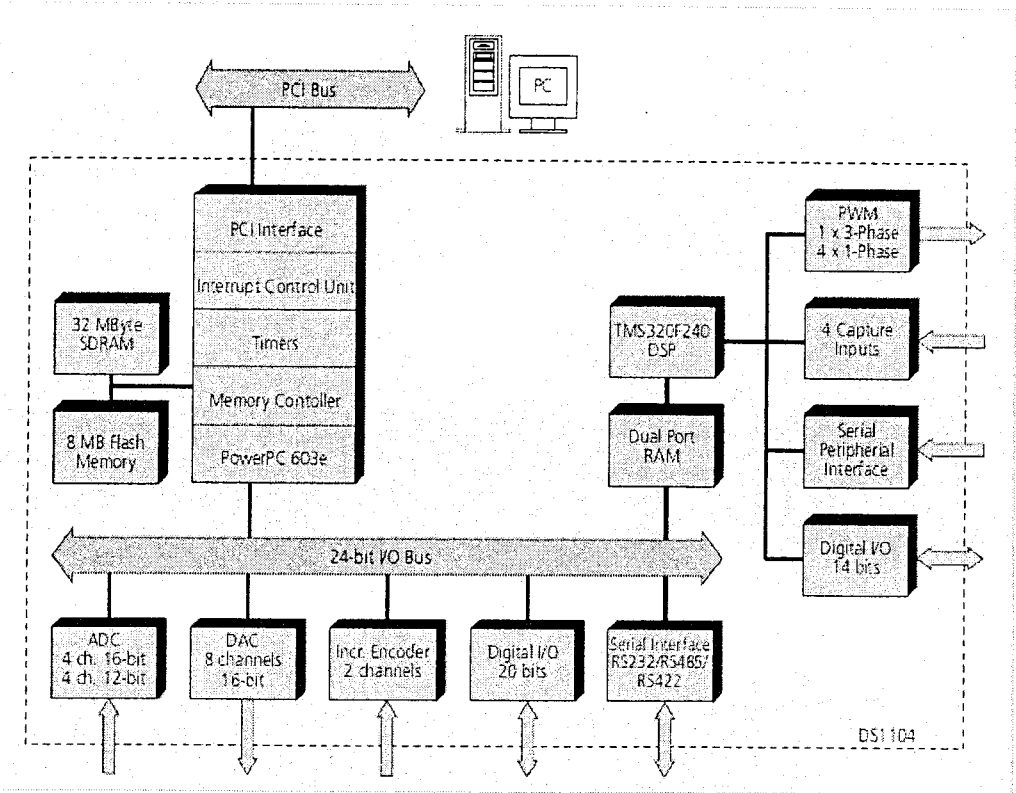

Fig .5.4: Block diagram of DS1104 board.

95

The encoder generates 1000 pulses per revolution. By using a built-in 4-fold pulse multiplication the output of the encoder is increased to 4x1000 pulses per revolution. The encoder pulses are counted by a 24-bit position counter in the software. After each revolution the counter is reset by the index pulse generated by the encoder. The motor speed is calculated from the measured rotor position angles by using a mathematical relation. The 16-bit micro controller, TI TMS320F240, acts as a slave processor and provides the necessary digital I/O ports configuration. The slave processor can also be used for digital I/O subsystem configuration. The actual motor voltages and currents are measured by using a three phase voltage and two Hall-effect sensors, respectively. After reasonable amplification by the driver/interface circuits these signals are fed back to CP1104 through A/D channels. These driver circuits work in two folds. First these reduce the noise level and then they amplify these signals reasonably to meet the requirements of CP1104 board. The interface circuits consist of non-inverting type amplifiers and are attached as Appendix-C. For the balanced motor load or ungrounded neutral, only two current sensors are required and third phase current is calculated using KCL. The motor torque and stator flux linkage are estimated by using these voltage and current signals. These estimated motor parameters are compared with their command parameters generated by the NFC. Using the digits produced by the torque and flux hysteresis the conventional DTC table produces the gating signal for the inverter. The six logic signals are the output of the DSP Board and fed to the base drive circuit of the IGBT inverter power module. The outputs of the digital I/O subsystem of the DS 1104 are six pulses with a magnitude of 5 V. This voltage level is not sufficient for the gate drive of IGBTs which needs almost 15 volts. Therefore, the voltage level is shifted from +5 V to +15V through the base drive circuit with the chip SN7407N as shown in Appendix C. Thus the work of the motor drive starts in cyclic process.

5.4 Software Development for Real-Time Implementation of the Proposed IM Drive

The DS1104 board is inherently equipped with the microprocessor. Therefore, it can work independently without using the PC. Though the processor is connected with the PC slot still it performs all of its tasks without using it. This board needs to download the drive system software for its functionality. Therefore, to implement the control algorithm, a real-time Simulink model of the whole drive system (shown in Appendix-D) is developed. Using the control desk software [70] this model is downloaded to the DS1104 board. The permissible maximum sampling frequency for the proposed work is found to be 10 KHz. The sampling frequency over this limit causes "overrun error" and stops the board's processor to run it.

The flow chart for the real-time implementation of the proposed drive system is shown in Fig.5.5. For startup purposes all the variable of the program needs initialization. After initialization the timer interrupt routine is setup which reads these variables (stator currents , voltages and rotor position) by using their respective sensors. The signals measured by these sensors are so adjusted that they present the actual quantities. The adjustment procedure is explained in next section. The calculation for rotor speed by using the optical position encoder is also explained in the same section. These variables are collected at the A/D ports of Control Panel of the board.
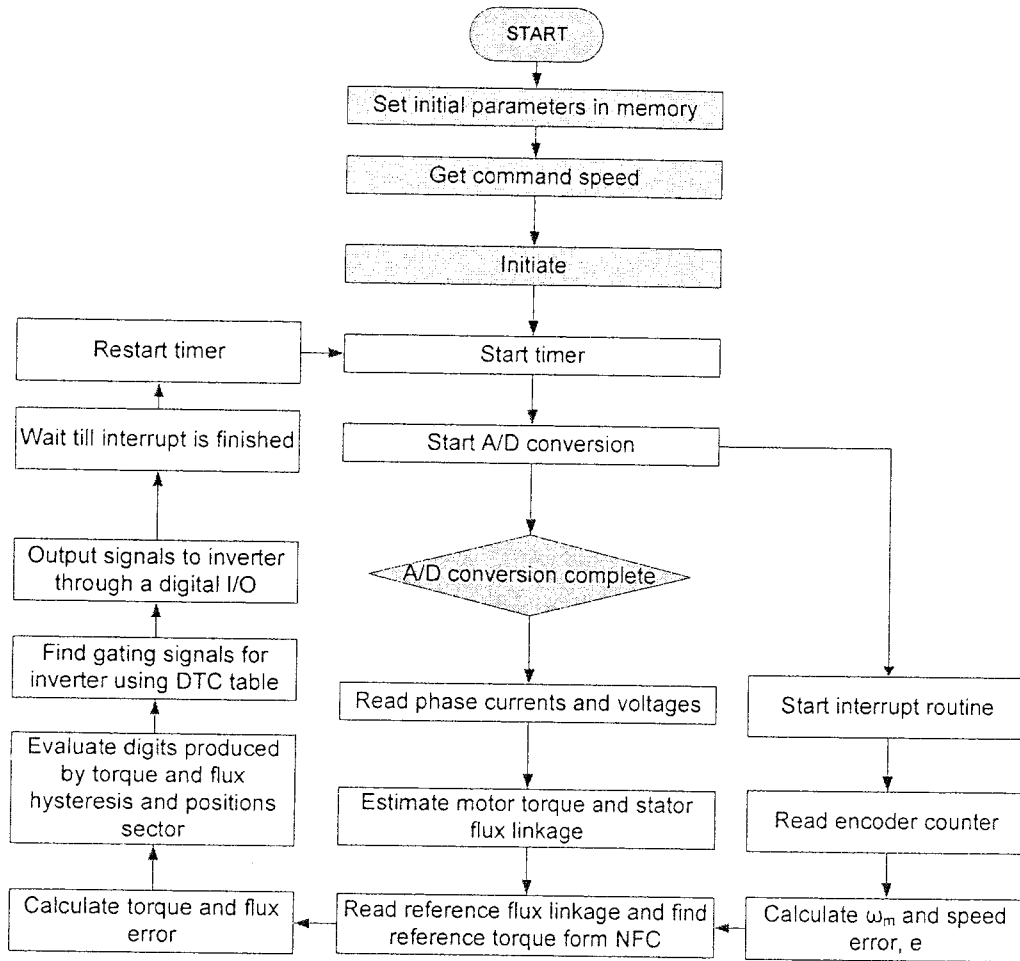
Fig.5.5: Flow Chart of the software development for real-time implementation of the proposed DTC based IM drive.

Using the speed error the reference motor torque is calculated by the processor of the board. Similarly, the calculation for estimated torque and flux linkage are performed by the processor using the drive software. All the calculated and measured values as explained above

98

such as stator voltages, currents and rotor speed along with initial parameters stored in memory are used to compute the gating signal for the inverter by using the drive software. These gating pulses are available at the I/O subsystem of the board and are applied to the inverter IGBT switches through drive circuit. Then process continues in cycle to run the IM.

5.5 Signal Measurement and Adjustments

5.5.1 Rotor Speed Measurement

The rotor position angle is measured by an optical position encoder 'XH25D-SS-1000-ABZC-28V/V-SM18' shown in Fig.5.6. The position can be calculated in radian by the equation

$$\theta_m\,(rad) = (2\Pi/1000)\,\text{p} \tag{5.1}$$

Where 'p' is the number of pulses per shaft turn, counted in the counter. The encoder produces 1000 pulses for each turn of the shaft. The encoder counter is reset by the index pulse after each turn of shaft rotation. It means max possible rotor shaft position is 360^0m or 2Π radians. Then the rotor speed is computed from the measured rotor position angles using backward difference equation. The Optical Position Encoder is shown in Fig.5.6. Based on the calculated speed, the speed error between actual and reference speed is calculated.
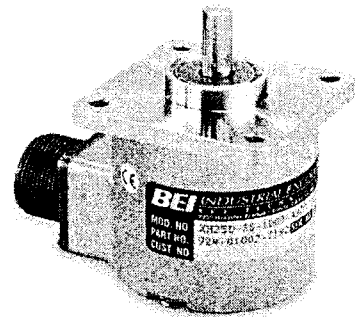

Fig.5.6: Optical position encoder

99

5.5.2 Stator Current Measurement

Hall-effect current sensors are used for the measurement of the IM stator currents. These sensors produce output voltage proportional to the current of the cable passing through the sensor's recess like a clamp-on ammeter. These signals after amplification by the interface circuit are supplied to the A/D ports of the control panel. These signals need to be the actual load current for the drive system software. Hence they need some adjustment to do the desired task. The real-time software program for sensor test is given in Appendix-D. The practical sensor's test circuit is shown in Fig.5.7.
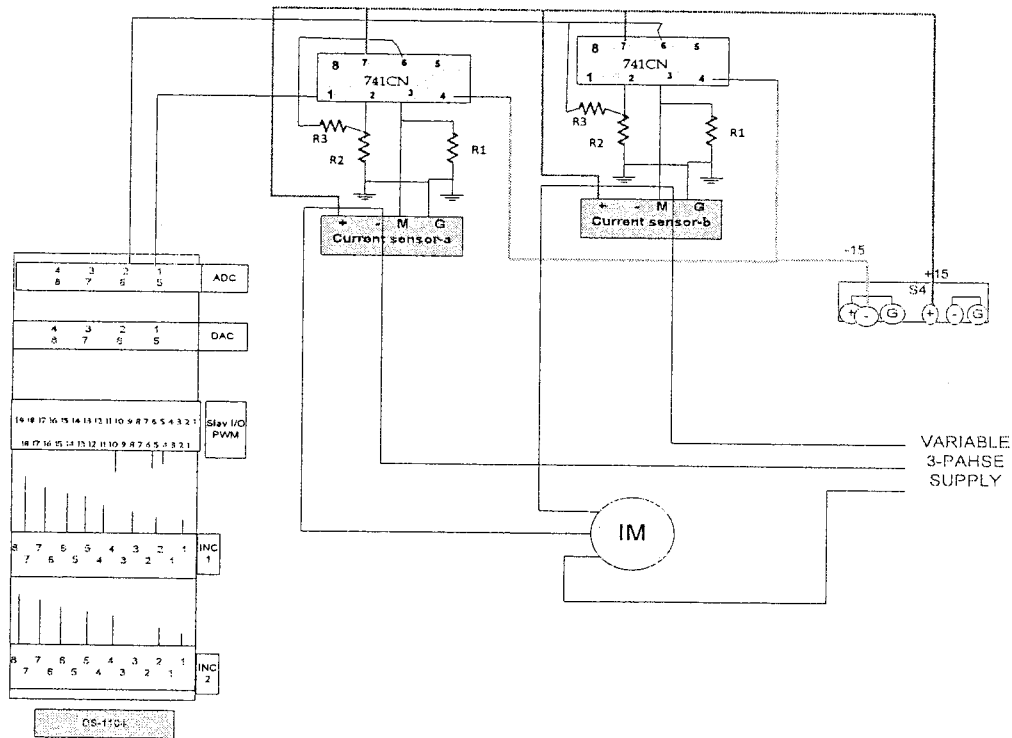
Fig. 5.7: Connection diagram for current sensor test.

The detailed calculations for the multiplication factor and vertical offset adjustment for the two

sensors (for phase-a & b) are given below in Table-3.

Table-3. Calculation for current gain for real-time IM drive software.

REQUIRED OFFSET AND GAIN FOR PHASE-A CURRENT SENSOR

Sr. No.	Source current(rms)	Positive Peak	Negative Peak	Required Vertical Offset	dSpace rms	Gain Required
1	0.5	0.0125	-0.019	0.00325	0.011	45.455
2	0.7	0.017	-0.024	0.0035	0.014	50
3	1	0.026	-0.034	0.004	0.021	47.619
4	1.2	0.0325	-0.039	0.00325	0.025	48
5	1.5	0.042	-0.048	0.003	0.032	46.875
6	1.7	0.048	-0.054	0.003	0.036	47.222
7	2	0.056	-0.065	0.0045	0.043	46.512
		AVERAGE		0.0035		47.38328571

(a)

REQUIRED OFFSET AND GAIN FOR PHASE-B CURRENT SENSOR

Sr. No.	Source current(rms)	Positive Peak	Negative Peak	Required Vertical Offset	dSpace rms	Gain Required
1	0.5	0.011	-0.017	0.003	0.01	50
2	0.7	0.017	-0.023	0.003	0.01	70
3	1	0.024	-0.03	0.003	0.02	50
4	1.2	0.029	-0.035	0.003	0.02	60
5	1.5	0.037	-0.043	0.003	0.03	50
6	1.7	0.042	-0.048	0.003	0.03	56.67
7	2	0.051	-0.056	0.0025	0.04	50
		AVERAGE		0.002928571		55.24

(b)

101

Hence the motor currents obtained through A/D channels 1 and 2 are multiplied by the gain 47.383 and 55.24 for phases 'a' & 'b', respectively, in order to get the actual motor current values in software. These constants depend on the Hall-effect sensors specifications, the resistors used at the output node of these sensors and the resistors used in the interface circuit. The current waves for the two sensors before and after the application of the respective adjustment factors are shown in Fig.5.8 and 5.9 respectively. It is found from these figures that the currents after adjustments are more symmetrical than those of without adjustments.
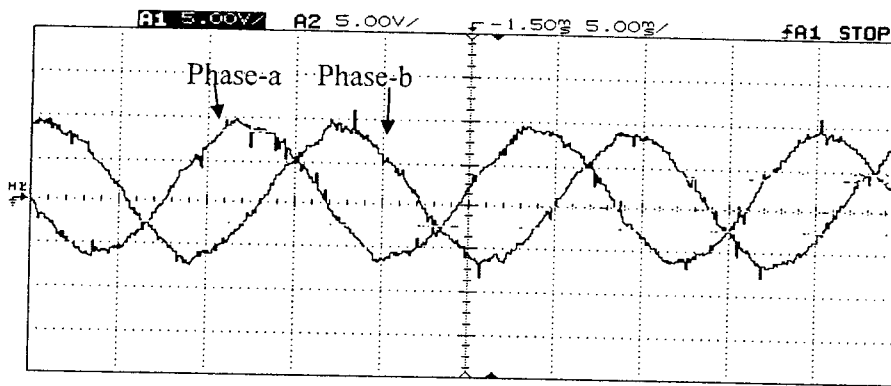
Fig. 5.8: Stator currents (phase-a and phase-b) without application of adjustments
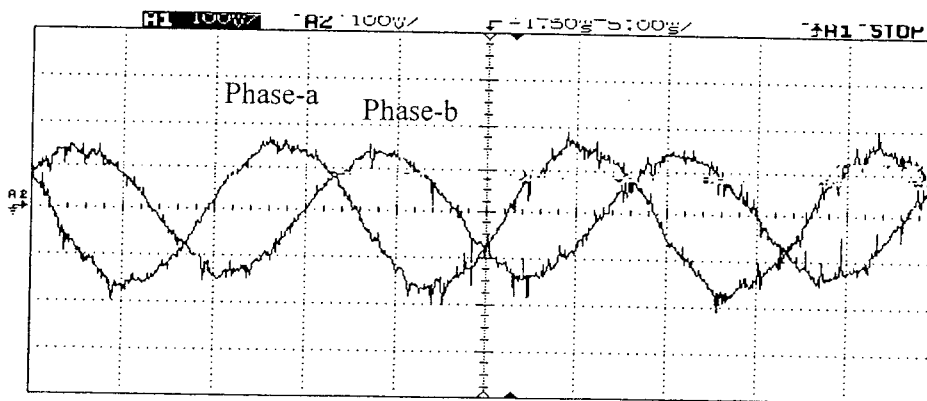
Fig. 5.9: Stator currents (phase-a and phase-b) after application of adjustments

5.5.3 Stator Phase Voltage Measurement

The three phase AC voltage transducer CE-VJ41-10MS3-0.5 is used for the measurement of the IM stator phase voltages. This transducer is self powered and hence need no biasing voltage. The sensor produce output phase voltages proportional to its relevant input phase voltages. The calculations for transformation ratio of the transducer are shown in Table-4 below:

Table-4. Calculation for transformation ratio of the voltage transducer

MULTIPLICATION FACTOR/GAIN DETERMINATION

INPUT			OUTPUT								
Vai	Vbi	Vci	Vao		Vbo		Vco		overall tranformation ratio		
(rms)	(rms)	(rms)	(p-p)	(rms)	(p-p)	(rms)	(p-p)	(rms)	ph-a	ph-b	ph-c
29.8	29.5	29.8	2.4	0.828	2.28	0.8	2.44	0.827	35.99033816	36.875	36.03385732
39.5	39	39.5	3.2	1.09	3.04	1.06	3.16	1.09	36.23853211	36.79245283	36.23853211
50	49.5	49	4	1.38	4	1.36	3.84	1.32	36.23188406	36.39705882	37.12121212
70.7	69.5	70.2	5.52	1.93	5.36	1.85	5.52	1.91	36.63212435	37.56756757	36.7539267
100.6	99.6	100	8	2.78	7.6	2.64	7.8	2.7	36.18705036	37.72727273	37.03703704
124.7	122	123	9.8	3.42	9.4	3.25	9.6	3.31	36.4619883	37.53846154	37.16012085
								AVERAGE	36.2903	37.1496	36.7241

The interface circuit after the transducer amplifies the signal to a reasonable level for dSPACE. These signals after the interface circuit are supplied to the A/D ports of the control panel. In order to get actual voltage there need some adjustments. The real-time software

program for voltage sensor test is attached as Appendix-D. The practical sensor test circuit is
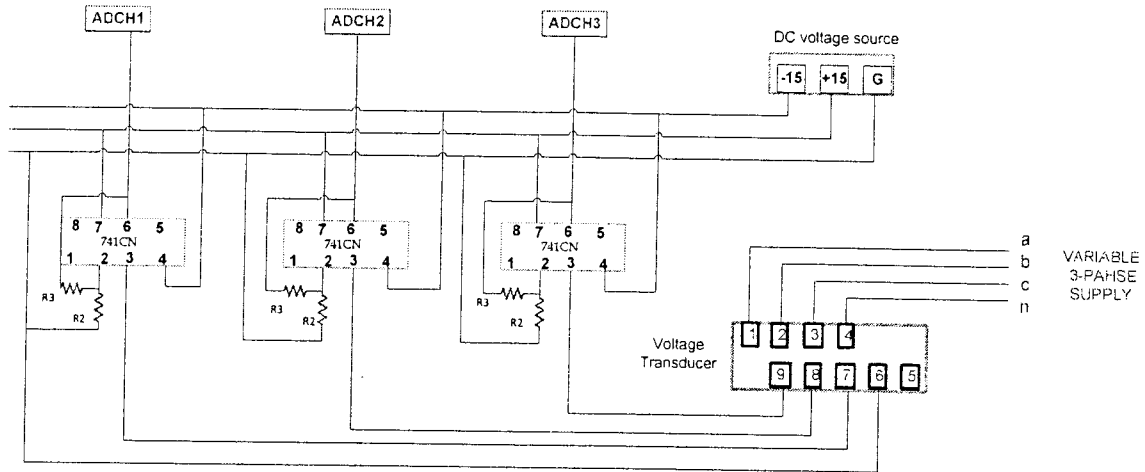
shown in Fig.5.10.

Fig. 5.10: Connection diagram for voltage sensor test.

The waveforms for the three phase supply voltage which are out of DS1104 board are shown in

Fig.5.11. The rms value of the supply phase voltages is given below:

$$V_a = 50.2V \; ; \; V_b = 49.4V \; ; \; V_c = 49.8V$$

From the figure it is clear that the voltage waveforms for the three phases are not

symmetrical w.r.t. the x-axis. Hence it needs some wave shift. This DC values for the three

phases are figured as 0.002, 0.002338 & 0.002, respectively. From the peak values obtained

from the dSPACE and supply phase voltages, the multiplying factors for the three phases are

calculated as 374.1552, 374.9478 & 343.6946, respectively. Hence the three phase voltages

obtained through A/D channels 1, 2 & 3 are multiplied by their respective multiplying factors to

get their actual values in software. These constants depend on the voltage sensors specifications,

104

the resistors used at the output node of these sensors and the resistors used in the interface circuit. The dSPACE voltage waves for the two sensors after the application of the respective adjustment factors are shown in Fig.5.12. It is found that the voltage waveforms after gain and offset adjustments are more symmetrical and smooth as compared to those of without gain and offset adjustments.
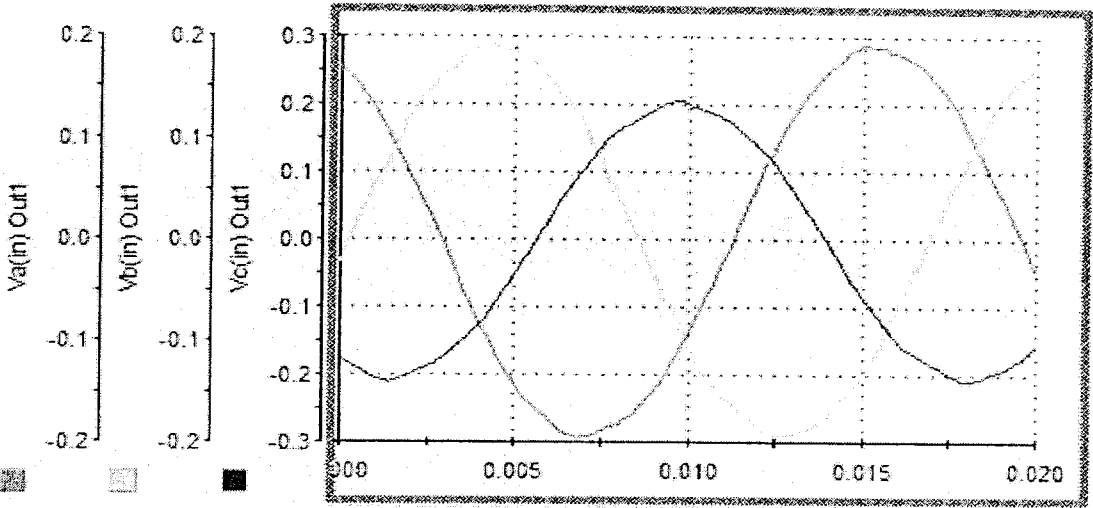
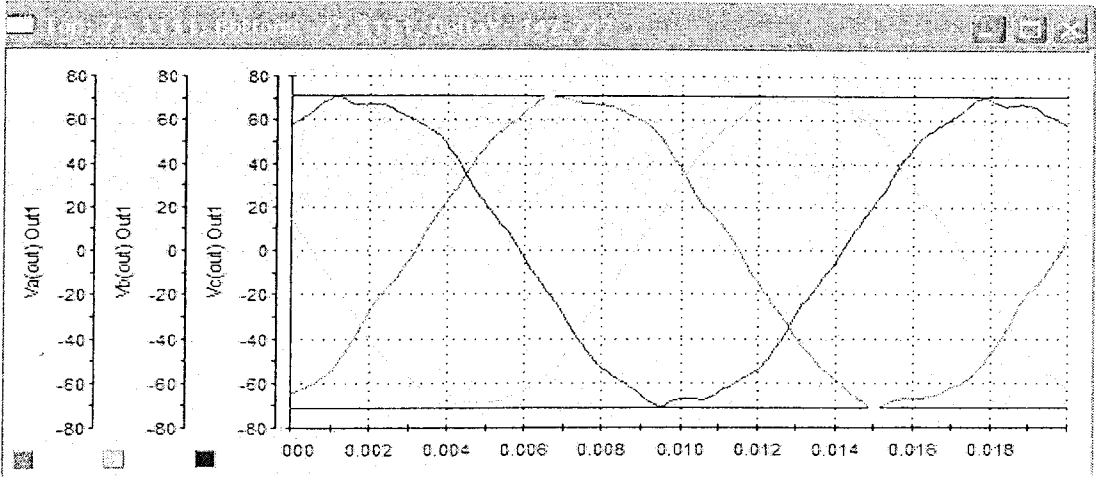Fig .5.11: Stator phase voltage (v_a, v_b, v_c) without application of adjustments

Fig. 5.12: Stator phase voltage (v_a, v_b, v_c) after application of adjustments

105

5.6 Experimental Results

The effectiveness of the proposed NFC and adaptive hysteresis based DTC scheme is verified by the experimental work. Extensive experimental tests are carried out under various operating conditions of the IM. The parameters of the IM used for real time implementation of the DTC scheme are given in Appendix-A. The results for PI-controller based conventional DTC scheme are also shown for comparison purposes.

Figures 5.13-5.15 show the different real time results of the IM drive at no-load and command speed of 180 rad/s. Figures 5.13(a) & (b) shows the speed responses using the conventional and proposed DTC schemes. It is clear from the figures that the proposed DTC scheme has lesser settling time than the conventional DTC scheme. Additionally, the proposed DTC scheme exhibits lesser speed ripples in both transient and steady states. For safer operation of the motor, the input voltage is applied to the inverter through variac and rectifier arrangement gradually but as quickly as possible. Fig.5.14 shows the steady state stator current response for phase-a and phase-b for the proposed DTC scheme. The current response is very smooth and almost ripples free for both the stator phases. Fig.5.15 presents the steady-state torque responses of the conventional and proposed DTC schemes. To clearly compare the two responses, the zoom-in-views of the shaded portion of the responses have also been shown. The torque ripples have been significantly reduced in the proposed scheme in steady-state. The performance for a step change of command speed is also investigated for a sudden change of command speed from 100 rad/s to 150 rad/s at no-load. Figures 5.16 (a, b) show the results for the step change in load applied to the IM drive. By comparing Figure5.16 (a) with 5.16 (b) it is evident that the motor can achieve the targeted change in speed more smoothly and within lesser time for the proposed

DTC scheme as compared to the conventional DTC scheme. Fig.5.17 is a zoom-in-view of Fig.5.16(b). It shows that how smoothly the proposed DTC scheme achieves the change in command speed without any significant speed/current ripples.
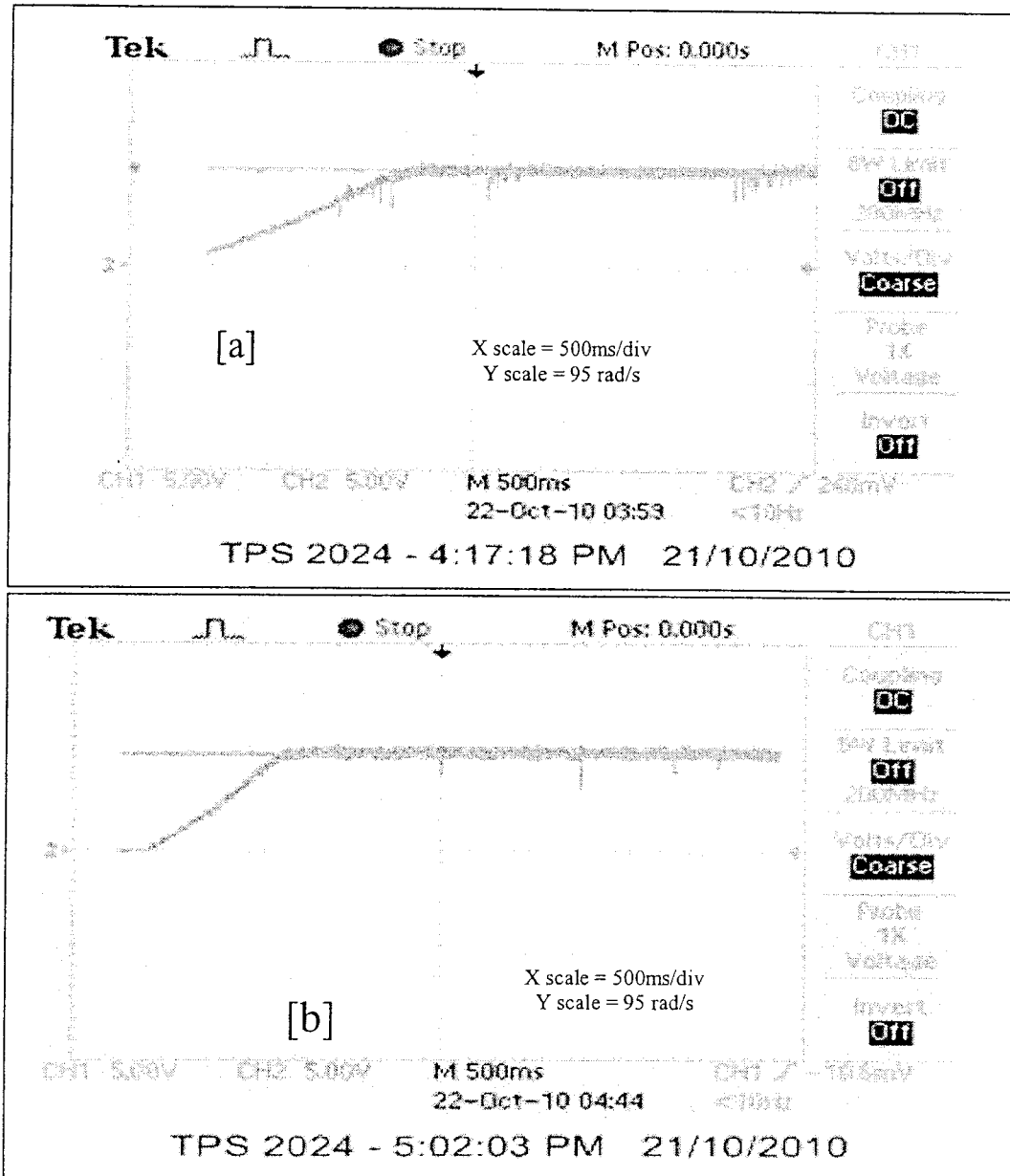

Fig. 5.13: Speed response of the IM drive at no-load and rated speed of 180 rad/s; (a) conventional DTC, (b) proposed NFC and variable hysteresis controller based DTC scheme.
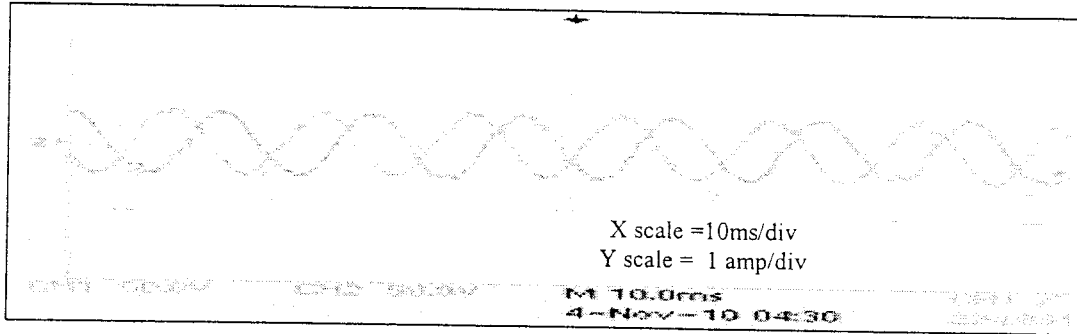
X scale =10ms/div
Y scale = 1 amp/div

M 10.0ms
4-Nov-10 04:30

Fig. 5.14: Steady state current response I_{sa} & I_{sb} for command speed of 180 rad/s at no-load.

A1 5.00V/   A2 5.00V/   0.00s 500m/   Auto A2 RUN

Framing error

(a)

X-scale:0.5s/div
Y-scale: 1Nm/div

A1 5.00V/   A2 5.00V/   0.00s 500m/   A2 STOP

Framing error

(b)

X-scale: 0.5 s/div
Y-scale: 1Nm/div
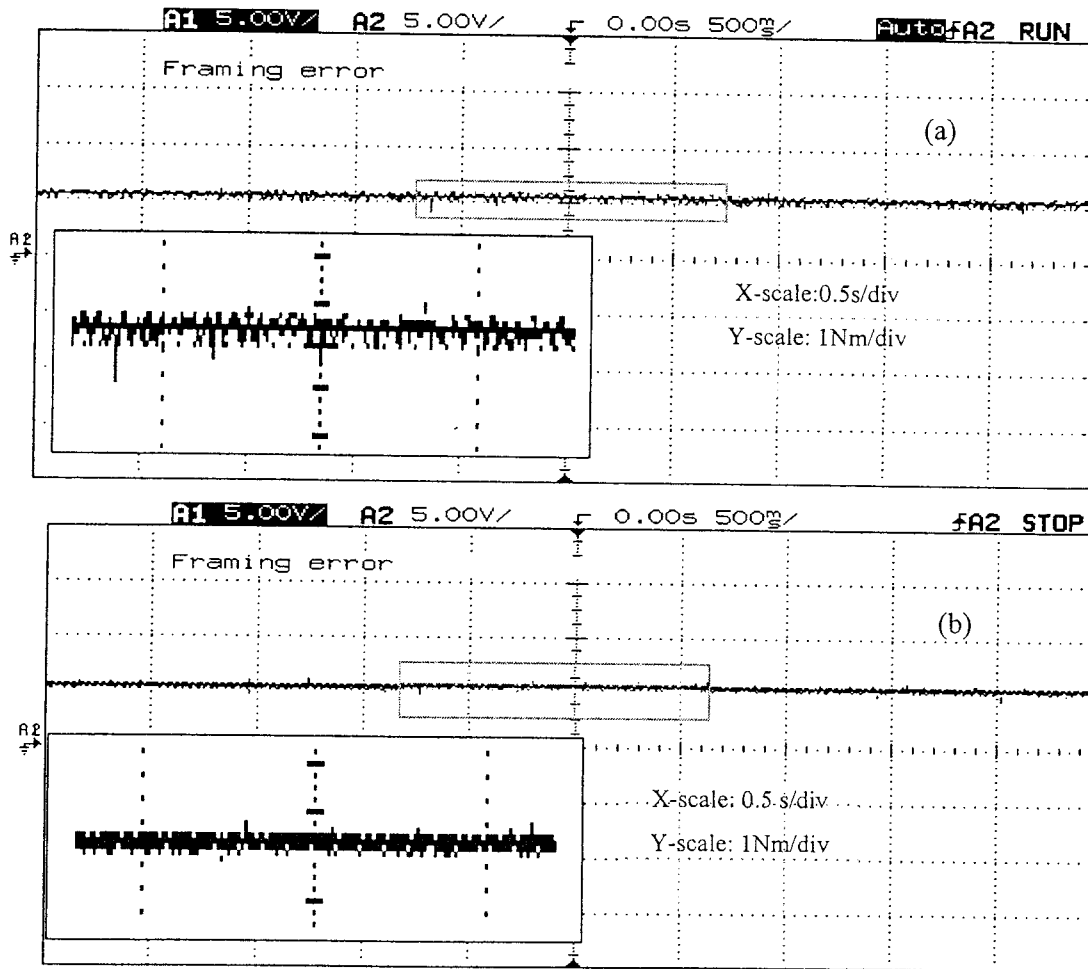
Fig. 5.15: Steady state experimental torque responses of the IM drive for command rated speed

of 180 rad/s at no-load; (a) conventional DTC, (b) proposed DTC scheme.

108
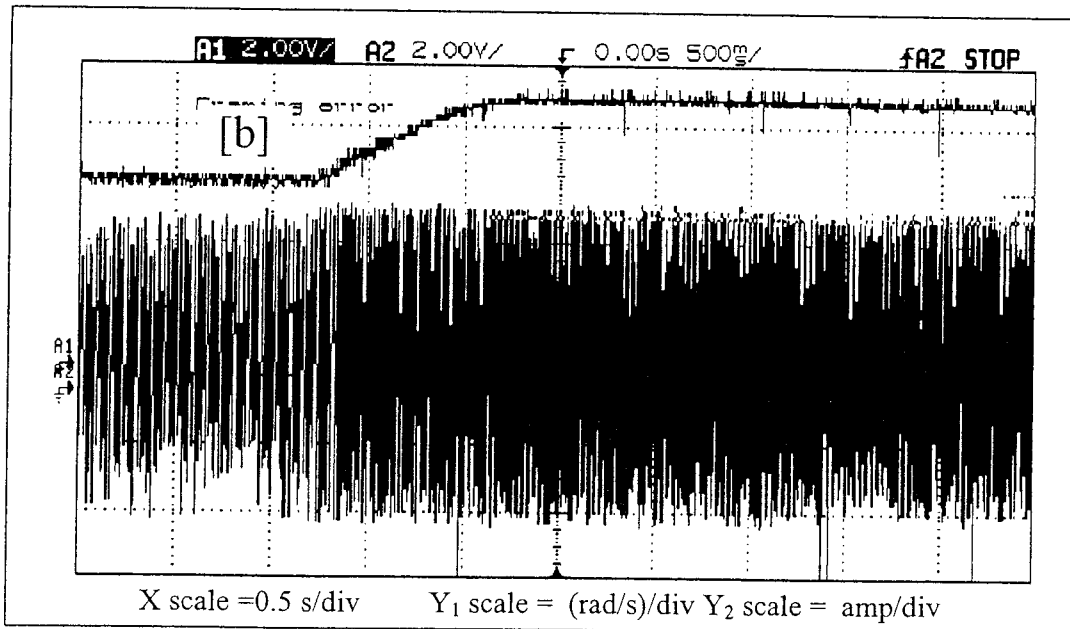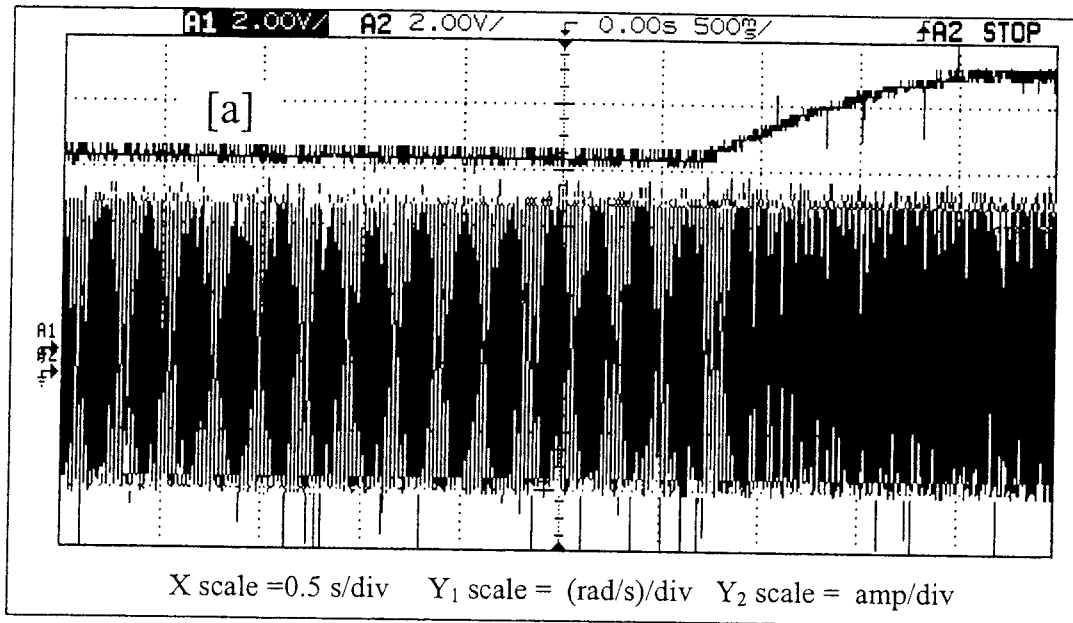
Fig. 5.16: Experimental speed and stator current responses for command step change in speed from 100-150 rad/s (a) conventional DTC, (b) proposed NFC and variable hysteresis controller based DTC scheme.
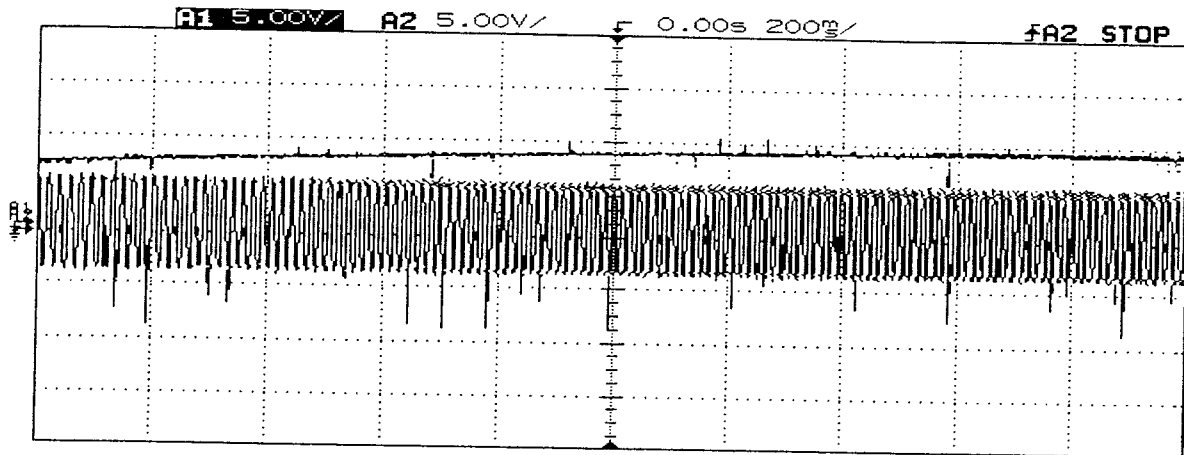
Fig. 5.17: Experimental Transient speed and stator current responses for command step change in speed from 100-150 rad/s for the proposed DTC scheme.

5.7 Conclusion

The proposed NFC and band adapted hysteresis controllers based DTC scheme was implemented in real-time in this chapter. The detailed implementation procedure was also described. The performance of proposed scheme was compared with the conventional DTC scheme in real-time. From the comparison made on the basis of the responses generated by the two schemes one can conclude that there are lesser speed and torque ripples in the proposed DTC scheme as compared to the conventional DTC scheme. Moreover, the proposed DTC scheme achieves the command speed with less settling time and smooth stator current.

110

CHAPTER 6

Conclusion and Future Scope

6.1 Conclusion and Achievements

The major conclusion for the work presented in this thesis may be drawn as follows:

- A new stator flux linkage sector selection algorithm has been developed and tested in this thesis. The proposed algorithm is simpler as compared to the conventional algorithm while maintaining the equivalent performance.

- The conventional fixed band hysteresis comparator of the DTC scheme was replaced by the band adapted hysteresis comparator. The proposed hysteresis controllers are quite better than the conventional hysteresis controller in terms of reduction in stator flux and motor torque ripples.

- This thesis also developed a new TSK-type neuro-fuzzy controller for speed control of an IM. The proposed NFC is very simple but effective. It improved the

dynamic performance of the IM drive. The NFC is found to be faster and accurate as compared to the conventional PI-controller.

- The proposed NFC and the adapted hysteresis controller based DTC scheme for IM drive was implemented in real-time using DSP board DS 1-004 for a laboratory 1/3 hp motor. The performance of the proposed DTC scheme was tested and compared with the conventional DTC scheme.

- The proposed NFC and DTC based IM drive exhibits better dynamic speed response as compared to the conventional DTC scheme. It achieves the targeted/command speed with lesser settling time. Moreover, the speed response is smoother with lesser ripples in steady-state. These factors prolong the motor life by having lesser vibration and noise.

6.2 Future Scope

The DTC scheme used in this work did not consider the estimation of stator flux at initial transient condition in order to avoid the complexity in real-time. In order to further enhance the torque and flux responses one can estimate the stator flux online at all time based on Eqns. (3.1) & (3.2).

The learning/training rate of the NFC is considered constant in this work in order to make the training technique is simple. But to improve the dynamics response of the drive systems with system disturbances and parameter variations an adaptive learning rate may provide better results.

112

The researchers have introduced many speed sensorless techniques. The use of expensive optical speed sensor may be eliminated by using some speed sensorless technique. This will improve the cost benefit ratio of real-time implementation.

References

[1]   R. Fei, E.F. Fuchs, and H. Huag, "Comparison of Two Optimization Techniques as applied to Three-Phase Induction Motor Design,"*IEEE Trans. Energy Conversion*, vol. 4, no. 4, pp. 651-660, Dec 1989.

[2]   The daily, New York Times, newspaper, 18 Dec, 2009.

[3]   S.J. Chapman, *Electric Machinery Fundamentals*, New York: Mcgraw-Hill, 1999.

[4]   A. M. Trzynadlowshi, *The field orienctation principle in control of inductioni motors*, Kluwer Academic, 1994.

[5]   I. Ludtke, and M.G. Jayne, "A comparative study of high performacne speed control strategies for voltage sourced PWM inverter fed induction motro drives," 7th *Internationial Connference on Electrical Machines and Drives*, 11-13 September 1995, university of Durham, UK.

[6]   J. W. Finch, "Scalar and Vector: a simplified treatmet of induciton motor control performacne", *IEE colloguium on Vector Control Revisited*, digest no. 1998/99, pp. 2/1-2/4.

[7]   Marek Stulrajter, Baleria Hrabovcova and Mark Franks, "Permanent Mangnets Synchronous Motor Control Theory," *Journal of Electrical Engineering*, vol. 58, no. 2, pp. 79-84, 2007

[8]   K.W. Ng, and C.W. Poon, "Computer Simulation on a Typical VVVF Elevator drive-Scalar versus Vector"

[9]   Sang Woo Nam, *Adapative Backstepping Based Online Loss Minimization Control of and Induction Motor Drive,* Master's thesis. Department of Electrical Enigneering, Lakehead University, July 2006.

[10]   B. K. Bose, "Power Electronics and AC Drives," Prentice Hall, 1986.

[11]   F. Blaschke, "The priciple of Field Orientation as Applied to the New Transvector Closed Loop Control System for Rotating Field Machines," Seimens Review, vol. 34, pp. 217-220, May 1972.

[12]   N. P. Quang and J.A. Dittrich, *Vector Control of Three-Phase AC Machines: System Development in Practice*, Springer Berlin Heidelberg, Jan 2010.

[13]   D.W. Novotony and T.A. Lipo, *Vector Control and Dynamics of AC Drives,* Oxford University Press, 1997.

[14]   M. Ichiro, I. Akio, and K. Takahashi, "Recent Industrial Application of Speed Sensorless Vector Control in Japan," *IEEE 24th International Conference on Industrial Electronics, Control and Instrumentatioin,* vol. 3, pp. 1573-1578, 1994.

[15]   Takahashi, T. Nouguchi, "A New Quick Response and High Efficiency Control Strategy for an Inducition Motor," *IEEE Trans. Industrial Applications,* vol. 22, no. 5, pp. 820-827, 1986.

[16]   M. Depenbrock., "Direct self-control (DSC) of inverter-fed induction machine," *IEEE Trans. Power Electronics,* vol. 3, no. 4, October 1988.

[17]   Hang Le-Huy, "Comparison of Field-Oriented Control and Direct Torque Control for Inductiion Motor Drives," *IEEE Industrial Application Conference,* vol. 2 pp. 1245-125, 1999.

[18] M. P. Kazmierkowski, "Control Philisophies of PWM Inverter-Fed Induction Motors," *IEEE Conf. Industrial Electronics*, vol. 1, pp. 16-26, 1997.

[19] Peter Vas, "Sensorless Vector and Direct Torque Control," Oxford University Press USA, 1998.

[20] ABB, Technical Guide 1, Direct Toruqe Control, ABB-library [online]. Available: http://www05.abb.com/global/scot/scot201.nsf/veritydisplay/299c5d307cb78a34c1256d2 8003fed0c/$File/ABB_Technical_Guide_1_%20EN26042002.pdf.

[21] N. Minorshy, "Directional stability of atuomatically steered bodies," *Journal of the American Society for Naval Engineers*, vol. 34, issue. 2, pp. 280-309, 1922.

[22] K. H. Ang, G. C. Y. Chong, and Y. Li., "PID Control System Analysis Design and Technology," *IEEE Trans. Control Systems Tech*, vol. 13 no. 4, pp. 559-576, 2005.

[23] G. Espinosa-Perez, and R. Ortega, "Tuning of PI Gains for FOC of Induction Motors with Guaranteed Stability," *IECON Proceedinggs*, vol. 2, pp. 569-574, 1997.

[24] G.-W. Chang, G. Espinosa-Perez, E. Mendes, and R. Ortega, "Tuning rules for the PI gains of field-oriented conrollers of induciton motors," *IEEE Trans. Industrial Electronics*, vol. 47, no. 3, pp. 592-602, June 2000.

[25] R. D. Lorenz, and B.B. Lawson, "A simplified approach to continuous on-line tuning of field-oriented inductin machine drives," *IEEE-IAS Conference Record (Pittsburgh)*, pp. 444-449, 1988.

[26] Kuo -Kai Shyu, Hsiu-Jang Shieh, and Sheng-Shang Fu, "Model Reference Adaptive Speed Control for Induction Motor Drive using Neural Networks," *IEEE Trans. Industrial Electronics*, vol. 45, no. 1, pp. 180-182, 1998.

116

[27]   P. Santhosh, R. H. Chile, A.B. Patil, and D.R. Patil, "Model Reference Adaptive Technique for Sensorless Speed Control of Induction Motor," *IEEE Conf. Emergin Trends in Engineering and Technology*, pp. 893-898, 2008.

[28]   K.B. Mohanty, "Sensorless Sliding Mode Cotrol of Induction Motor Drives," *TENCON*, pp. 1-6, 2008,

[29]   M. Rodic, K. Jezernik, and A. Sabanovic, "Speed Sensorless Sliding Mode Torque Control of Induction Motor," *IEEE Conf. Industry Applicatioins*, vol. 3 pp. 1820-1827, 2000.

[30]   Z. Hakan Akpolat, G. M. Asher, and J. C. Clare, "A practicale approach to the design of robust speed controller for machine drives," *IEEE Trans. Industrial Electronics*, vol. 47, no. 2, pp. 315-324, Apr 2000.

[31]   P.V. Kokotovic, "The Joy of Feedback Nonlinear and Adaptive," *IEEE Control Systems Magazine*, vol. 12, no. 3, pp. 7-17, 1992.

[32]   S. Shastry and M. Bodson, *Adaptive Control: Stability, Convergence and Robustness*, Prentice Hall, 1994.

[33]   H. Tan, and J. Chang,"Field Orientation and Adaptive backstepping for Induction Motor Control," *IEE- IAS-1999*, vol. 4, pp. 2357-2363.

[34]   A. S. Morse, "Global Stability of Parameter Adaptive Control Systems," *IEEE Trans. Automatic Control*", vol. AC-25, pp. 433-439, June 1980.

[35]   K. S. Narendra, Y. H. Lin, and I. S. Valavani, "Stable Apdaptive Controller Design- Part II: Proof of Stability," *IEEE Tran. Automatic Control*, vol. AC-25, pp. 440-448, June 1980.

117

[36]   G. C. Goodwin, P. J. Ramadge, and P. E. Caines, "Discrete Time Multivariable Adaptive Control," *IEEE Trans. Automatic Control*, vol. AC-25, pp. 449-456, June 1980.

[37]   C. E. Rohrs, L. Valavani, M. Athans, and G. Stein, "Robustness of Continuous-Time Adaptive Control Algorithms in the Presence of Unmodeled Dynamics," IEE *Trans. Automatic Control*, vol. 30, no. 9, pp. 881-889, Sep 1985.

[38]   L. Vandevelde, and J. A. A. Melkebeek, "Numerical Analysis of Vibrations of quirrel – Cage Induction Motors based on Magnetci Equivalent circuits and Structural Finite Element Models," *IEEE Conf. Industry Applicatioins*, vol.4, pp. 2288-2295, 2001.

[39]   Chin-Teng Lin, and C. S. G. Lee, "Neural Fuzzy Systems: A Neuro-Fuzzy Synergism to Intelligent Systems," NJ: Prentice Hall, *1996.*

[40]   Z. Ibrahim, And E. Levi. "A Comparative Analysis of Fuzzy Logic and PI Speed Control in High Perfbrmance AC Drives Using Experimental Approach," *IEEE Trans. Industrial Application*, vol. 38, no. *5,* pp. 1210-1218, Sept./Oct 2002.

[41]   Y. Tang, and L. Xu, "Fuzzy Logic Application for Intelligent Control of a Variable Speed Drive," *IEEE Trans. Power Electron*, vol. 12, pp. 1028-1039, November 1997.

[42]   C. C. Lee, " Fuzzy Logic In Control System: Fuzzy Logic Controller – Part I," *IEEE Trans. System, Man And Cybernetics*, vol. 20, no. 2, pp. 404-435, 1990.

[43]   L. A. Zadeh, "Fuzzy Sets", *Inforamtion and Control*, vol. 8, no. 3,pp. 338-353, 1965.

[44]   D. Driankov, H. Hellendoorn, and M. Reinfrank, *An Introduction to Fuzzy Control*, 2nd ed., Springer-Verlag Berlin, *1996.*

[45]   Fatiha Zidani, and Rachid Naït Saïd, "Direct Torque Control of Induction Motor with Fuzzy Minimization Torque Ripple," *Journal of Electrical Engineering*, vol. 56, no. 7-8, 2005, pp. 183-188.

[46]   Hassan-Halleh, Meisam Rahmani, and Bahram Kimiaghalam, "Direct Torque Control of Induction Motors with Fuzzy Logic Controller," *IEEE Conf. Control, Automation and Systems*, Oct 14-17, 2008 in CEOX, Seoul, Korea, pp. 345-350.

[47]   R. Toufouti, S. Meziane, and H. Benalla, "Direct Torque Control for Induction Motor using Intelligent Techniques," *Journal of Theoratical and Applied Information Technology*, pp. 35-44, 2007.

[48]   L. Youb, and A. Craciunescu, "Direct Torque Control of Induction Motors with Fuzzy Minimization Torque Ripple," *WESCO 2009*, vol. 2, pp. 713-717.

[49]   M. N. Uddin, T. S. Radwan, and M. A. Rahman, "Performance of fuzzy-logic based indirect vector control for induction motor drive," *IEEE Transaction on Industry Apllicatons*, vol. 38, no. 5, pp. 1219-1225, September/October 2002.

[50]   T. C. Huang, and M. A. El-Sharkawi, "High performance speed and position tracking of induction motors using multi-layer fuzzy control," *IEEE Trans. Energy Conversion*, vol. 11, no. 2, pp. 353-358, June 1996.

[51]   Y. Tang, and L. Xu, "Fuzzy Logic Application for Intelligent Control of a Variable Speed Drive," *IEEE Trans.Energy Conversion,* vol. 9, pp. 679-685, December 1994.

[52]   F. F. Cheng, and S. N. Yeh, "Application of Fuzzy Logic in the Speed Control of AC Servo System and an Intelligent Inverter," *IEEE Trans. Energy Conversion,* vol. 8, no. 2, pp. 312-318, June 1993.

119

[53] A. Engel, and C. Van Den Broech, *Statistical Mechanics of Learning*, Cambridge University Press, 2001.

[54] B. Kosco, "Neural Networks and Fuzzy Systems : A Dynamic Systems Approach to Machine Intelligence," Englewood Cliffs, NY: Prentice Hall, *1992*.

[55] R. Kumar, R. A. Gupta, S. V. Bhangale, and Himanshu Gothwal, "Artificial Neural Network Based Direct Torque Control of Induction Motor Drives," *IETECH Journal of Electrical Analysis*, vol. 2, no. 3, pp. 159-165, 2008.

[56] Y. V. S. Reddy, M. Vijayakumar, and T. Brahmananda Reddy, "Direct Torque Control of Induction Motor Using Sophisticated Lookup Tables Based on Neural Networks," *AIML Journal*, vol. 7, no. 1, June 2007.

[57] Yen-Shin Lai, and Juo-Chiun Lin, "New Hybrid Fuzzy Controller for Direct Torque Control Induction Motor Drives," *IEEE Trans. Power Electronics*, vol. 18, no. 5, pp. 1211-1219, September 2003.

[58] P. C. Krause, and C. H. Thomas, "Simulation of Symmetrical Induction Machinery," *IEEE Trans. Power Apparatus System*, vol. PAS-84, no. 11, pp. 1038-1053, 1965.

[59] N.R.N Idris, and A.H.M Yatim, "Direct Torque Control of Induction Machine with Constant Switching Frequency and Reduced Torque Ripple," *IEEE Trans. Ind. Electronics*, vol. 51, no. 4, pp.758-767, Aug. 2004.

[60] A E. Fowkes, "Hardware efficient algorithm for trigonometric functions," *IEEE Trans. Computers*, vol. 42 no. 2, pp. 235-239, February 1993.

[61] Marin P. Kazmierdowski, "Improved direct torque and flux vector control of PWM inverter-fed induction motor drives," *IEEE Trans. Ind. Electronics*, vol. 42, no. 4, August 1995.

[62] *Matlab, Simulink User Guide*, The Math Works Inc., 2004.

[63] B. Kosko, *Fuzzy Engineering*, Prentice-Hall Inc., 1997.

[64] David M. Skapura, *Building Neural Networks*, ACM Press, Addison-Wesley, 1996

[65] H.Dmathur, and S. Ghosh, "A Comprehensive Analysis of Intelligent Controllers for Load Frequency Control," *Power India Conference, IEEE*, 10-12 April, 2006. pp. 5.

[66] D. Driankov, H. Hellendoorn, and M. Reinfrank, "An introduction to fuzzy control," 2nd ed., Springer-Verlag, Berlin. 1996.

[67] Peter Vas, *Artificial-Intelligence-Based Electrical Machines and Drives*, Oxford University Press, 1999.

[68] M. N. Uddin, and Hao Wen, "Development of a Self-Tuned Neuro-Fuzzy Controller for Induction Motor Drives," *IEEE transaction on Industrial Electronics*, vol. 42, no. 4, July/August 2007.

[69] Akio Yamamoto, Yosunori Kitamura, and Yoshihiro Yamane,"Computational Efficiencies of Approximated Exponential Functions for Transport Calculations of the Characteristics Method," Annals of Nuclear Energy, vol. 31, pp. 1027-1037, 2004. Available: www.Sciencedirect.com

[70] *dSPACE*, "Digital Signal Processing and Control Engineering", Implementation Guide, Paderborn, Germany, 2003.

121

Appendix -A

IM Parameters

	Simulation	Real Time
Number of phases	3	3
Number of pole pairs	2	2
Rated Frequency (Hz)	60	60
Rated Speed (rpm)	1725	1725
Rated power (HP)	5	1/3
Rated input line-to-line voltage (volts)	460	208
Mutual Inductance, Lm (H)	0.2037	0.2655
Stator leakage inductance, $L_{ls\ (mH)}$	5.974	275.8
Rotor leakage inductance, L_{lr} (mH)	5.974	280.9
Stator resistance per phase Rs (Ω)	1.115	6.5
Rotor resistance per phase Rr(Ω)	1.083	3.4
Inertia constant J (K-m^2)	0.02	0.0012
Rotor damping constant B_m (N.m.s)	0.005752	

Appendix – B

Subsystems for Simulink/Matlab Model
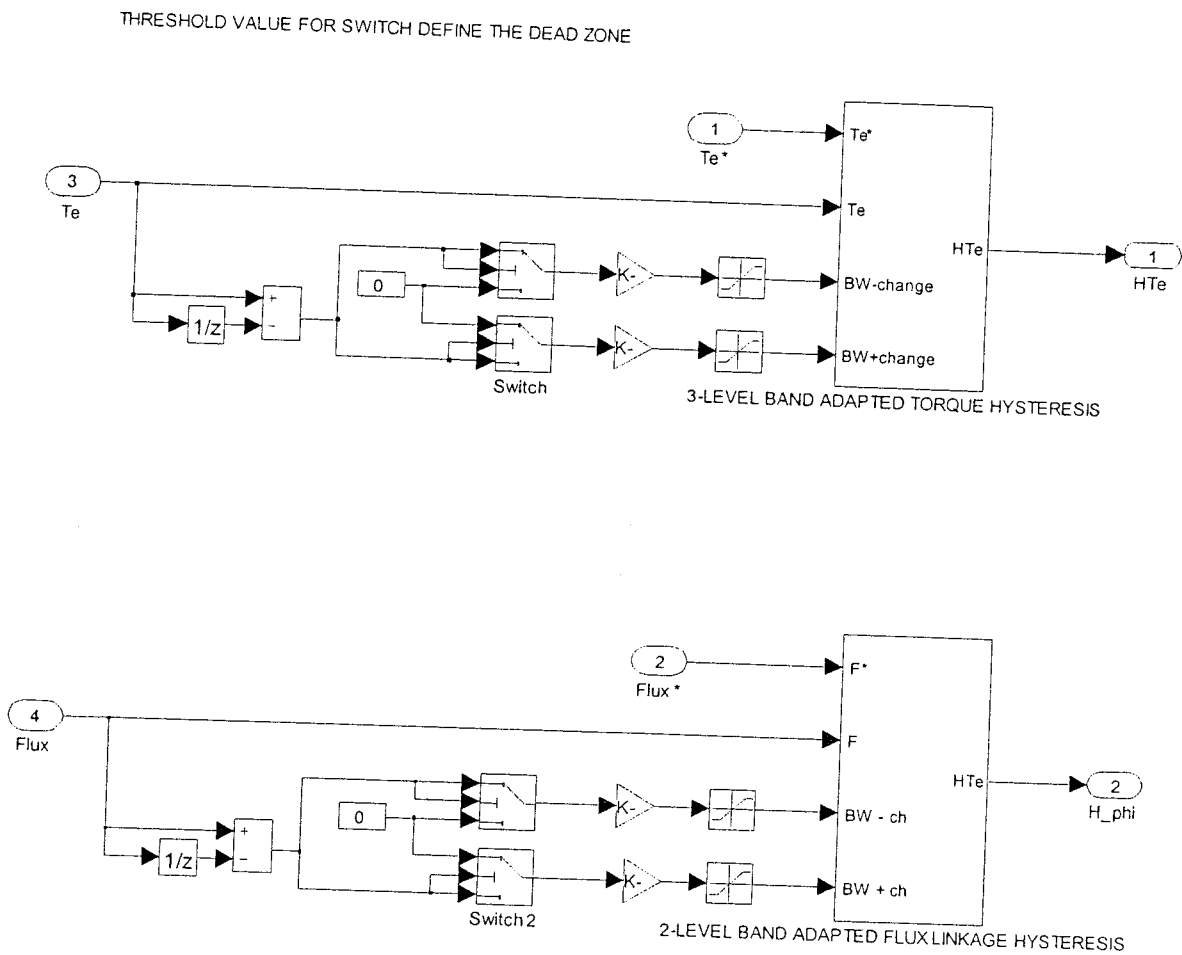
B.1: Subsystem of "Hysteresis Comparators".
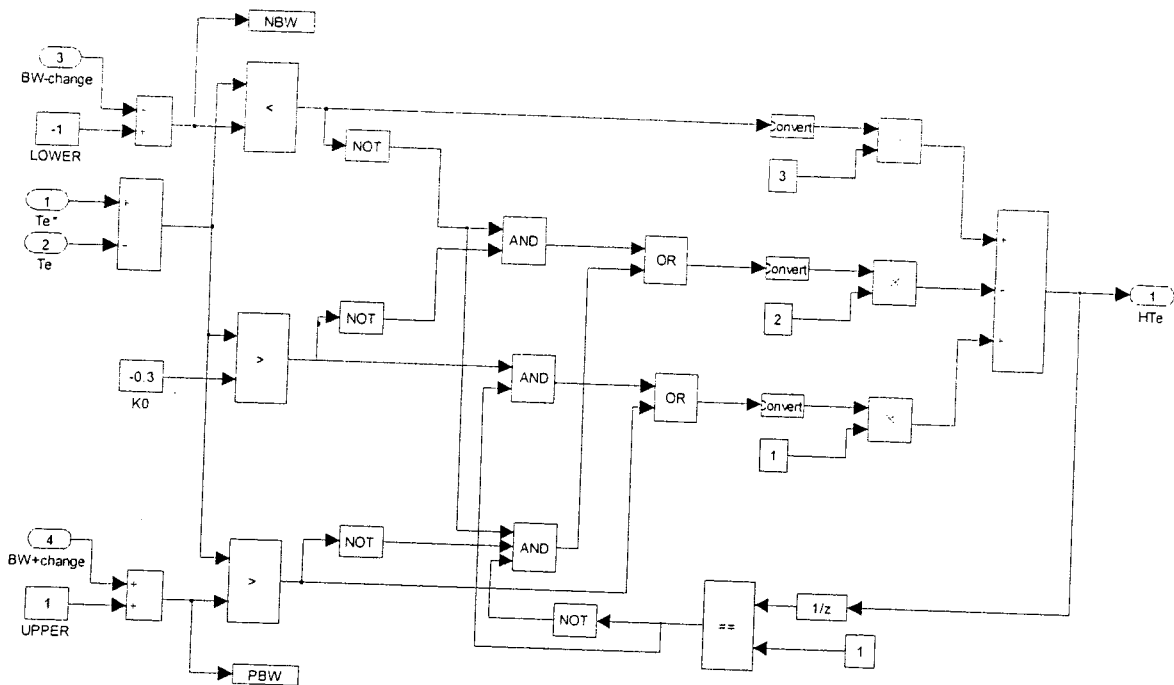
B.2: Subsystem of "3-level band adapted torque hysteresis".
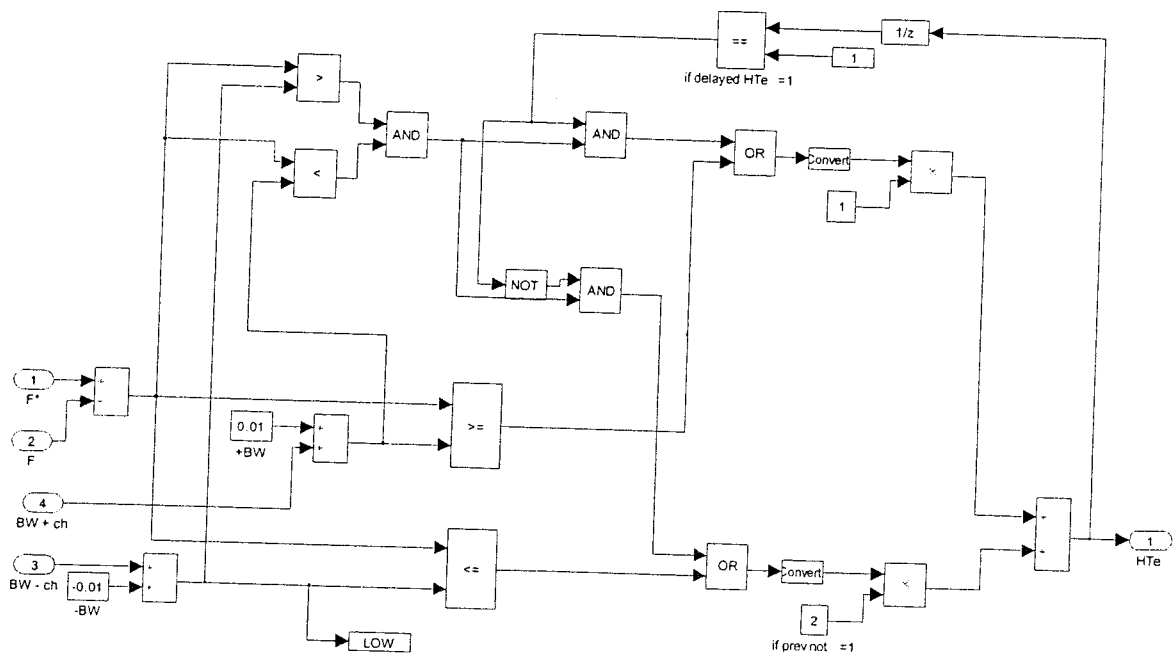
B.3: Subsystem of "2-level band adapted flux hysteresis"

124
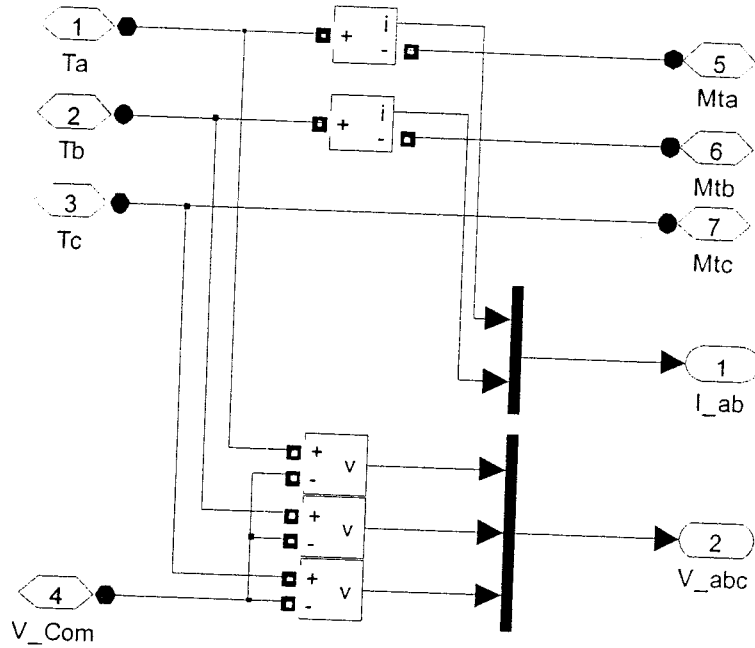
B.4: Subsystem of "Electrical Measurements"
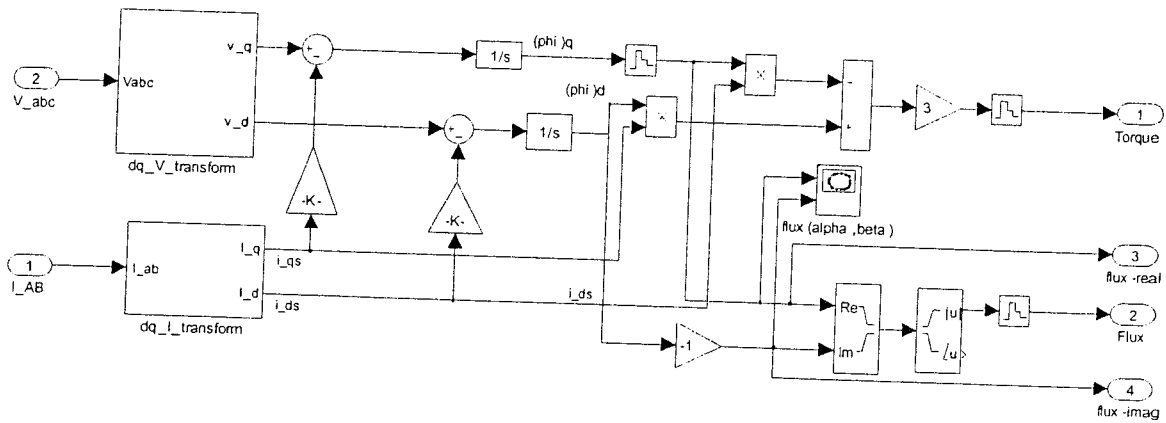
B.5: Subsystem of "Flux & Torque Estimation"

125
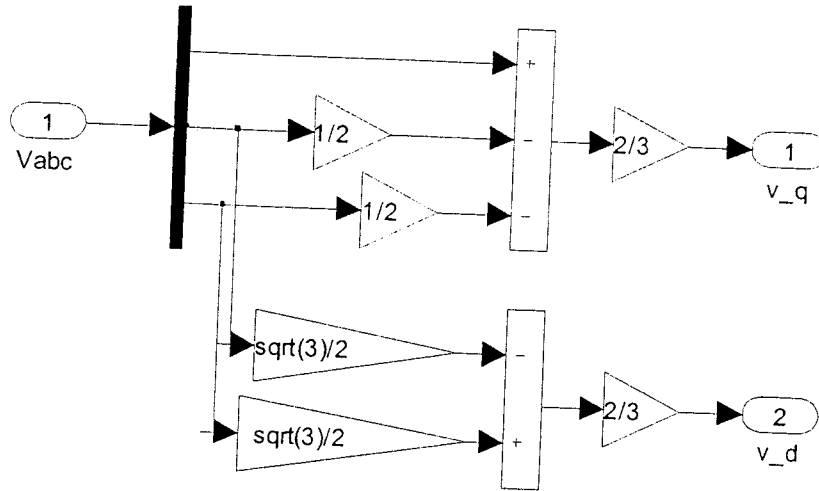
B.6: Subsystem of "Stator voltage abc-dq transformation
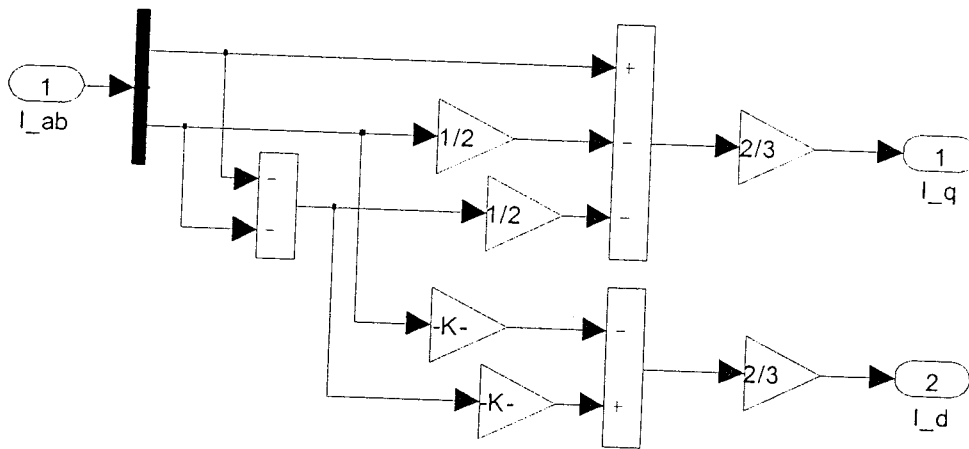
B.7: Subsystem of "Stator current abc-dq transformation

126
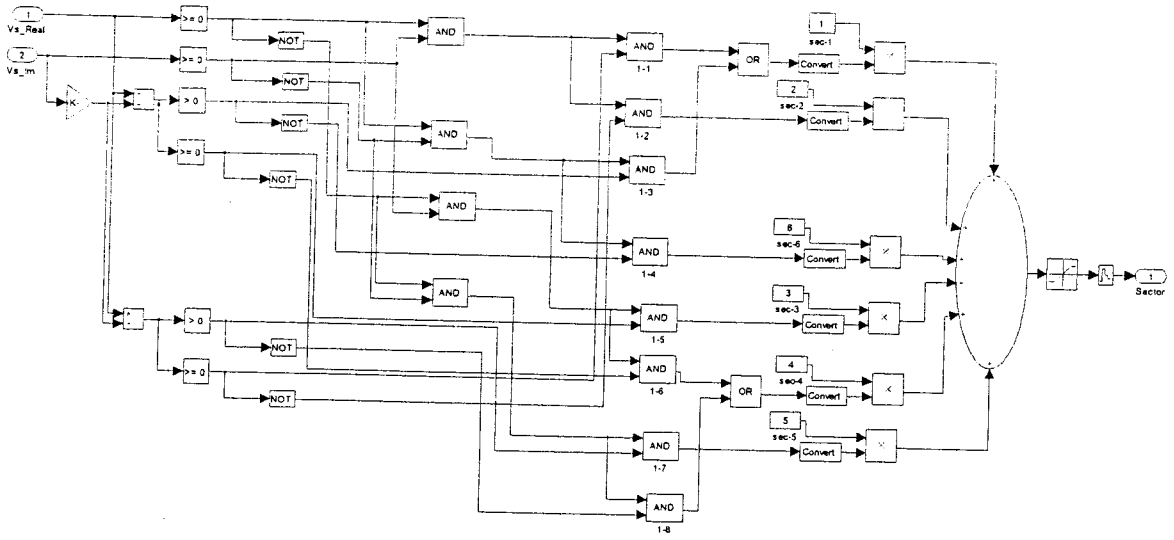
B.8: Subsystem of "Flux Sector"
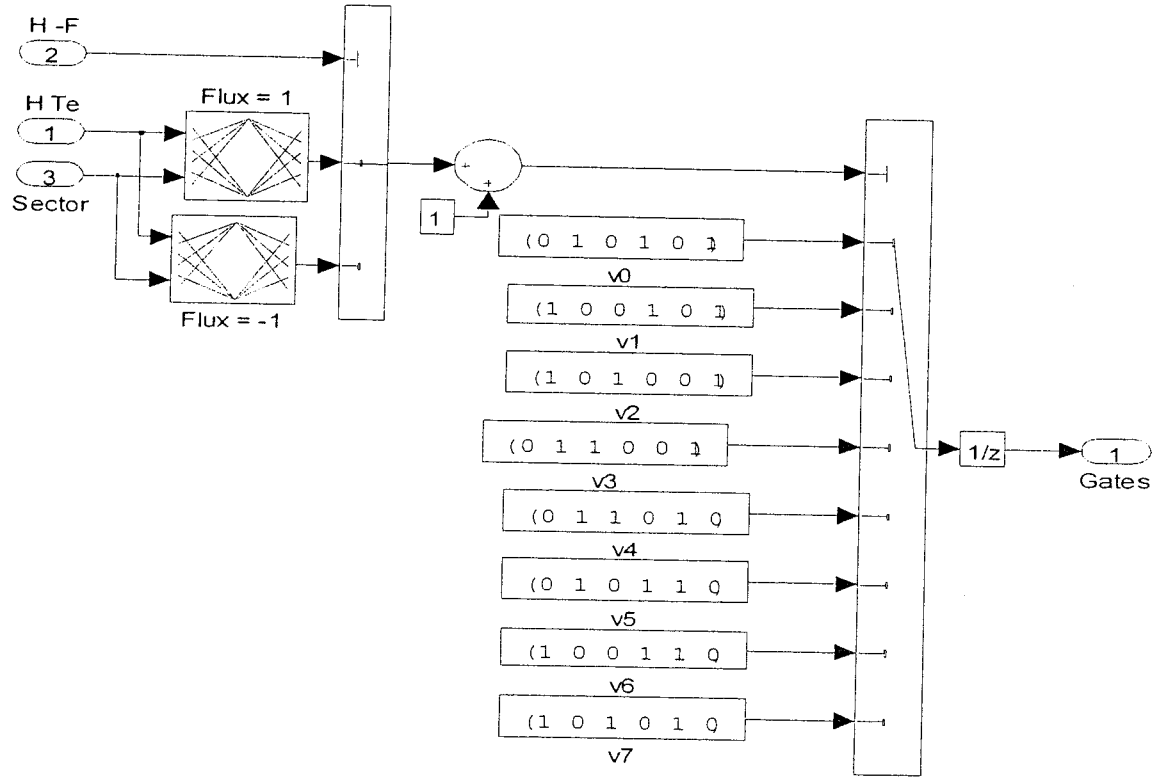
B.9: Subsystem of "Switching Table"

127
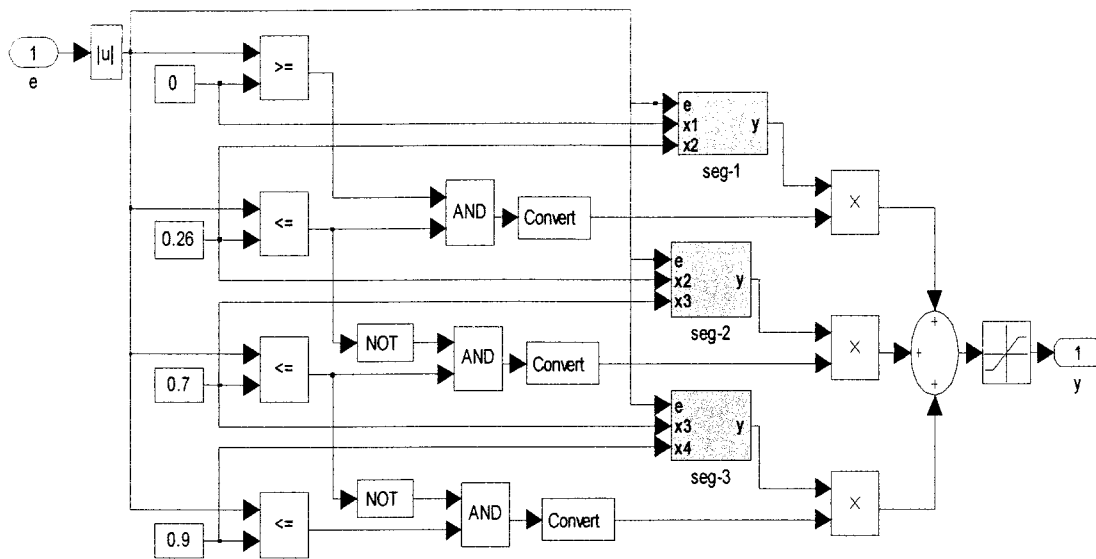
B.10: Subsystem of "mf_ZE(e)".
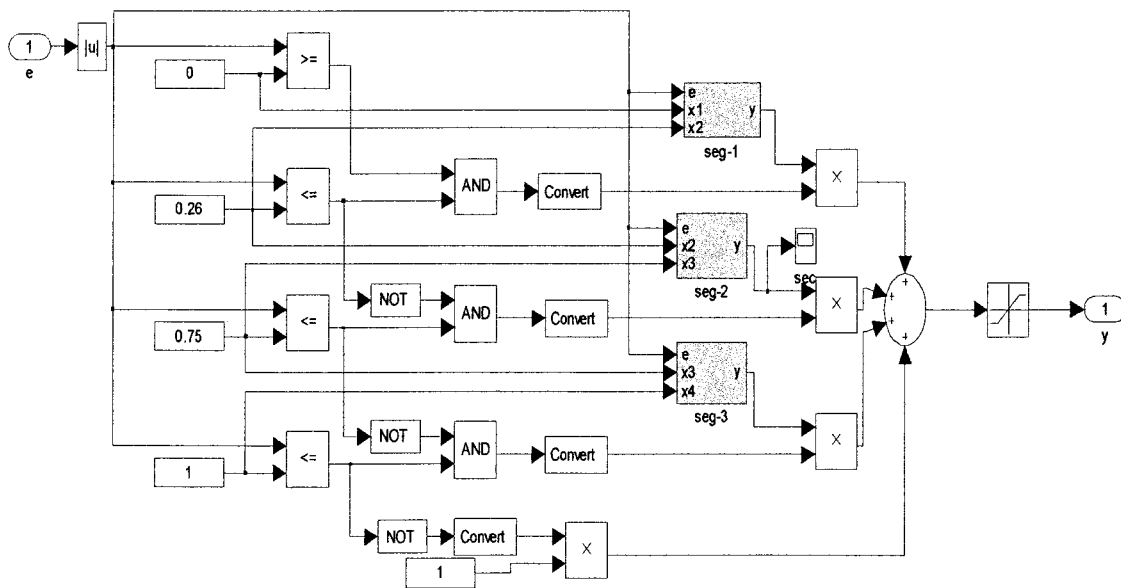
B.11: Subsystem of "mf_PN(e)".
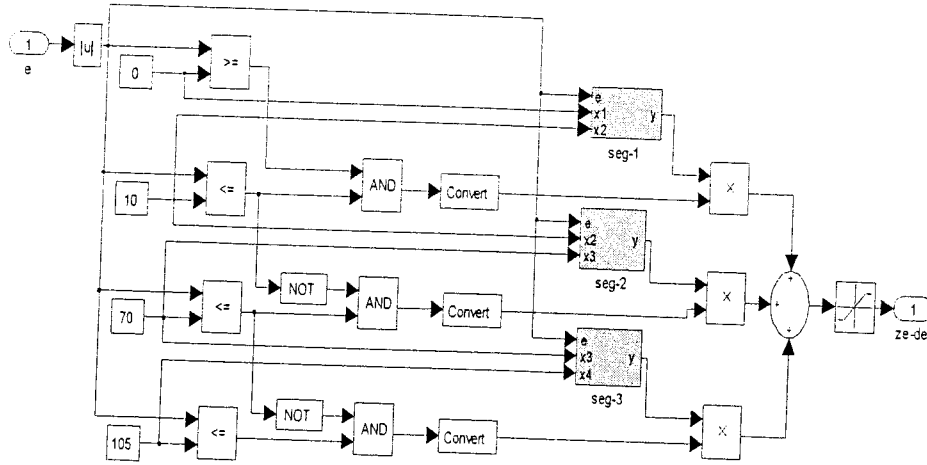
B.12: Subsystem of "mf_ZE(de)".
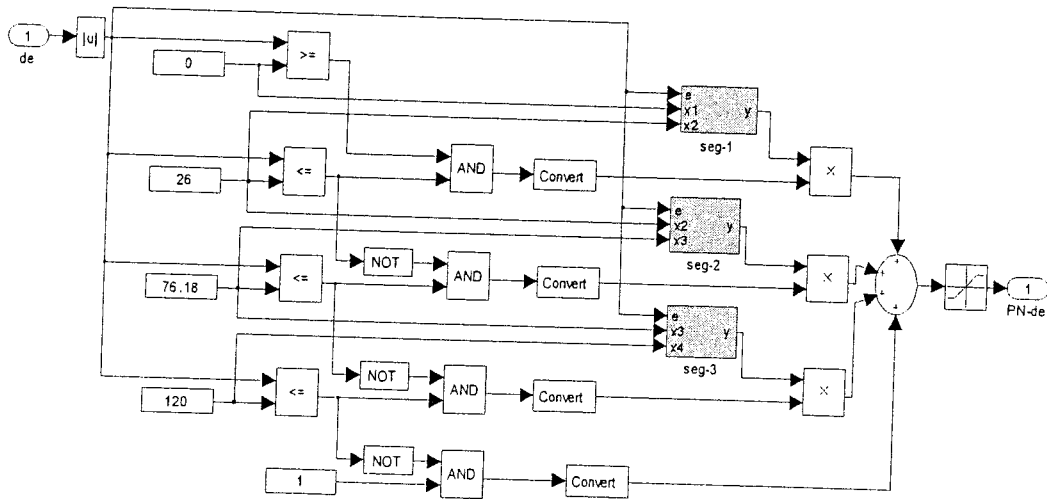
B.13: Subsystem of "mf_PN(de)".

129
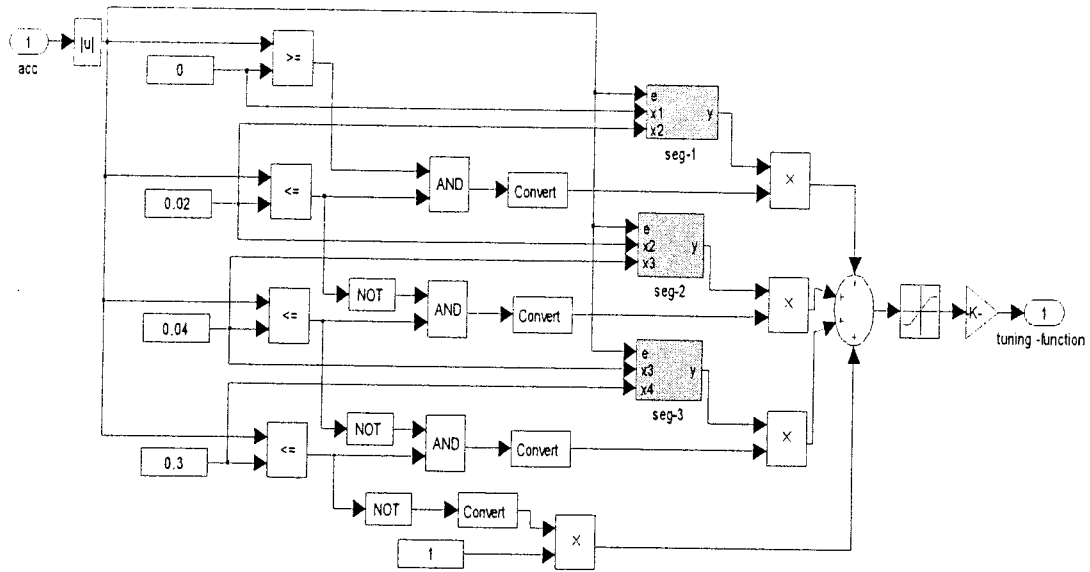
B.14: Subsystem of Tuning function
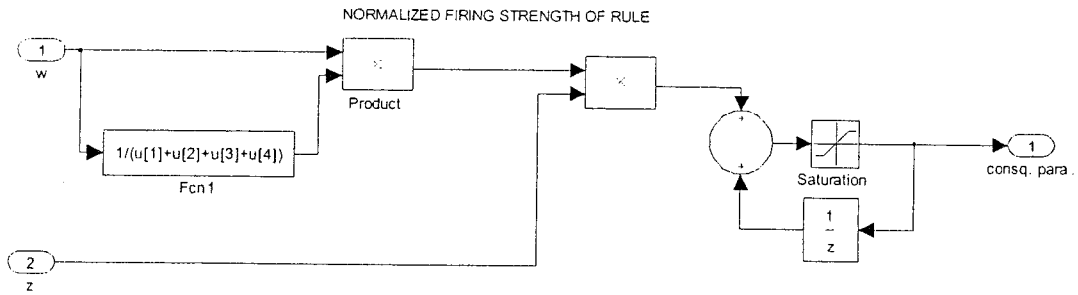
B.15: Subsystem of "updated consequent parameter"

130

Appendix C

Drive and Interface Circuits
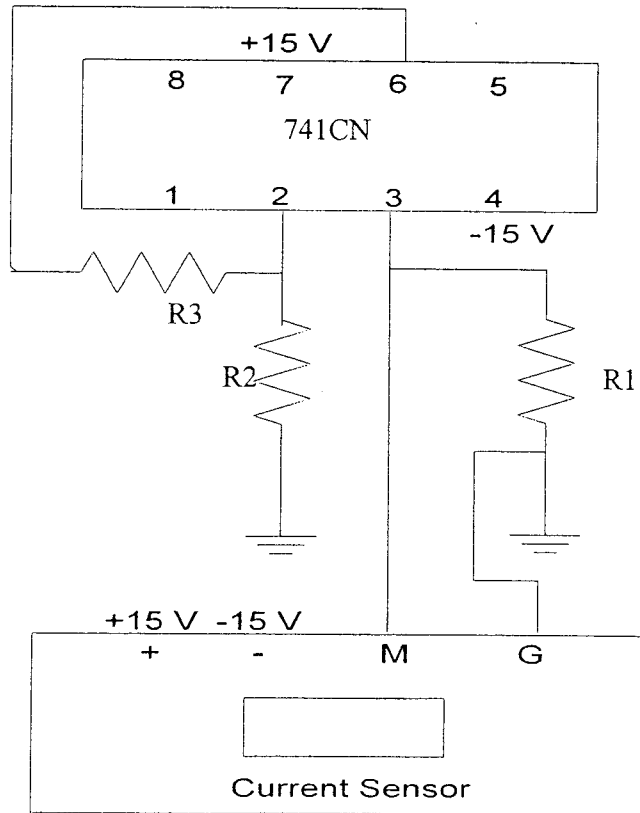
$$R1 = R2 = R3 = R4 = R5 = R6 = 1.5k$$
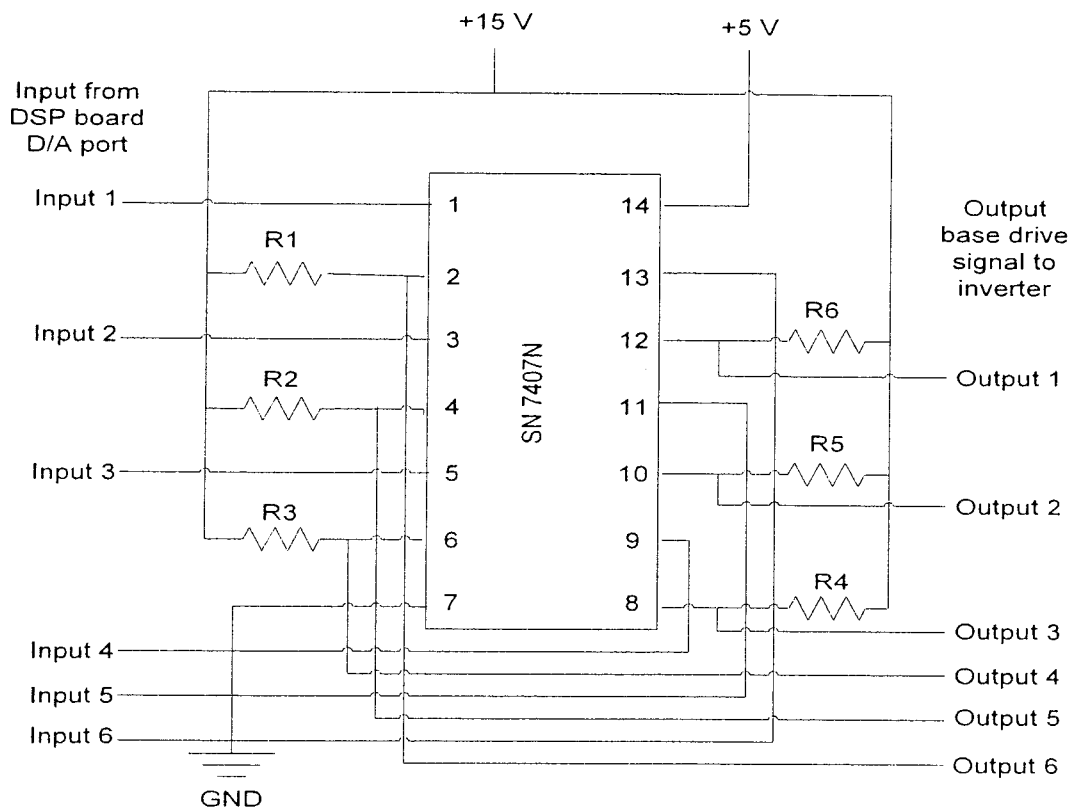
C.1: Base drive circuit for the inverter
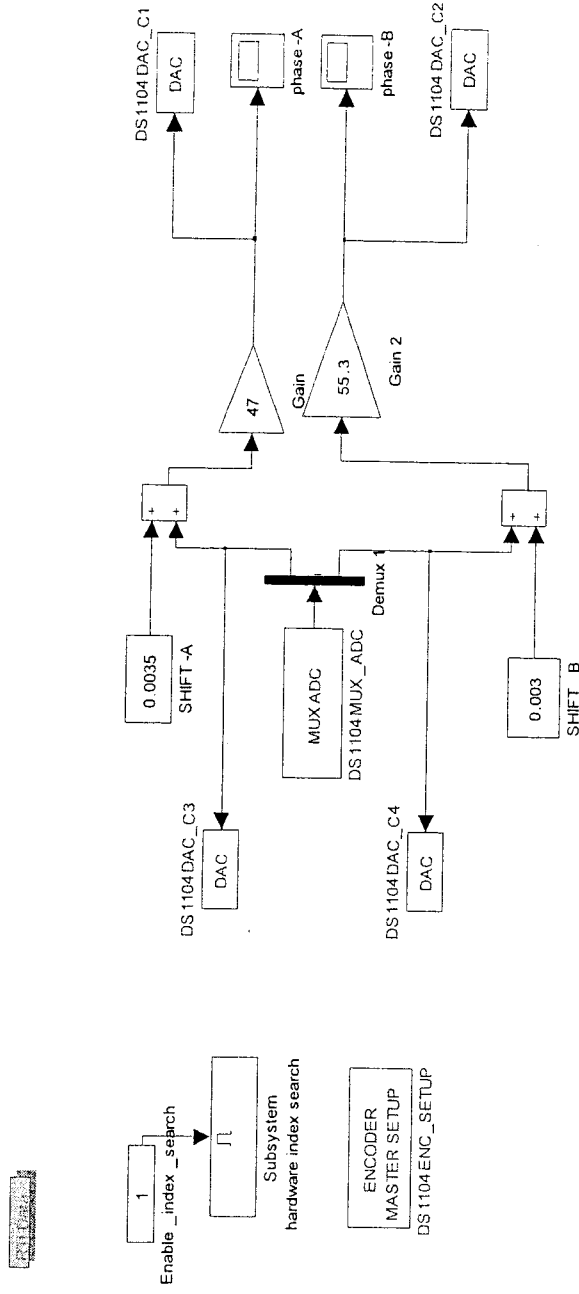
Gain of Op-Amp (741CN) = 1+R3/R2

Magnitude of resistors:

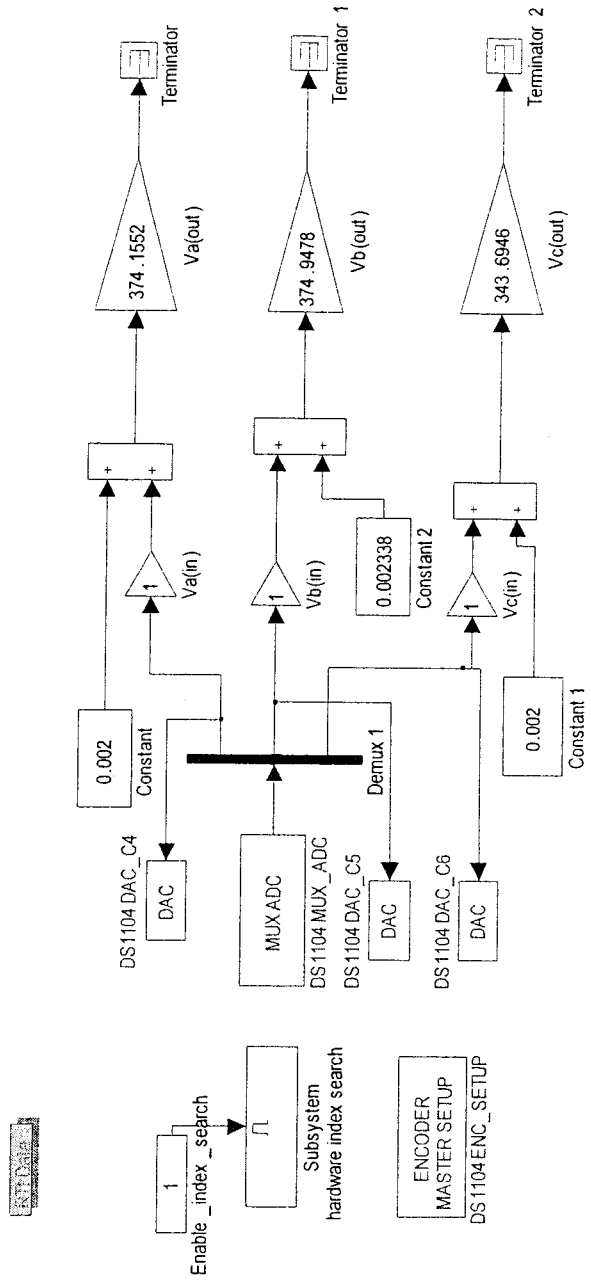|	Current sensor for phase 'a'	Current sensor for phase 'b'
R1	98.7 ohm	99 ohm
R2	1.8 k	2 k
R3	5.5 k	5.1 k

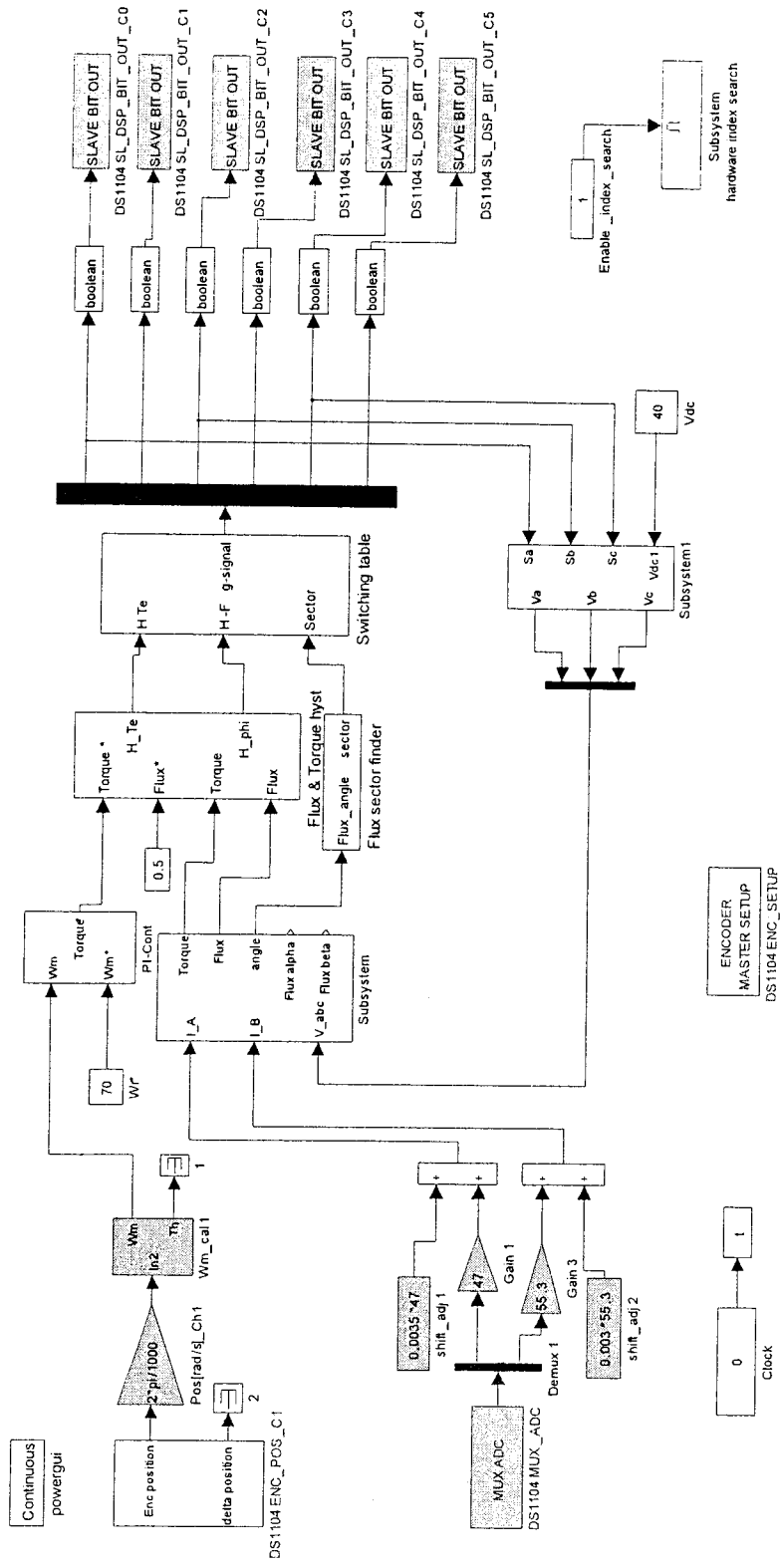C.2. interface circuit for the current sensor

132

Appendix-D

Real-Time Simulink Models

D.1: Real time Simulink/Dspace software block diagram for current sensor testing

133

D.2. Real time Simulink/Dspace software block diagram for voltage sensor testing

134

D3. Real-time Simulink model for the proposed DTC scheme.

135